

# Antiferromagnetic spintronics

V. Baltz\*

*SPINTEC, Univ. Grenoble Alpes/CNRS/INAC-CEA, F-38000 Grenoble, France*

A. Manchon†

*King Abdullah University of Science and Technology (KAUST),  
Physical Science and Engineering Division (PSE), Thuwal 23955-6900, Saudi Arabia*

M. Tsoi

*Department of Physics, The University of Texas at Austin, Austin, Texas 78712-0264, USA*

T. Moriyama

*Institute for Chemical Research, Kyoto University, 611-0011 Uji, Kyoto, Japan*

T. Ono

*Institute for Chemical Research, Kyoto University, 611-0011 Uji, Kyoto, Japan*

Y. Tserkovnyak

*Department of Physics and Astronomy, University of California,  
Los Angeles, California 90095, USA*

 (published 15 February 2018)

Antiferromagnetic materials could represent the future of spintronic applications thanks to the numerous interesting features they combine: they are robust against perturbation due to magnetic fields, produce no stray fields, display ultrafast dynamics, and are capable of generating large magnetotransport effects. Intense research efforts over the past decade have been invested in unraveling spin transport properties in antiferromagnetic materials. Whether spin transport can be used to drive the antiferromagnetic order and how subsequent variations can be detected are some of the thrilling challenges currently being addressed. Antiferromagnetic spintronics started out with studies on spin transfer and has undergone a definite revival in the last few years with the publication of pioneering articles on the use of spin-orbit interactions in antiferromagnets. This paradigm shift offers possibilities for radically new concepts for spin manipulation in electronics. Central to these endeavors are the need for predictive models, relevant disruptive materials, and new experimental designs. This paper reviews the most prominent spintronic effects described based on theoretical and experimental analysis of antiferromagnetic materials. It also details some of the remaining bottlenecks and suggests possible avenues for future research. This review covers both spin-transfer-related effects, such as spin-transfer torque, spin penetration length, domain-wall motion, and “magnetization” dynamics, and spin-orbit related phenomena, such as (tunnel) anisotropic magnetoresistance, spin Hall, and inverse spin galvanic effects. Effects related to spin caloritronics, such as the spin Seebeck effect, are linked to the transport of magnons in antiferromagnets. The propagation of spin waves and spin superfluids in antiferromagnets is also covered.

DOI: [10.1103/RevModPhys.90.015005](https://doi.org/10.1103/RevModPhys.90.015005)

## CONTENTS

I. Introduction	2	3. Semiconductors and semimetals	4
A. Current challenges	2	C. Basics of antiferromagnets	5
B. Materials survey	2	1. Quantum aspects	5
1. Metals	3	a. A prologue on quantum antiferromagnets	5
2. Insulators	4	b. Electronic band structure	7
		2. Some key parameters	7
		a. Magnetic susceptibility and Néel temperature	7
		b. Magnetic phase transition and finite-size scaling	8
		c. Spatial variability of magnetic properties	9

\*vincent.baltz@cea.fr

†aurelien.manchon@kaust.edu.sa

3. Manipulation by magnetic field, light, and exchange bias	10
a. Manipulation by magnetic field	10
b. Optical manipulation	12
c. Manipulation by exchange bias	13
4. Magnetic textures	14
a. Experimental observation of antiferromagnetic textures	15
b. Relativistic dynamics	16
c. Field-driven manipulation of domain walls	17
II. Spin-transfer Electronics	17
A. Spin-transfer torque and spin pumping	18
1. Principle of spin-transfer torque	18
2. Manipulation of the order parameter by spin-transfer torque	18
a. Antiferromagnetic spin valves	18
b. Antiferromagnetic tunnel junctions	20
c. Seeking spin-transfer torque experimentally	21
d. Current-driven dynamics	22
3. Moving magnetic textures by spin-transfer torque	23
4. Spin pumping from antiferromagnets	24
B. Spin-mixing conductance and penetration depths	25
1. Spin-mixing conductance at antiferromagnetic interfaces	25
2. Spin penetration depths and relaxation mechanisms	27
C. Giant and tunnel magnetoresistance	29
1. Giant magnetoresistance	29
2. Tunnel magnetoresistance	30
III. Spin Orbitronics	30
A. Anisotropic magnetoresistance	30
B. Tunnel anisotropic magnetoresistance	31
C. Anomalous and spin Hall effects	33
1. Anomalous Hall effect in noncollinear antiferromagnets	33
2. Spin Hall effect	34
3. Spin Hall magnetoresistance	37
D. Spin-orbit torques	37
1. Principle of spin-orbit torques	37
2. Manipulation of the order parameter by spin-orbit torque	38
a. Manipulation by inverse spin galvanic torque	39
b. Manipulation by spin Hall torque	40
3. Moving magnetic textures by spin-orbit torque	41
4. Current-induced switching by antiferromagnets	41
IV. Spin Caloritronics and Superfluidity	41
A. Thermally induced spin currents	42
B. Superfluid spin transport	45
C. Thermally induced domain-wall motion	46
V. Conclusion and Perspectives	47
Acknowledgments	47
References	47

## I. INTRODUCTION

### A. Current challenges

In the field of spintronics much effort is being deployed to reduce device power consumption and scale (Duine, 2011; Sinova and Žutić, 2012). Antiferromagnetic materials have great potential in this regard, which makes them outstanding candidates for the next generation of spintronic applications. Ultimately, antiferromagnets could replace ferromagnets as

the active spin-dependent element on which spintronic devices are based. Antiferromagnetic materials, through their robustness against perturbation due to magnetic fields, the absence of production of parasitic stray fields, ultrafast dynamics, and the generation of large magnetotransport effects, have a number of interesting properties. For instance, synthetic antiferromagnets [i.e., two ferromagnets coupled antiparallel usually by Ruderman-Kittel-Kasuya-Yoshida interactions (Parkin, 1991)] are currently used to overcome device malfunction associated with ferromagnetic stray fields when lateral dimensions are reduced (e.g., crosstalk in magnetic random access memories: mutual influence of neighboring cells which are supposed to be isolated from one another). However, synthetic antiferromagnets never entirely compensate, and small, but nonzero stray fields persist. With antiferromagnetic materials, the net compensation is intrinsic except for a very small proportion at the interface. To build a functional “(ferro)magnet-free” device, it is first necessary to determine whether and how spin transport can be used to *write* the antiferromagnetic order and *read* subsequent variations through the development of predictive models, relevant disruptive materials, and new experimental designs. Several teams are already studying the theoretical and experimental aspects of the subject. To begin with, we review the antiferromagnetic materials suitable for antiferromagnetic spintronics and their fundamental properties. Selected current topics are then dealt with in different sections, depending on whether they relate to spin-transfer electronics, spin orbitronics, or spin caloritronics. The contributions of these different subfields to write (through spin torque) and read (via magnetoresistance) the antiferromagnetic order is also discussed. Interested readers are encouraged to complement their knowledge on specific points by consulting focused reviews, e.g., relating to the theory of current-induced torques in metals (Haney *et al.*, 2008), spin transfer in antiferromagnet-based spin valves (MacDonald and Tsoi, 2011), dynamics of the antiferromagnetic order (Gomonay and Loktev, 2014), spin Hall effects in metallic antiferromagnets (Sklenar *et al.*, 2016), and manipulation and detection of the magnetic state of an antiferromagnet (Jungwirth *et al.*, 2016; Fina and Marti, 2017).

### B. Materials survey

In the context of ferromagnetic/antiferromagnetic exchange-bias magnetic interactions (see Sec. I.C.3), antiferromagnetic materials have been the subject of intense research for no less than 60 years. In this framework, several authors (Berkowitz and Takano, 1999; Nogués and Schuller, 1999; Umetsu *et al.*, 2003; Coey, 2009; Mácá *et al.*, 2012) have extensively reviewed the properties of antiferromagnetic materials focusing on composition, atomic structure, spin structure, stoichiometry range, and critical temperatures. Whereas the antiferromagnetic properties required for ferromagnetic/antiferromagnetic exchange bias are reasonably well established, those for spin-dependent transport are still under investigation, e.g., spin penetration length, spin Hall angle, and domain-wall velocity. Here we briefly discuss some antiferromagnetic materials and their properties from the perspective of spin transport (Tables I–III). The spintronic

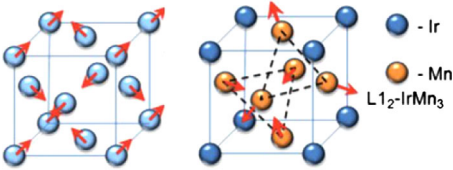
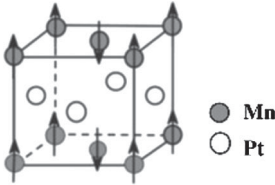
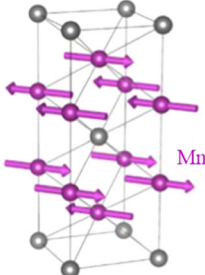
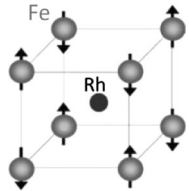
effects identified will be further detailed throughout the review. The materials listed in the tables are split into three categories depending on their metallic, insulating, or semiconducting or semimetallic nature. Given their wide variety, we restricted our tables to selected materials either because they have a bulk Néel temperature above room temperature or because they played a key role in the development of antiferromagnetic spintronics. Tables I–III illustrate the vast numbers of materials available, while also listing the corresponding crystallographic and spin structures. This multitude of options opens numerous pathways for the investigation of spintronics with antiferromagnetic materials.

### 1. Metals

Metallic antiferromagnets (Table I) comprise Mn-based alloys such as IrMn, FeMn, and PtMn. These types of materials

are most often produced by sputter deposition and are by far the most widely used in industrial applications (mostly for exchange bias). Examples of applications include read heads in hard disk drives and magnetic memories. The possibility to switch from an alloy containing a light element (such as Fe) to heavier elements (such as Ir and Pt) is essential for the exploration of spin-transfer effects [e.g., spin penetration length (Acharyya *et al.*, 2010, 2011; Merodio, Ghosh *et al.*, 2014) (see Sec. II.B), magnetic order manipulation by spin-transfer torque (Wei *et al.*, 2007) (see Sec. II.A.2), giant magnetoresistance (Y. Y. Wang *et al.*, 2014a) (see Sec. II.C), and enhanced spin pumping near the Néel temperature (Frangou *et al.*, 2016) (see Sec. I.C.2)], spin-orbit effects [e.g., the inverse spin Hall effect (Mendes *et al.*, 2014; W. Zhang *et al.*, 2014) (see Sec. III.C.2)], and their subsequent use for the deterministic reversal of ferromagnets by spin Hall torque [(Brink *et al.*, 2016;

TABLE I. Crystallographic structure, spin structure, and Néel temperature ( $T_N$ , antiferromagnetic-to-paramagnetic transition) of some metallic antiferromagnets. The last column indicates whether studies investigated finite-size effects on  $T_N$  ( $T_{N,finite\ size}$ ).

Electrical category	Crystallographic and spin structures (bulk)	Material	$T_{N,bulk}$ (K)	$T_{N,finite\ size}$ (K)
Metal	 <p><math>\gamma</math>-phase = disordered <math>L1_2^a</math> From Kohn <i>et al.</i>, 2013</p>	Ir <sub>20</sub> Mn <sub>80</sub> Fe <sub>50</sub> Mn <sub>50</sub>	690 490	(Petti <i>et al.</i> , 2013; Frangou <i>et al.</i> , 2016) ...
	 <p><math>S_{Mn} \parallel c</math> (e.g. PtMn) or <math>a</math> (e.g. NiMn) From Umetsu, Fukamichi, and Sakuma, 2006</p>	Ir <sub>50</sub> Mn <sub>50</sub> Ni <sub>50</sub> Mn <sub>50</sub> Pt <sub>50</sub> Mn <sub>50</sub> Pd <sub>50</sub> Mn <sub>50</sub>	1150 1070 970 810	... ... ... ...
	 <p>From Barthem <i>et al.</i>, 2013</p>	Mn <sub>2</sub> Au	~1500	...
	 <p>From Ju <i>et al.</i>, 2004</p>	Fe <sub>50</sub> Rh <sub>50</sub>	380 <sup>b</sup>	(Han <i>et al.</i> , 2013; Saidl <i>et al.</i> , 2016)

<sup>a</sup>The spin structure in  $L1_2$ -IrMn<sub>3</sub> is also called  $3Q$  (triple  $Q$ ).

<sup>b</sup>Data for Fe<sub>50</sub>Rh<sub>50</sub> are for the specific antiferromagnetic-to-ferromagnetic transition.

Fukami *et al.*, 2016; Lau *et al.*, 2016; Oh *et al.*, 2016) (see Sec. III.D.4)]. In addition, the  $3d$  shell of the Mn transition metal offers large spontaneous moments, while the  $5d$  shell of the noble metals (Pt in PtMn, Ir in IrMn, and Au in Mn<sub>2</sub>Au) provides large spin-orbit coupling. This combination is ideal for handling strong magnetic anisotropy phenomena [e.g., tunnel anisotropic magnetoresistance (Shick *et al.*, 2010; Park *et al.*, 2011; Wang *et al.*, 2012) (see Sec. III.B) and anisotropic magnetoresistance (Galceran *et al.*, 2016; S. M. Wu *et al.*, 2016) (see Sec. III.A)]. Moreover, the noncollinearity of the spin texture, found, for example, in  $\gamma$ -FeMn (Shindou and Nagaosa, 2001) and IrMn<sub>3</sub> (Chen, Niu, and MacDonald, 2014), breaks the invariance under the combination of time-reversal symmetry with a crystal symmetry operation resulting in a finite anomalous Hall effect (see Sec. III.C.1). In the specific case of Mn<sub>2</sub>Au, inverse spin galvanic effects have been predicted (Železný *et al.*, 2014) and experimentally demonstrated (Meinert, Graulich, and Matalla-Wagner, 2017), with current-induced staggered spin accumulation matching the staggered spin texture (see Sec. III.D.2). Metallic antiferromagnets also comprise archetypal materials such as Cr with an intriguing spin density wave configuration (Fawcett, 1988). This material has been thoroughly studied in Cr/MgO-based multilayers (Leroy *et al.*, 2013) (see Sec. II.C). Metallic metamagnets with an antiferromagnetic to ferromagnetic transition (such as FeRh) offer the possibility to indirectly operate the antiferromagnetic order via iterative steps consisting of manipulating the ferromagnetic order and undergoing the magnetic phase transition. In the case of FeRh, a small (noncrystalline) anisotropic magnetoresistance was also detected in the antiferromagnetic phase and quasistatic write-read operations were demonstrated (Marti *et al.*, 2014; Moriyama, Takei *et al.*, 2015; Clarkson *et al.*, 2017). Other important materials include, for example, Gd alloys, such as GdSi, GdGe, and GdAu<sub>2</sub> (Tung *et al.*, 1996). These alloys offer the possibility to exploit rare-earth-based antiferromagnetic metals. Other materials may also be interesting to consider for future fundamental studies on antiferromagnetic spintronics, such as TiAu (Svanidze *et al.*, 2015), an itinerant antiferromagnet without magnetic constituents, or CrB<sub>2</sub> (Brasse *et al.*, 2013) which potentially combines antiferromagnetic spintronics and superconductivity.

## 2. Insulators

Insulating antiferromagnets (Table II) are mostly oxides. They are ideal for studying magnonic effects [e.g., the propagation of spin waves in NiO (Hahn *et al.*, 2014; H. Wang *et al.*, 2014; Takei and Tserkovnyak, 2015) (see Secs. II.B and IV.B)] and subsequent caloritronic effects [e.g., spin Seebeck in Cr<sub>2</sub>O<sub>3</sub> (Seki *et al.*, 2015) (see Sec. IV.B)]. Optical excitation of spin waves in antiferromagnets is briefly discussed in Sec. I.C.3. Tunnel anisotropic magnetoresistance (Sec. III.B) based on antiferromagnetic CoO barriers was also demonstrated (K. Wang *et al.*, 2015). In addition, some specific antiferromagnetic insulators show interesting multiferroicity and magnetoelectric effects (Binek and Doudin, 2005; Martin *et al.*, 2008). Typical mechanisms involve direct coupling between ferroic orders, as in perovskite BiFeO<sub>3</sub>, where the ferroelectric and antiferromagnetic orders coexist (Sando, Barthélémy, and Bibes, 2014). A purely

antiferromagnetic magnetoelectric random access memory was recently demonstrated using the magnetoelectric antiferromagnet Cr<sub>2</sub>O<sub>3</sub> (Kosub *et al.*, 2017). Alternatively, the magnetoelectric effect in the antiferromagnet gives rise to electrically induced interface magnetization which can couple to an adjacent ferromagnetic film, such as with Cr<sub>2</sub>O<sub>3</sub>/[Co/Pd] multilayers (He *et al.*, 2010). Other perovskite antiferromagnets have been explored and may be promising materials for antiferromagnetic spintronics. For example, antiferromagnetic order can be excited in LaMnO<sub>3</sub> and La<sub>2</sub>CuO<sub>4</sub> (Coldea *et al.*, 2001) (Sec. I.C.3), which could be of interest when seeking to generate spin currents from antiferromagnets (Sec. II.A.4). La<sub>2</sub>CuO<sub>4</sub> cuprate also exhibits antiferromagnetism and traces of superconductivity, which opens appealing perspectives for superconducting antiferromagnetic spintronics. Rare-earth orthoferrites such as TmFeO<sub>3</sub> also exhibit a (distorted) perovskite structure and canted antiferromagnetism (i.e., weak ferromagnetism). They are known to display a strong temperature-dependent anisotropy. Optical manipulation of the antiferromagnetic order in the terahertz (THz) range was demonstrated (Kimmel *et al.*, 2004). Finally, the properties of antiferromagnetic spinel such as ZnCr<sub>2</sub>O<sub>4</sub> and garnets have been thoroughly investigated (Belov and Sokolov, 1977). In the future, combinations of optics and antiferromagnetic spintronics may produce interesting results.

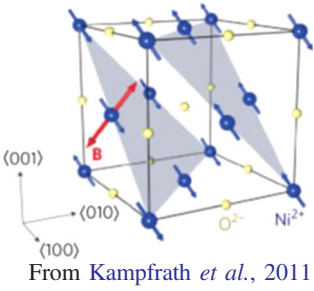
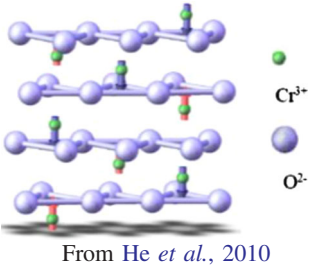
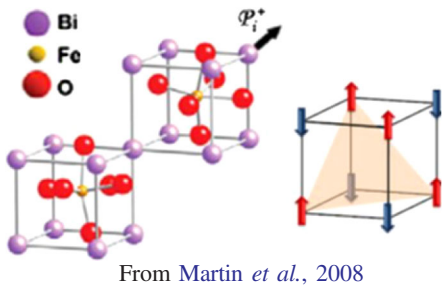
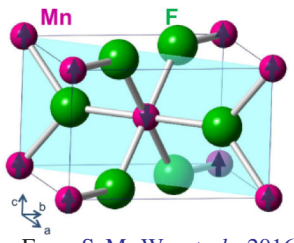
Among insulators, halides such as CuCl<sub>2</sub>, FeCl<sub>2</sub>, MnF<sub>2</sub>, and FeF<sub>2</sub> deserve some mention. Halide antiferromagnets have already proven very useful for the investigation of antiferromagnetic spintronics. In particular, MnF<sub>2</sub> (Jacobs, 1961) and FeCl<sub>2</sub> (Jacobs and Lawrence, 1967) are typical examples of antiferromagnets displaying spin-flop and spin-flip transitions, respectively. Mechanisms related to antiferromagnetic order, such as resonant mode degeneracy, can be switched on and off thanks to these transitions (Hagiwara *et al.*, 1999). They were also recently used to demonstrate the antiferromagnetic spin Seebeck effect (Seki *et al.*, 2015; Rezende, Rodríguez-Suárez, and Azevedo, 2016a; S. M. Wu *et al.*, 2016). Mixed halides such as KNiF<sub>3</sub> perovskite are now attracting attention for optical manipulation of the antiferromagnetic order in the THz range (Bossini *et al.*, 2015).

These examples are only an illustration of the vast complexity of antiferromagnets and more complex frustrated systems (Balents, 2010). Other exotic quantum phases include fractional spinon excitations in CuSO<sub>4</sub> (Mourigal *et al.*, 2013), quantum criticality (Lake *et al.*, 2005; Merchant *et al.*, 2014), and Bose-Einstein condensation of magnons in antiferromagnetic dimers such as TlCuCl<sub>3</sub> halide (Nikuni *et al.*, 2000; Giamarchi, Rüegg, and Tchernyshyov, 2008), or spin liquid phases in antiferromagnetic kagome lattices (Han *et al.*, 2012). The nature of these exotic phases may hold the key to high- $T_c$  superconductivity (Dai, 2015). These fascinating features pertain to the physics of frustrated magnetic systems, which is beyond the scope of the present review.

## 3. Semiconductors and semimetals

Although they have received less attention until now than their metallic and insulating counterparts, semiconducting and semimetallic antiferromagnets (Table III) are another class of important materials for the study of spin transport. For

TABLE II. Crystallographic structure, spin structure, and Néel temperature of some insulating antiferromagnets.

Electrical category	Crystallographic and spin structures (bulk)	Material	$T_{N,bulk}$ (K)	$T_{N,finite\ size}$ (K)
Insulator	 <p>From Kampfrath <i>et al.</i>, 2011</p>	NiO	520	(Abarra <i>et al.</i> , 1996; Lin <i>et al.</i> , 2016; Qiu <i>et al.</i> , 2016)
		CoO	290	(Abarra <i>et al.</i> , 1996; Ambrose and Chien, 1996; Tang <i>et al.</i> , 2003; Molina-Ruiz <i>et al.</i> , 2011; Lin <i>et al.</i> , 2016; Qiu <i>et al.</i> , 2016)
	 <p>From He <i>et al.</i>, 2010</p>	Cr <sub>2</sub> O <sub>3</sub>	310	(Pati <i>et al.</i> , 2016)
	 <p>From Martin <i>et al.</i>, 2008</p>	BiFeO <sub>3</sub>	653	...
	 <p>From S. M. Wu <i>et al.</i>, 2016</p>	MnF <sub>2</sub>	68	...

example, anisotropic magnetoresistance (see Sec. III.A) was detected in semiconducting Sr<sub>2</sub>IrO<sub>4</sub> (crystalline component) (Fina *et al.*, 2014; C. Wang *et al.*, 2014), semimetallic CuMnAs (noncrystalline component) (Wadley *et al.*, 2016), and II-VI semiconducting MnTe (noncrystalline component) (Kriegner *et al.*, 2016). Recently, the first “(ferro)magnet-free” memory prototype with electrical writing and readout was produced with CuMnAs, exploiting the inverse spin galvanic effect for writing and the planar Hall component of the anisotropic magnetoresistance effect for reading (Wadley *et al.*, 2016) (see Sec. III.D.2). The vast number of antiferromagnetic semiconductors, such as Mn(II)-VI, Fe(III)-V, and Gd(III)-V alloys, hold great promise for future research. Among classes of antiferromagnetic semiconductors which have yet to be exploited for antiferromagnetic spintronics, we can list CuFeS<sub>2</sub> (I-IV-III-IV), which has an exceptionally high

Néel temperature of 825 K, MnSiN<sub>2</sub> (II-V-IV-V, 490 K) and LiMnAs (I-II-V, 374 K). Other semiconducting antiferromagnets are listed in Máca *et al.* (2012) and Jungwirth *et al.* (2016). Recently, it was realized that antiferromagnetism may coexist with topologically nontrivial phases of matter, such as Weyl semimetals [e.g., GdPtBi (Hirschberger *et al.*, 2016), Mn<sub>3</sub>Ge, and Mn<sub>3</sub>Sn (Yang *et al.*, 2017), and CuMnAs (Tang *et al.*, 2016)]. This field is expected to be the focus of significant attention in the near future (Šmejkal *et al.*, 2017).

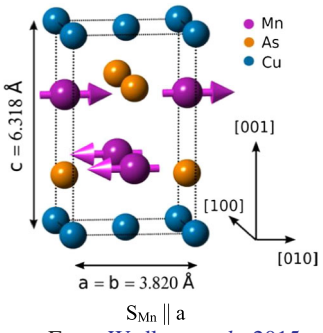
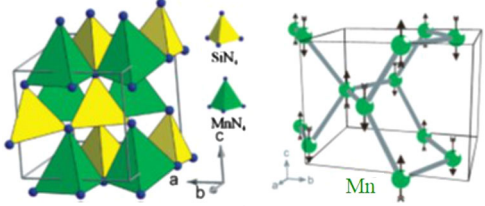
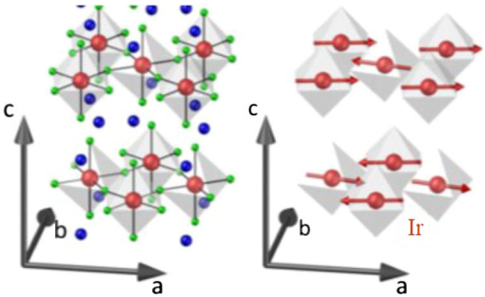
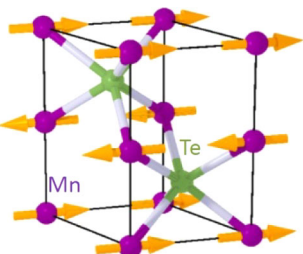
### C. Basics of antiferromagnets

#### 1. Quantum aspects

##### a. A prologue on quantum antiferromagnets

A particularly illustrative example of the thought-provoking character of antiferromagnets concerns the ground state of

TABLE III. Crystallographic structure, spin structure, and Néel temperature of some semimetallic and semiconducting antiferromagnets.

Electrical category	Crystallographic and spin structures (bulk)	Material	$T_{N,\text{bulk}}$ (K)	$T_{N,\text{finite size}}$ (K)
Semiconductor/semimetal	 <p>From Wadley <i>et al.</i>, 2015</p>	CuMnAs	480	...
	 <p>From Esmailzadeh, Hålenius, and Valldor, 2006</p>	MnSiN <sub>2</sub>	490	...
	 <p>From K. Wang <i>et al.</i>, 2015</p>	Sr <sub>2</sub> IrO <sub>4</sub>	240	(Fina <i>et al.</i> , 2014)
	 <p>From Kriegner <i>et al.</i>, 2016</p>	MnTe	323	...

antiferromagnetic chains, represented by a nearest-neighbor Heisenberg Hamiltonian

$$\hat{H} = - \sum_i J_{i,i+1} \mathbf{S}_i \cdot \mathbf{S}_{i+1}. \quad (1)$$

Here the spin operator  $\mathbf{S}_i$  is in units of  $\hbar$  and  $J_{i,i+1}$  is the exchange energy between neighboring sites. In the case of a positive exchange integral  $J_{i,i+1} > 0$ , the system's ground state forms a ferromagnetic chain (such as  $|\uparrow\uparrow\uparrow\cdots\rangle$  or  $|\downarrow\downarrow\downarrow\cdots\rangle$ , i.e., any high spin configuration). In contrast, when the exchange integral is negative  $J_{i,i+1} < 0$ , nearest-neighbor magnetic moments tend to align antiferromagnetically. The antiferromagnetic Heisenberg Hamiltonian, Eq. (1), can be

derived from Hubbard's model in the limit of  $U/t \gg 1$  at half filling [where  $U$  is Hubbard's parameter for electron correlation, and  $t$  is the term describing hopping between nearest neighbors (Anderson, 1959; Takahashi, 1977)]. It would appear logical to assume that the ground state is an antiferromagnetic chain of the form  $|\uparrow\downarrow\uparrow\cdots\rangle$ . However, this is not at all the case. For instance, the ground state of a 4-site spin-1/2 antiferromagnetic chain is given by  $|\uparrow\uparrow\downarrow\downarrow\rangle + |\downarrow\downarrow\uparrow\uparrow\rangle + |\uparrow\uparrow\downarrow\downarrow\rangle + |\downarrow\downarrow\uparrow\uparrow\rangle - 2|\uparrow\downarrow\uparrow\downarrow\rangle - 2|\downarrow\uparrow\downarrow\uparrow\rangle$ . Therefore, the ground state of the antiferromagnetic Heisenberg Hamiltonian is not a collinear antiferromagnetic chain at  $T = 0$  K, as confirmed by experiments (Hirjibehedin, Lutz, and Heinrich, 2006). Hence, quantum antiferromagnets host exotic, strongly correlated excitations, and because of these,

they have been the objects of intense research in condensed matter physics for more than 60 years (Giamarchi, 2003; Balents, 2010). Although this topic is beyond the scope of the present review, we believe that the recent observation of a spinon-mediated spin Seebeck effect in the  $\text{Sr}_2\text{CuO}_3$  one-dimensional antiferromagnet might bridge the gap between antiferromagnetic spintronics and frustrated systems (Hirobe *et al.*, 2016).

### b. Electronic band structure

Although antiferromagnets appear in a wide variety of flavors in terms of crystal symmetries and magnetic textures (Tables I–III), we will illustrate a few of their important aspects by addressing the properties of the simplest paradigm: a collinear bipartite antiferromagnet composed of two interpenetrating square lattices  $A$  and  $B$  possessing antiferromagnetically aligned moments [see Fig. 1(a), the extension to three dimensions is straightforward]. This configuration is usually referred to as a  $G$ -type or checkerboard antiferromagnet, i.e., when both intraplane and interplane couplings are antiferromagnetic (other collinear bipartite spin structures exist, such as the  $A$ -type structure when intraplane coupling is ferromagnetic and interplane coupling is antiferromagnetic, or the  $C$ -type structure when intraplane coupling is antiferromagnetic and interplane coupling is ferromagnetic). Assuming only nearest-neighbor hopping for simplicity, the tight-binding Hamiltonian reads

$$\hat{H} = \sum_{i,j} \{c_{i,j}^+ [\varepsilon_0 + (-1)^{i+j} \Delta \hat{\sigma}_z] c_{i,j} - t(c_{i,j}^+ c_{i+1,j} + c_{i,j}^+ c_{i,j+1} + \text{c.c.})\}, \quad (2)$$

where  $t$  is the hopping parameter, and  $\varepsilon_0$  is the on-site energy. We assume an exchange energy between the itinerant spins and the local moments  $(-1)^{i+j} \Delta$  that is positive and negative on sublattices  $A$  and  $B$ , respectively. It is convenient to rewrite this Hamiltonian in the basis  $(|A\rangle, |B\rangle) \otimes (|\uparrow\rangle, |\downarrow\rangle)$ , which reduces to

$$\hat{H} = \varepsilon_0 \hat{1} \otimes \hat{1} + \gamma_k \hat{\tau}_x \otimes \hat{1} + \Delta \hat{\tau}_z \otimes \hat{\sigma}_z \quad (3)$$

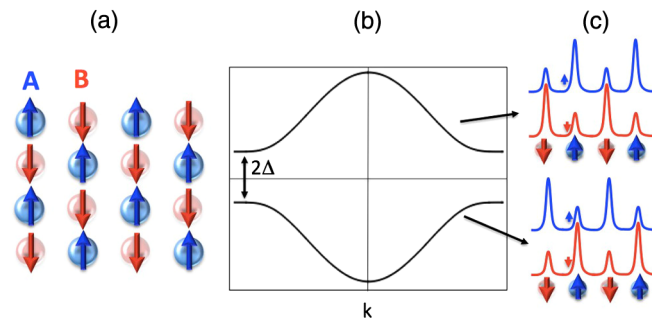


FIG. 1. (a) Schematics of a two-dimensional  $G$ -type antiferromagnet with two sublattices referred to as  $A$  (blue arrows, pointing up) and  $B$  (red arrows, pointing down), (b) electronic band structure, and (c) spatial distribution of the corresponding density of states.

with  $\gamma_k = -2t(\cos k_x a + \cos k_y a)$ . The  $2 \times 2$  Pauli matrices  $\hat{\sigma}_i$ , and  $\hat{\tau}_i$  refer to spin and sublattice subspaces, respectively. It is straightforward to calculate the eigenstates and band structure of this system and one obtains

$$\begin{aligned} \varepsilon_k^s &= \varepsilon_0 + s\sqrt{\gamma_k^2 + \Delta^2}, \\ \psi_s^\sigma &= \frac{1}{\sqrt{2}} \left( \sqrt{1 + s\sigma \frac{\Delta}{\sqrt{\gamma_k^2 + \Delta^2}}} |A\rangle \right. \\ &\quad \left. + s \sqrt{1 - s\sigma \frac{\Delta}{\sqrt{\gamma_k^2 + \Delta^2}}} |B\rangle \right) \otimes |\sigma\rangle, \end{aligned} \quad (4)$$

where  $\sigma$  refers to the spin index, while  $s$  denotes the conduction ( $s = +1$ ) or valence band ( $s = -1$ ). In collinear antiferromagnets, the spin degree of freedom remains a good quantum number, but not the sublattice degree of freedom. Therefore, the eigenstates are a spin-dependent mixture of  $A$  and  $B$  states. Their spatial profile displays a lattice dependent modulation of the density that is spin dependent and band dependent [Figs. 1(b) and 1(c)]. In other words, although the exchange  $(-1)^{i+j} \Delta$  breaks time-reversal symmetry, its combination with spatial translation provides an analogous to Kramers' theorem, which produces two degenerate bands with opposite spins that do not carry spin current. Notice that this property may not hold true for certain noncollinear antiferromagnets, as discussed in Sec. III.C.2. An interesting consequence of this property was pointed out by Haney and MacDonald (2008). At normal metal/antiferromagnet interfaces incident spins may undergo spin flip accompanied by sublattice interchange. This mechanism governs spin-angular momentum transfer at these interfaces as it results in a nonvanishing spin-mixing conductance and thereby spin-transfer torque and magnetoresistance in antiferromagnetic devices (Sec. II).

## 2. Some key parameters

### a. Magnetic susceptibility and Néel temperature

In the course of his exploration of Weiss molecular field theory, Néel (1932, 1938, 1971) and subsequently Bitter (1938) and Van Vleck (1941) addressed the magnetic susceptibility of substances with negative local exchange integrals between collinear moments. These substances were baptized *antiferromagnets* by Bitter (1938). In the mean field approximation, each individual magnetic moment is antiferromagnetically coupled to its nearest neighbors through their mean value field (extension to next-nearest neighbors is straightforward). The energy of the magnetic moment at position  $i$  on sublattice  $A$  reads  $H_i \approx -2J\mathbf{S}_i \cdot \sum_{j \in B} \langle \mathbf{S}_j \rangle = -2Jz\mathbf{S}_i \cdot \langle \mathbf{S}_B \rangle$  (Van Vleck, 1941), where  $z$  is the number of nearest neighbors and  $\langle \mathbf{S}_B \rangle$  is the mean value of the magnetic moments on sublattice  $B$ . In an oversimplified treatment, where magnetic anisotropy is neglected (Kittel, 1976) (a small easy-axis anisotropy is implicit in order to prevent spin flop, see Sec. I.C.3), the magnetization of sublattice  $\alpha$  ( $= A, B$ ) reads

$$M_\alpha = \frac{N}{2} g\mu_B S B_S \left( \frac{4zJ}{k_B T} \frac{SM_\alpha}{g\mu_B N} \right),$$

with

$$B_S(x) = \left( 1 + \frac{1}{2S} \right) \coth \left[ \left( 1 + \frac{1}{2S} \right) x \right] - \frac{1}{2S} \coth \left[ \frac{x}{2S} \right], \quad (5)$$

where  $B_S$  is the Brillouin function,  $S$  is the on-site spin,  $N$  is the number of magnetic atoms per unit volume (assuming that half of these  $N$  belong to one of the two collinear sublattices),  $T$  is the temperature,  $g$  is the  $g$  factor, and  $\mu_B$  is the Bohr magneton. By taking the limit of vanishing magnetization, the Néel temperature can be derived

$$k_B T_N = \frac{2}{3} zJS(1+S). \quad (6)$$

The magnetic susceptibility above the Néel temperature then becomes

$$\chi_{T>T_N} = \mu_0 (g\mu_B)^2 N \frac{S(1+S)}{3k_B} \frac{1}{T+T_N}, \quad (7)$$

where  $\mu_0$  is the vacuum permeability. In contrast to the Curie-Weiss law for ferromagnets, the susceptibility of antiferromagnets does not diverge at the critical ordering (Néel) temperature. Below the Néel temperature, the susceptibility depends on the direction of the field applied with respect to the magnetic order

$$\chi_{\parallel} = \mu_0 \frac{N(g\mu_B S)^2 B'_s \left[ \frac{(2zJ/k_B T) SM/g\mu_B N}{k_B T + 2zJS^2 B'_s \left[ \frac{(2zJ/k_B T) SM/g\mu_B N}{k_B T} \right]} \right]}{k_B T + 2zJS^2 B'_s \left[ \frac{(2zJ/k_B T) SM/g\mu_B N}{k_B T} \right]}, \quad (8)$$

$$\chi_{\perp} = \mu_0 \frac{N(g\mu_B)^2}{4zJ} = \mu_0 \frac{N(g\mu_B)^2}{6k_B T_N} S(1+S).$$

$\chi_{\parallel, \perp}$  is the susceptibility when the external magnetic field is applied parallel or transverse to the order parameter. It is worth noticing that  $\chi_{\parallel} \rightarrow 0$  when  $T \rightarrow 0$ . The parallel susceptibility of MnO measured by [Bizette, Squire, and Tsai \(1938\)](#) was probably the first observation of an antiferromagnetic response to an external field and the demonstration of how different it was from the response of ferromagnets and paramagnets. The qualitative agreement between experimental data for  $\chi_{\parallel}$  and  $\chi_{\perp}$  and the molecular field theory is illustrated in Fig. 2 (for MnF<sub>2</sub>, a collinear coplanar antiferromagnet). Qualitatively similar results were recently obtained when the molecular field theory was extended to noncollinear coplanar antiferromagnets ([Johnston, 2012](#)). It should be noted that exact quantitative agreement with these theories cannot be expected because of the molecular field approximation; e.g., these theories do not include the  $S$  dependence of quantum spin fluctuations. [Johnston \(2012\)](#) and [Van Vleck \(1941\)](#) thoroughly discussed the discrepancies between experiments and their respective theories.

Experimentally, considerable data are available for bulk antiferromagnets, sufficiently thick single layers, or for multiply repeated thinner layers since most techniques are volume sensitive. In contrast, it is much more challenging to determine the magnetic susceptibility and Néel temperature

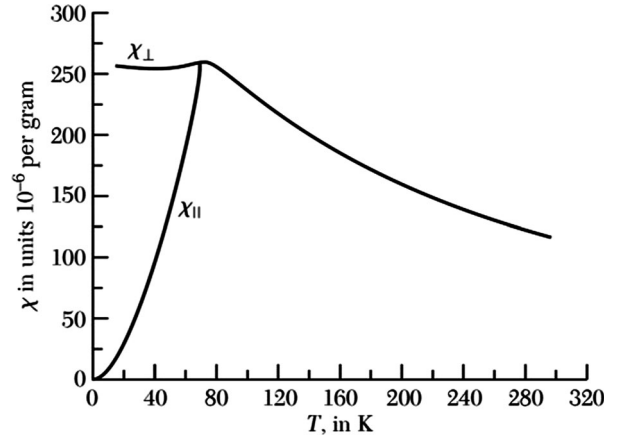


FIG. 2. Representative experimental data for magnetic susceptibility for MnF<sub>2</sub>. From [Kittel, 1976](#).

for a thin film of isolated antiferromagnetic material. Despite the importance of such a basic parameter for antiferromagnetic spintronics and how finite-size effects influence the magnetic susceptibility and the Néel temperature of antiferromagnetic films, very few studies to date have presented quantitative data (Tables I–III). This dearth of data stems from a lack of routinely available rapid measurement techniques compatible with most antiferromagnetic thin films. The next section focuses on this issue.

#### *b. Magnetic phase transition and finite-size scaling*

Theoretical calculations accounting for magnetic phase transitions and finite-size scaling ([Zhang and Willis, 2001](#)) relate size effects to the loss of spin coordination when the size is reduced resulting in smaller critical temperatures. The model takes into account the fact that size effects limit the divergence of the spin-spin correlation length near the critical temperature. As we further detail, intense research efforts are focused on elucidating the impact of ultrathin films on spin-dependent properties, although transition temperatures have yet to be established for these systems. Extrapolating for the case of all-antiferromagnetic [i.e., (ferro)magnet-free] devices ([Petti \*et al.\*, 2013](#)), the order-disorder Néel temperature would set the temperature threshold for data retention. This temperature is defined by the stiffness of the exchange between moments in the antiferromagnet. Sometimes, it is mistakenly confused with the blocking temperature, which is specific to ferromagnetic/antiferromagnetic exchange-bias interaction (see Sec. I.C.3), whereas the Néel temperature is intrinsic to the antiferromagnet ([Berkowitz and Takano, 1999](#); [Nogués and Schuller, 1999](#)). The blocking temperature can easily be determined experimentally, for example, by measuring the disappearance of the hysteresis loop shift as the external temperature rises, or by using specific field-cooling protocols ([Soeya \*et al.\*, 1994](#); [Baltz, Rodmacq \*et al.\*, 2010](#)). In contrast, it is much more challenging to determine the Néel temperature for a thin film of isolated antiferromagnetic material. To the best of our knowledge, neutron diffraction ([Yamaoka, Mekata, and Takaki, 1971](#)), magnetic susceptibility ([Ambrose and Chien, 1996](#)), nanocalorimetry ([Abarra \*et al.\*, 1996](#)), resistivity ([Boakye and Adanu, 1996](#)), and optical measurements



(Saidl *et al.*, 2017) can be used to determine the Néel temperature for sufficiently thick single layers or for superlattices of thinner layers. Alternatively, the Néel temperature can be indirectly determined through experiments involving nonconventional ultrafast measurements of ferromagnetic/antiferromagnetic exchange-biased bilayers. In these bilayers, the ferromagnetic/antiferromagnetic blocking temperature increases with the ferromagnetic material's magnetization sweep rate and can reach the antiferromagnetic intrinsic Néel temperature when measuring in the nanosecond regime (Lombard *et al.*, 2010). However, as with nanocalorimetry, nanostructures must be produced.

Note that the terminology *blocking temperature* is also often used to describe the temperature threshold for superparamagnetism of ferromagnetic or antiferromagnetic grains and particles ( $= KV/k_B$ , where  $K$  is the anisotropy constant,  $V$  is the volume of the grain or particle, and  $k_B$  is the Boltzmann constant). We also note here that ferromagnetic/antiferromagnetic exchange-bias interactions have been extensively studied in an attempt to beat the superparamagnetic limit of ferromagnetic particles (Skumryev *et al.*, 2003).

Some recent experimental works applied alternative methods to determine the Néel temperature (Frangou *et al.*, 2016; Lin *et al.*, 2016; Qiu *et al.*, 2016). These studies found that enhanced spin pumping can be achieved by using a fluctuating spin sink close to its magnetic order transition temperature. The principle of the experiment (Fig. 3) is that the non-equilibrium magnetization dynamics of a spin injector (NiFe) pumps a spin current ( $I_S$  is the spin current density times cross section) into an adjacent layer, called the spin sink (IrMn). This spin sink absorbs the current to an extent which depends on its spin-dependent properties. To eliminate direct exchange interactions and focus only on the effects due to the interaction between the spin current and the spin sink, the injector and the sink are separated by an efficient spin conductor (Cu). The findings were corroborated by recently developed theories which link the enhanced spin pumping into a fluctuating spin sink to interfacial spin-mixing conductance (Ohnuma *et al.*, 2014; Chen *et al.*, 2016). This conductance depends on the transverse spin susceptibility of the spin sink, which is known to vary around critical temperatures (Fig. 2).

Unlike previous techniques (e.g., susceptibility, neutron diffraction, calorimetry) which tend to be volume sensitive,

this method is surface sensitive. By showing that magnetic phase transitions of isolated thin films can be detected by spin pumping, these works open the possibility of further investigation of nontrivial magnetic orders, not limited to antiferromagnetism. For example, the dependence of the IrMn critical temperature on the thickness of this layer was experimentally determined by spotting the spin pumping peak (Fig. 3). This information provided access to a fundamental parameter, the characteristic length for spin-spin interactions. Until now, for isolated IrMn thin films, this parameter had been experimentally inaccessible, and it remains to be measured for a number of common antiferromagnets, including FeMn, PtMn, CuMnAs, and Mn<sub>2</sub>Au (Tables I–III). Size effects also result in a reduction of Néel temperature from larger to smaller grains in polycrystals (even in the 8 nm range). This effect results in a grain-to-grain Néel temperature distribution, which remains to be determined experimentally. Grain sizes are typically the same in antiferromagnetic and ferromagnetic systems, ranging from a few nanometers to a few tens of nanometers. The precise size depends, for example, on sample preparation, thickness, and postdeposition annealing. Examples of grains sizes for CoO and IrMn can be found in Molina-Ruiz *et al.* (2011) and Vallejo-Fernandez, Fernández-Outón, and O'Grady (2008), respectively.

### c. Spatial variability of magnetic properties

Another important finite-size effect relates to variability. Spatial variability of magnetic properties refers to how the magnetic properties are distributed when measured at different spatial locations. In spintronics this problem was raised when the very first generation of magnetic random access memory (MRAM) chips was developed and it has received considerable attention. Most studies focused on the variability of the shapes of memory bits produced during the nanofabrication process (Slaughter, Rizzo, and Mancoff, 2010). As a rule, the use of nanostructures calls for statistical representations, a need which becomes even more pressing when antiferromagnetic materials are involved. This is because both polycrystalline and epitaxial antiferromagnetic films are very sensitive to spin texture faults (due to roughness, atomic stacking faults, etc.) that create randomly spread disordered magnetic phases

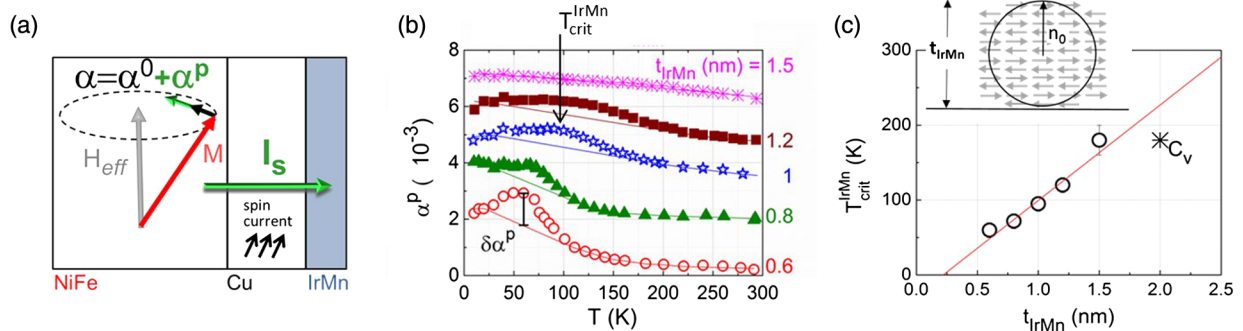


FIG. 3. (a) The spin pumping experiment. (b) Temperature ( $T$ ) dependence of the IrMn spin pumping contribution to NiFe damping ( $\alpha^P$ ). To facilitate reading, data have been shifted vertically. The enhanced spin pumping occurring during the IrMn magnetic phase transition is  $\delta\alpha^P$ . (c) Dependence of  $T_{crit}^{IrMn}$  on  $t_{IrMn}$ , where  $T_{crit}^{IrMn}$  is the critical temperature for the IrMn magnetic phase transition. Data fitting returns the spin-spin correlation length ( $n_0$ ). Adapted from Frangou *et al.*, 2016.

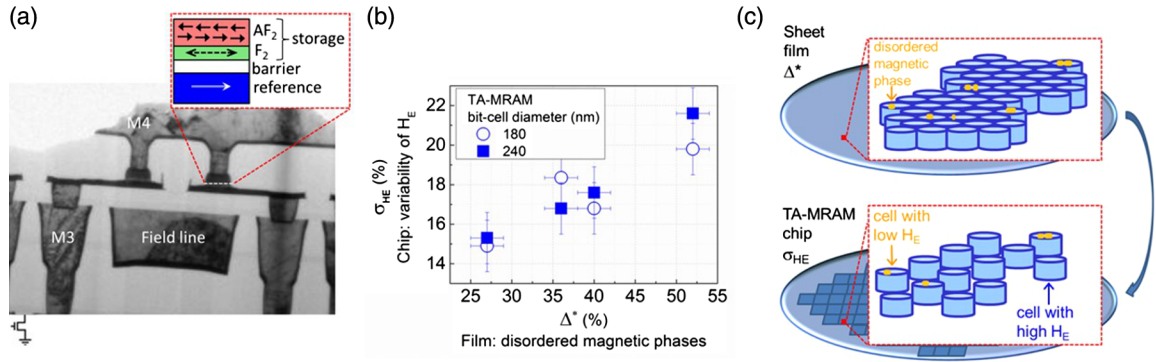


FIG. 4. (a) Transmission electron microscopy (TEM) cross section zoomed on two memory bits of a typical thermally assisted (TA)-MRAM chip on a complementary metal oxide semiconductor with a simplified stack (reference/barrier/{F<sub>2</sub>/AF<sub>2</sub>}). (b) Variability of the ferromagnetic/antiferromagnetic (F<sub>2</sub>/AF<sub>2</sub>) bilayer exchange bias ( $\sigma_{HE}$ ) in memory bits vs proportion of disordered magnetic phases initially present in the film ( $\Delta^*$ ). (c) Sketch showing how disordered magnetic phases are spread over a polycrystalline film and the resulting variability of exchange bias in memory bits when the film is patterned to form memory bits. Adapted from Akmalidinov *et al.*, 2015.

(Takano *et al.*, 1997; Baltz, Rodmacq *et al.*, 2010; Lhoutellier *et al.*, 2015). In addition, lateral finite-size effects on antiferromagnetic materials are not straightforward: lateral size reduction affects the antiferromagnetic domain size, and it also introduces boundaries. These boundaries have two main consequences: they cut the grains located at the edges (in polycrystalline films), thus reducing their volumes (Baltz *et al.*, 2004; Vallejo-Fernandez and Chapman, 2010) and they add unstable disordered magnetic phases along the edges due to the suppression of atomic bonds (this applies to both polycrystalline and epitaxial films) (Baltz, Gaudin *et al.*, 2010).

In MRAM chips, Akmalidinov *et al.* (2015) recently experimentally demonstrated that antiferromagnetic disordered magnetic phases initially present in the film cause nanostructure-to-nanostructure dispersion of the antiferromagnet-related properties when the film is patterned. As a result, each nanostructure is atypical, yielding a large dispersion in device behavior (see Fig. 4).

It is essential to take this variability factor into account through statistical analysis when dealing with the interaction between a current and an antiferromagnetic material in a nanostructure. This analysis can help to avoid drawing conclusions based on potentially misleading individual cases. From the moment that arrays of nanostructures are involved, statistical analysis should be performed when determining spin-transfer, spin-orbit, and spin-caloritronics effects.

### 3. Manipulation by magnetic field, light, and exchange bias

#### a. Manipulation by magnetic field

While antiferromagnetic materials are often reported to be robust against perturbation due to magnetic fields, this does not mean that they are insensitive to magnetic fields. The fact that antiferromagnets can be driven by magnetic fields was briefly introduced in Sec. I.C.2 when we presented magnetic susceptibility. Here we clarify how the magnetic moments in an antiferromagnetic material can be appreciably rotated in a quasistatic manner. We then discuss the dynamics of antiferromagnets and the impact of magnetic field excitation.

A simple but powerful model to describe quasistatic magnetic field manipulation of a bipartite antiferromagnet

is the Stoner-Wohlfarth (Stoner and Wohlfarth, 1948) or coherent rotation model (which was originally developed to describe ferromagnets). In the macrospin approximation, the energy density of one sublattice with uniaxial anisotropy ( $K$ ) and subjected to a magnetic field ( $H$ ) is given by

$$E = J_{AF}M_s^2 \cos(2\phi) + K \cos^2(\phi) - \mu_0 H M_s \cos(\phi), \quad (9)$$

where  $\phi$  is the angle between  $\mathbf{H}$  and the magnetic moments of the sublattice,  $J_{AF}$  is the antiferromagnetic exchange energy, and  $M_s$  is the magnetization of one sublattice. When an external magnetic field is applied perpendicular to the easy axis, the magnetic moments on the two sublattices cant and a net magnetization  $\mathbf{M}$  gradually builds up proportional to the field [Fig. 5(a)]. The net magnetization saturates when the Zeeman energy approximately equals the exchange energy ( $\mu_0 H_{sat} M_s = J_{AF} M_s^2 + K$ ). The scenario is significantly altered when the external field applied is parallel to the easy axis. When the anisotropy energy is small compared to the exchange energy, sublattice magnetization remains in its easy-axis state, with zero net magnetization until the magnetic field compensates the anisotropy. The sublattice magnetization is then free to rotate in directions approximately perpendicular to the easy axis while consuming almost no energy [Fig. 5(a)]. This is known as the spin-flop transition, and it occurs at the spin-flop field  $\mu_0 H_{sf} M_s \approx \sqrt{2K J_{AF} M_s^2}$ . After the transition, the sublattice magnetizations cant increasingly in the direction of the magnetic field and the net magnetization is proportional to the magnetic field [Fig. 5(a)]. When the anisotropy energy is large compared to the exchange energy, net magnetization jumps directly from zero (sublattice magnetic moments antiparallel along the easy axis) to saturation (sublattice magnetic moments parallel along the easy axis). This is known as the spin-flip transition [Fig. 5(a)]. Examples of antiferromagnets with spin-flop [Fig. 5(b)] and spin-flip transitions are MnF<sub>2</sub> (Jacobs, 1961) and FeCl<sub>2</sub> (Jacobs and Lawrence, 1967), respectively. Note that a (spin-flop) field of 9–10 T in MnF<sub>2</sub> is enough to rotate the magnetic moments by 90° [Fig. 5(b)]. Some antiferromagnets need even smaller fields. For example, GdAlO<sub>3</sub> needs only ~1 T (Blazey and Rohrer, 1968) and K<sub>2</sub>[FeCl<sub>5</sub>(H<sub>2</sub>O)] needs

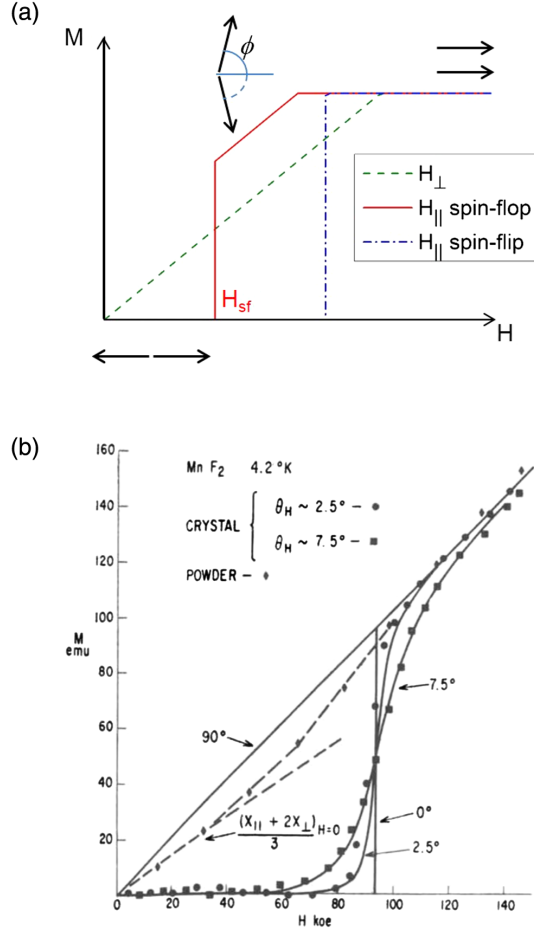


FIG. 5. (a) Diagrammatic representation of antiferromagnetic manipulation by magnetic field. (b) Spin-flop transition measured in  $\text{MnF}_2$ . From [Jacobs, 1961](#).

$\sim 2.6$  T ([Palacio, Paduan-Filho, and Carlin, 1980](#)). On the other hand, for systems such as  $\text{FeF}_2$  the spin-flop field may be as large as  $\sim 42$  T ([Jaccarino \*et al.\*, 1983](#)). The reorientation of an antiferromagnetic sublattice by applying a magnetic field can sometimes be used to determine the magnetic anisotropy of antiferromagnets. The process can also be used as a means to activate and deactivate mechanisms related to antiferromagnetic order, such as resonant mode degeneracy ([Hagiwara \*et al.\*, 1999](#)) [Fig. 6(a)] and the antiferromagnetic spin Seebeck effect ([Seki \*et al.\*, 2015](#); [Rezende, Rodríguez-Suárez, and Azevedo, 2016a](#); [S. M. Wu \*et al.\*, 2016](#)) (Fig. 46).

Let us now turn our attention toward the dynamics of antiferromagnets and the impact of a magnetic field excitation. For the simplest bipartite collinear antiferromagnet, the classical coupled dynamics can be modeled by the phenomenological Landau-Lifshitz-Gilbert equation

$$\begin{aligned} \partial_t \mathbf{m}_A &= -\gamma \mathbf{m}_A \times \mathbf{H}_A + \alpha \mathbf{m}_A \times \partial_t \mathbf{m}_A, \\ \partial_t \mathbf{m}_B &= -\gamma \mathbf{m}_B \times \mathbf{H}_B + \alpha \mathbf{m}_B \times \partial_t \mathbf{m}_B, \end{aligned} \quad (10)$$

where  $\mathbf{H}_\alpha = -\delta_{\mathbf{m}_\alpha} W / M_s$ ,  $\mathbf{m}_\alpha$  is the spin density directional unit vector of sublattice  $\alpha$  ( $\alpha = A, B$ ),  $\gamma$  ( $> 0$ ) is minus the gyromagnetic ratio, and  $W$  is the magnetic energy density of the system including external applied fields, magnetic anisotropy, and

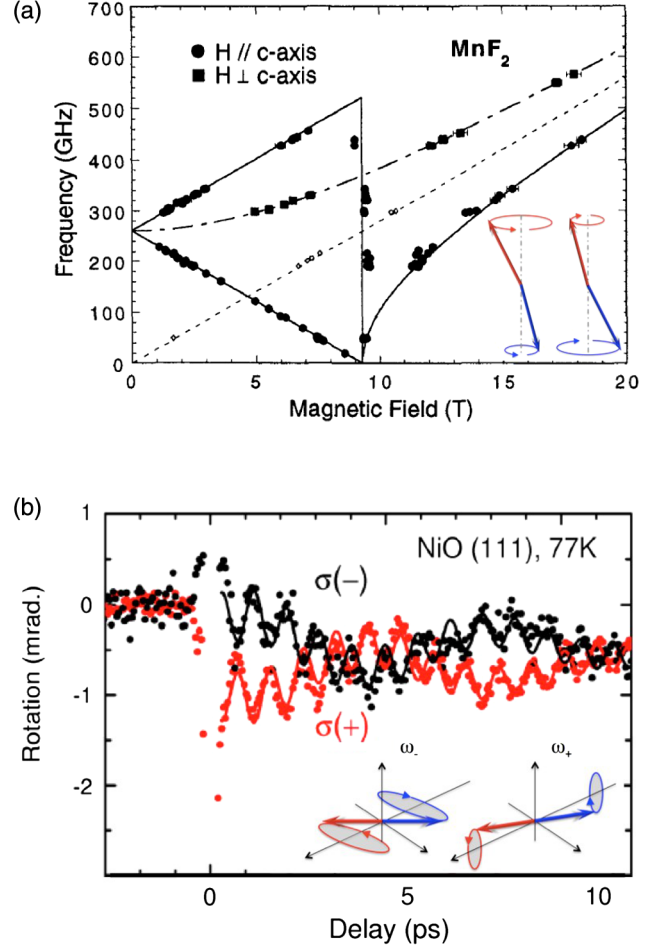


FIG. 6. (a) Field dependence of antiferromagnetic resonance of  $\text{MnF}_2$ . The mode degeneracy is lifted by applying an external field. From [Hagiwara \*et al.\*, 1999](#). (b) Temporal evolution of two mixed spin-wave modes in  $\text{NiO}$ . The rapid oscillations correspond to the out-of-plane mode, while the slow oscillations correspond to the in-plane mode. The insets show the excitation modes. Adapted from [Satoh \*et al.\*, 2010](#).

antiferromagnetic exchange ( $\mu_0 H_E M_s \mathbf{m}_A \cdot \mathbf{m}_B$ ). This simple model leads to a number of important results that we outline later ([Gomonay and Loktev, 2014](#); [Ivanov, 2014](#)).

Let us first consider antiferromagnetic resonance and spin waves. In principle there exist as many excitation modes as basic constituents of the magnetic unit cell. Therefore, diatomic collinear antiferromagnets possess two modes that become nondegenerate in the presence of an external field or magnetic anisotropy ([Kittel, 1951](#); [Nagamiya, 1951](#); [Keffer and Kittel, 1952](#)). In the simplest case where a small field  $H_z$  is applied along the uniaxial anisotropy axis, two circularly polarized modes emerge with frequency

$$\omega = \gamma \mu_0 \sqrt{H_K (2H_E + H_K)} \pm \gamma \mu_0 H_z. \quad (11)$$

Here  $H_K$  is the anisotropy field ( $H_K = 2K / \mu_0 M_s$ ) and  $H_E$  is the exchange field ( $\mu_0 H_E = J_{\text{AF}} S^2 / \mu_B$ ). The resulting frequency is in the range of hundreds of GHz, as shown in Fig. 6(a) for  $\text{MnF}_2$  ( $H_K \sim 0.82$  T,  $H_E \sim 53$  T). Remarkably, these two modes have opposite chirality [see the inset of Fig. 6(a)].

In the case of biaxial anisotropy, such as in NiO ( $T_N \sim 523$  K), the two modes are associated with the different anisotropy constants and referred to as in-plane and out-of-plane modes with respect to the (111) planes (Table II), also referred to as acoustic and optical modes. In NiO(111), the hard-axis ( $\perp$ ) anisotropy along (111) coexists with an in-plane easy-axis ( $\parallel$ ) anisotropy, yielding two different excitations branches,  $\omega_+ = \gamma\mu_0\sqrt{H_E(H_\perp + H_\parallel - Aq^2)}$  and  $\omega_- = \gamma\mu_0\sqrt{H_E(H_\parallel + Aq^2)}$  as displayed in Fig. 6(b) ( $H_\parallel \sim 0.8$  T,  $H_\perp \sim 0.035$  T, and  $H_E \sim 937$  T), where  $q$  is the wave vector and  $A$  is the spin stiffness.

In the absence of anisotropy, the spin-wave dispersion becomes linear  $\omega \sim q$  (see Fig. 7), which has important consequences in terms of spin and heat transport, as discussed further in Sec. IV.B.

Let us now consider the impact of a magnetic field on the dynamics of antiferromagnets. From Eq. (10), one obtains the coupled dynamics of the antiferromagnetic order parameter  $\mathbf{l} = (\mathbf{m}_A - \mathbf{m}_B)/2$  and of the normalized spin density  $\mathbf{m} = (\mathbf{m}_A + \mathbf{m}_B)/2$ . In the limit of large antiferromagnetic exchange,  $\mathbf{m}$  becomes a slave variable such that  $|\mathbf{m}| \ll |\mathbf{l}| \sim 1$  and

$$\mathbf{m} = \frac{1}{\gamma\mu_0 H_E} \mathbf{l} \times \partial_t \mathbf{l} - \frac{1}{H_E} \mathbf{l} \times (\mathbf{H} \times \mathbf{l}). \quad (12)$$

In this case, one can derive the equation of motion for the antiferromagnetic order parameter only, also called the *sigma model* (Ivanov, 2014)

$$\partial_t^2 \mathbf{l} \times \mathbf{l} = \gamma\mu_0 [2(\mathbf{l} \cdot \mathbf{H}) \partial_t \mathbf{l} - (\mathbf{l} \times \partial_t \mathbf{H}) \times \mathbf{l}] + (\gamma\mu_0)^2 (\mathbf{l} \cdot \mathbf{H}) \mathbf{l} \times \mathbf{H} + \gamma\mu_0 \alpha (H_E/2) \mathbf{l} \times \partial_t \mathbf{l}. \quad (13)$$

Anisotropies and spatial inhomogeneities are disregarded here. These are restored in Eq. (16). Several aspects are worth noticing. First and foremost, Eq. (13) is second order in time derivative in sharp contrast with the ferromagnetic Landau-Lifshitz-Gilbert equation that is first order only. Hence, the dynamics of the antiferromagnetic order parameter presents similarities with the inertial dynamics of classical mechanical systems described by Newton's kinetic equation. In other

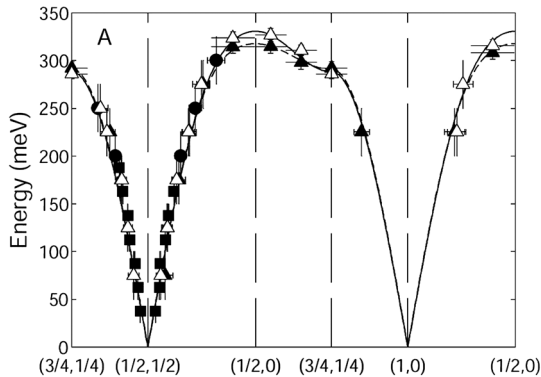


FIG. 7. Energy dispersion of antiferromagnetic spin waves in  $\text{La}_2\text{CuO}_4$ . From Coldea *et al.*, 2001.

words, the kinetic term  $\partial_t^2 \mathbf{l} \times \mathbf{l}$  acts like an acceleration, which has been demonstrated to have a dramatic impact on the dynamics of antiferromagnets and will be discussed later (Wienholdt, Hinzke, and Nowak, 2012; Cheng *et al.*, 2015; Gomonay, Klaui, and Sinova, 2016). It is interesting to note that the fact that the equation of motion for an antiferromagnet is second order follows from the existence of two sublattices [i.e., two first order equations (10) are combined to get one second order equation].

Another noticeable aspect is that damping and anisotropy are both enhanced by the exchange field  $H_E$ . As a consequence, the dynamics of antiferromagnets is much faster than that of their ferromagnetic counterpart (as already noticed) whereas the magnetic damping is also enhanced. Finally, while an external magnetic field acts on the magnetic order parameter  $\mathbf{m}$  in the first order through the term  $\mathbf{l} \times (\mathbf{H} \times \mathbf{l})$  in Eq. (12), its time derivative directly acts on the antiferromagnetic order parameter  $\mathbf{l}$ , through the term  $(\mathbf{l} \times \partial_t \mathbf{H}) \times \mathbf{l}$  in Eq. (13). Notice that a time-independent external magnetic field acts on the antiferromagnetic order parameter  $\mathbf{l}$  in the second order through the term  $(\mathbf{l} \cdot \mathbf{H}) \mathbf{l} \times \mathbf{H}$ , but this effect is of the order of  $(H/H_E)^2 \ll 1$  and is therefore generally negligible.

#### b. Optical manipulation

Because antiferromagnets break time-reversal symmetry, they display linear magnetic dichroism: the absorption of linearly polarized light depends on the orientation of the Néel order parameter. This property can be exploited to observe antiferromagnetic domains (Sec. I.C.4) and to selectively heat different domains and thereby control their extension as recently demonstrated in  $\text{MnF}_2$  (Higuchi and Kuwata-Gonokami, 2016). Nonetheless, dramatic differences between ferromagnetic and antiferromagnetic dynamics have been illustrated by Kimel *et al.* (2004) in  $\text{TmFeO}_3$  orthoferrite and Fiebig, Duong, and Satoh (2004) in NiO. They established the fact that the antiferromagnetic order parameter could be reoriented upon optical excitation. This observation has been recently extended to  $\text{HoFeO}_3$  and interpreted in terms of inertial dynamics (Kimel *et al.*, 2009). As a matter of fact, these materials possess biaxial anisotropy that provides two metastable magnetic states, as well as the Dzyaloshinskii-Moriya interaction that cants the magnetic order and results in a small magnetization. As a consequence, a light-induced time-dependent magnetic field [driven by the inverse magneto-optical Faraday effect (Van der Ziel, Pershan, and Malmstrom, 1965)] triggers the dynamics of the antiferromagnetic order parameter [the second term  $\sim \partial_t \mathbf{H}$  on the right-hand side of Eq. (13)]. Upon inertial motion, the order parameter keeps evolving even after the light pulse is turned off, which drives the order parameter reorientation (see Fig. 8). This inertial switching has been confirmed numerically using atomistic modeling by Wienholdt, Hinzke, and Nowak (2012). In contrast, ferromagnets do not display such an inertial dynamics and, in the absence of thermal activation, can only be switched when a large enough magnetic field is applied over the time scale of the event ( $\sim$  ns). Remarkably though, quantum mechanical calculations of optical excitation of ferromagnets in the *sudden impulse* limit (Popova, Bringer, and Blügel, 2011) show that the optical torque persists on the

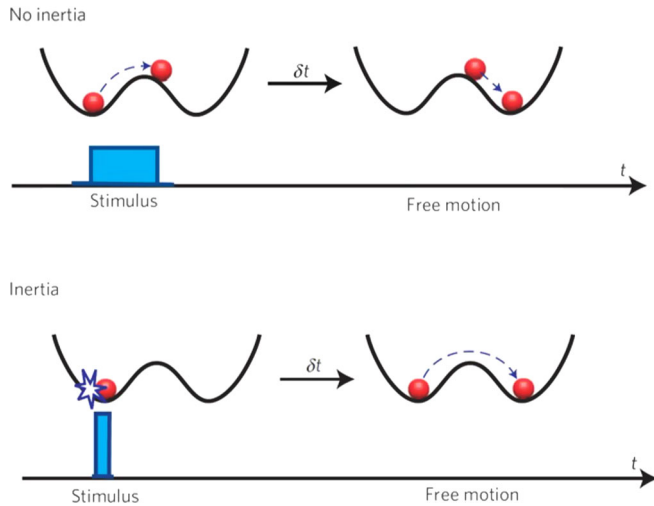


FIG. 8. Difference between noninertial and inertial spin reorientation, typical of ferromagnetic and antiferromagnetic dynamics, respectively. From Kimel *et al.*, 2009.

ferromagnet even after the optical excitation has been removed. This is an alternative description of ultrafast optical switching that goes beyond the simple image of the inverse Faraday effect and beyond inertial effects such as those in antiferromagnets.

The inertial dynamics is also believed to be a key ingredient in the optical manipulation of rare-earth transition-metal ferrimagnets, for example, in GdFeCo (Stanciu *et al.*, 2007), FeTb (Hassdenteufel *et al.*, 2013), and TbCo, DyCo, or HoFeCo (Mangin *et al.*, 2014) alloys. It is however absent in ferromagnets (after an ultrashort field pulse, the magnetization falls back to the lowest energy state). Light-induced switching in transition-metal ferromagnets therefore necessitates some degree of thermal heating (Lambert *et al.*, 2014).

More generally, the investigation of antiferromagnetic spin-wave modes has received significant attention lately with the development of femtomagnetism and THz research [see, e.g., the review article by Kirilyuk, Kimel, and Rasing (2010)]. As a matter of fact, upon optical drive the very high frequency modes of antiferromagnetic insulators can be excited, such as in NiO (Kampfrath *et al.*, 2011; Nishitani, Nagashima, and Hangyo, 2013), MnO (Nishitani, Nagashima, and Hangyo, 2013), or Cr<sub>2</sub>O<sub>3</sub> (Satoh *et al.*, 2007) as well as in rare-earth orthoferrite weak ferromagnets (i.e., canted antiferromagnets), such as DyFeO<sub>3</sub> (Kimel *et al.*, 2005), TmFeO<sub>3</sub> (Kimel *et al.*, 2006), ErFeO<sub>3</sub> (De Jong *et al.*, 2011), YFeO<sub>3</sub> (Zhou *et al.*, 2012), and HoFeO<sub>3</sub> (Mukai *et al.*, 2014). The exploration of the interplay between such radiations and spin transport is still at its infancy and offers perspectives for ultrafast order parameter manipulation and spin-current generation. The present techniques have been demonstrated only for bulk antiferromagnetic materials (or at least a few tens micron thick film) because the absorption signals or the Faraday rotation are proportional to the volume of the sample. It is still a major challenge to detect such excitations in thin films, on which usual spintronic devices are built and where the spin-current related phenomena become dominant. This will be discussed

in the next section where the physics of spin-transfer electronics in antiferromagnets is dealt with.

Conversely Seifert *et al.* (2016) took advantage of the electron spin to produce new THz emitters. In metallic ferromagnet/nonmagnet, and ferromagnet/antiferromagnet (e.g., PtMn bilayers), a femtosecond laser pulse excites electrons in the metal stack, creating a spin-polarized current. A THz electromagnetic transient is then emitted due to the conversion of the spin current into an ultrafast transverse ac charge current in the nonmagnetic metal, through the inverse spin Hall effect. They are currently investigating how the antiferromagnetic order influences the THz emission in antiferromagnet/nonmagnet based emitters (Seifert and Kampfrath, 2017).

### c. Manipulation by exchange bias

Exchange bias refers to magnetic interactions between ferromagnetic and antiferromagnetic materials (Meiklejohn and Bean, 1956; Meiklejohn, 1962). As a result of these interactions, unidirectional anisotropy builds up and creates a hysteresis loop shift. The antiferromagnet is usually regarded as a means to manipulate the ferromagnet through magnetization pinning. In a reciprocal manner the antiferromagnetic order can also be manipulated via exchange bias. In subsequent sections in this paper, we describe demonstrations of antiferromagnetic spintronic effects where exchange bias is used to probe current-induced antiferromagnetic order manipulation (Sec. II.A.2), to excite antiferromagnetic dynamics (Sec. II.B.2), to manipulate the antiferromagnetic order (Sec. III.B), and to combine several antiferromagnetic functionalities (Sec. III.D.4). In this section, we briefly discuss the basis of exchange bias. This presentation is intended to guide readers who may not be familiar with this topic in order to facilitate the understanding of the following sections. Ferromagnetic/antiferromagnetic exchange bias is of course much more complex than the simplistic description given here. Any magnetic frustration due to roughness, grain boundaries in polycrystalline films, or stacking faults will challenge the idealized picture. Interested readers can consult focused reviews where the exchange-bias phenomenon is extensively described (Berkowitz and Takano, 1999; Nogués and Schuller, 1999).

Here we first discuss the intuitive picture and how exchange bias can be manipulated by cooling (domain imprint, Fig. 9). Exchange bias is induced by raising the sample temperature above the blocking temperature ( $T_B$ ) of the ferromagnet/antiferromagnet bilayer and cooling in a field ( $H_{FC}$ ) which is sufficiently large to saturate the magnetization of the ferromagnet. During field cooling, coupling ( $J_{F-AF}$ ) between moments of the ferromagnet and antiferromagnet causes the moments in the antiferromagnet to align with those of the ferromagnet (since  $J_{F-AF} > 0$ ). Below the blocking temperature, the moments in the antiferromagnet remain pinned, regardless of the direction of the moments in the ferromagnet. It is said that the initial ferromagnetic configuration is imprinted in the antiferromagnet during field cooling. Because of coupling, when sweeping the magnetic field at temperatures below the blocking temperature, the configuration where moments in the ferromagnet are parallel to moments in the antiferromagnet is energetically favored compared to the opposite configuration where moments are

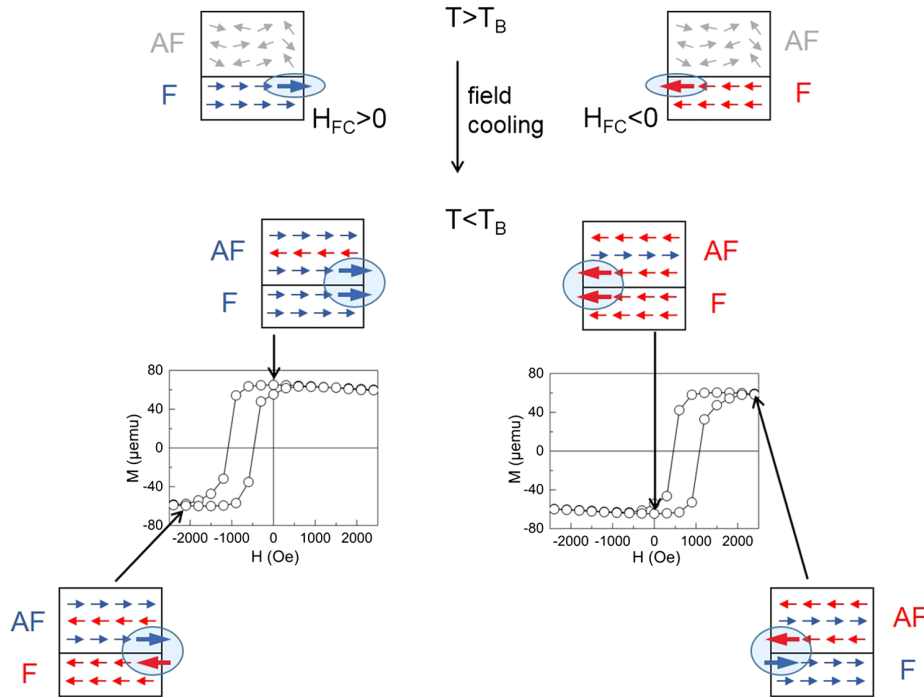


FIG. 9. Intuitive picture of exchange bias and antiferromagnetic order manipulation by field cooling.

antiparallel. As a result, the hysteresis loop of the ferromagnet is shifted by a quantity called the exchange-bias field ( $H_{EB}$ ) (see Secs. II.A.2 and III.D.4). When the exchange-bias field exceeds the coercive field, only one magnetization direction is stable at zero field. This property is widely used to set a reference direction for the spin of conduction electrons in spintronic applications (Dieny, Speriosu, and Parkin, 1991).

Figure 9 illustrates how the direction of the antiferromagnetic order can be manipulated by exchange bias. In fact, the combination of coupling with a ferromagnet and field cooling can be used to direct the antiferromagnetic order. In other words, positive (negative) field cooling imprints a positively (negatively) oriented configuration at the antiferromagnet interface. By field cooling at  $90^\circ$ , it is also possible to imprint configurations at  $90^\circ$  (Sec. III.B). Finally, imprinting multidomain states and magnetic textures in antiferromagnets can be achieved by preparing the ferromagnet in specific magnetic configurations, e.g., multidomain (Brück *et al.*, 2005; Roshchin *et al.*, 2005) and vortex (Salazar-Alvarez *et al.*, 2009; Wu *et al.*, 2011) states. Section I.C.4 is devoted to antiferromagnetic textures.

We now turn our attention to quasistatic manipulation by magnetic field and torques induced by exchange bias (exchange spring). In the picture presented above, the antiferromagnetic order is preserved when magnetization is reversed at temperatures below the blocking temperature. Another simple phenomenon useful for the present review was suggested by Néel (1967) and Mauri *et al.* (1987). When the anisotropy in the antiferromagnet is small compared to the interfacial coupling, the antiferromagnet is no longer magnetically rigid. As a result of the torque exerted by the ferromagnet's magnetization on the antiferromagnet's sublattices, a domain wall parallel to the interface develops, like an exchange spring. Néel and Mauri predictions of

exchange spring have been demonstrated in Co/NiO bilayers (Scholl *et al.*, 2004). This constitutes another means to manipulate the antiferromagnetic order by combining coupling with a ferromagnet and sweeping the magnetization of the ferromagnet with a magnetic field (Sec. III.B).

Finally, exchange bias can also be used to dynamically inject and propagate spin-angular momentum in antiferromagnets. This case will be specifically discussed in Secs. II and IV. As a preliminary example for now, in spin pumping experiments at finite temperatures the precessing magnetization in the ferromagnet pumps the oppositely polarized magnons in the antiferromagnet differently, making magnonic spin transport possible (Rezende, Rodríguez-Suárez, and Azevedo, 2016b); see also Table V.

#### 4. Magnetic textures

Ferromagnetic textures such as domain walls, vortices, and skyrmions are currently attracting a lot of attention due to their rich spin physics and to their potential for three-dimensional electronic devices for storage and logic computing (Allwood *et al.*, 2005; Parkin, Hayashi, and Thomas, 2008; Fert, Cros, and Sampaio, 2013). Magnetic textures also exist in antiferromagnetic materials and interesting differences compared to their ferromagnetic counterparts can be noted. For example, divergent vortices cannot form whenever a ferromagnetic component is present. In contrast, compensated antiferromagnetic materials can form divergent vortices in disks because they do not produce magnetic charges at the disk boundary (Wu *et al.*, 2011). Another example can be found in domain-wall dynamics. Since dipolar coupling is vanishingly small in antiferromagnets, antiferromagnetic domain walls do not exhibit Walker breakdown, thus a “massless” motion of the wall is observed (Gomonay, Jungwirth, and Sinova, 2016). Furthermore, the antiferromagnetic domain walls exhibit a

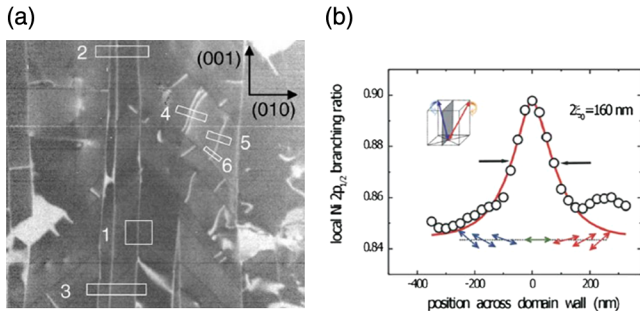


FIG. 10. (a) X-ray linear magnetic dichroism imaging of antiferromagnetic domain walls in NiO. The width of the field of view is about  $35 \mu\text{m}$ . (b) Profile of a domain wall averaged along the wall in region 1. From [Weber \*et al.\*, 2003](#).

relativisticlike motion, which results in a Lorentz contraction of the wall when its velocity approaches the magnon group velocity ([Kim, Tserkovnyak, and Tchernyshyov, 2014](#); [Shiino \*et al.\*, 2016](#)). In this section, we briefly introduce some of the typical antiferromagnetic textures encountered and how these textures can be measured. Manipulation of these textures, in particular, by an electron or a magnon flow, will be discussed in Secs. [II.A](#), [III.D](#), and [IV.C](#).

#### a. Experimental observation of antiferromagnetic textures

While antiferromagnetic textures may show some advantages over ferromagnetic analogs, because they lack net magnetization they are difficult to detect. Direct observation usually requires large scale facilities with element-sensitive techniques like x-ray absorption spectroscopy ([Weber \*et al.\*, 2003](#); [Salazar-Alvarez \*et al.\*, 2009](#); [Wu \*et al.\*, 2011](#)) or specific techniques with local probes like spin-polarized scanning tunneling microscopy ([Bode \*et al.\*, 2006](#); [Loth \*et al.\*, 2012](#)) and quantum sensing with single spins (nitrogen vacancies) in diamond ([Gross \*et al.\*, 2017](#); [Kosub \*et al.\*, 2017](#)). Alternatively, some information about antiferromagnetic domains can be inferred using indirect transport

measurements. For example, this approach was attempted in chromium by [Soh and Kumamuru \(2011\)](#).

Magnetic moments in a domain wall undergo a gradual reorientation. The domain-wall width depends on the exchange, anisotropy, and magnetoelastic energies in the material. Figure 10 shows a 160 nm wide domain wall in antiferromagnetic NiO observed by x-ray linear magnetic dichroism photoelectron emission microscopy ([Weber \*et al.\*, 2003](#)). In this type of material, the formation and properties of walls are dominated by magnetoelastic interactions. Local probes capable of atomic resolution such as spin-polarized scanning tunneling microscopy are needed to further detect details of the spin structure in antiferromagnetic domain walls (Fig. 11). The wide variety of long-range spin structures in antiferromagnets (e.g.,  $3Q$  spin structure, Table I) results in a much wider variety of possible domain-wall configurations in these materials. We note also that controlling the amount of domain walls in an antiferromagnet was demonstrated by [Brück \*et al.\* \(2005\)](#) and [Roshchin \*et al.\* \(2005\)](#) through domain imprinting in ferromagnet/antiferromagnet exchange-biased bilayers (Sec. [I.C.3](#)).

In a magnetic vortex the magnetization vector curls around the center of a confined structure (e.g., disks). The polarity and winding number of the vortex govern its gyroscopic rotation, reversal, and motion. Figure 12 shows curling and divergent vortices in the volume of antiferromagnetic NiO and CoO disks, as measured by x-ray magnetic linear dichroism ([Wu \*et al.\*, 2011](#)). These data are complementary to circular dichroism observations of vortex states in IrMn layers ([Salazar-Alvarez \*et al.\*, 2009](#)), where the signal was produced by the uncompensated moments at the IrMn interface rather than from the moments in the volume of the antiferromagnet. In both experiments, the vortex was imprinted from a ferromagnet into the antiferromagnet via exchange-bias interactions (Sec. [I.C.3](#)).

Finally, the last textures of interest are magnetic skyrmions, which are topological magnetic defects in the magnetization texture. They can be found either in the bulk or at

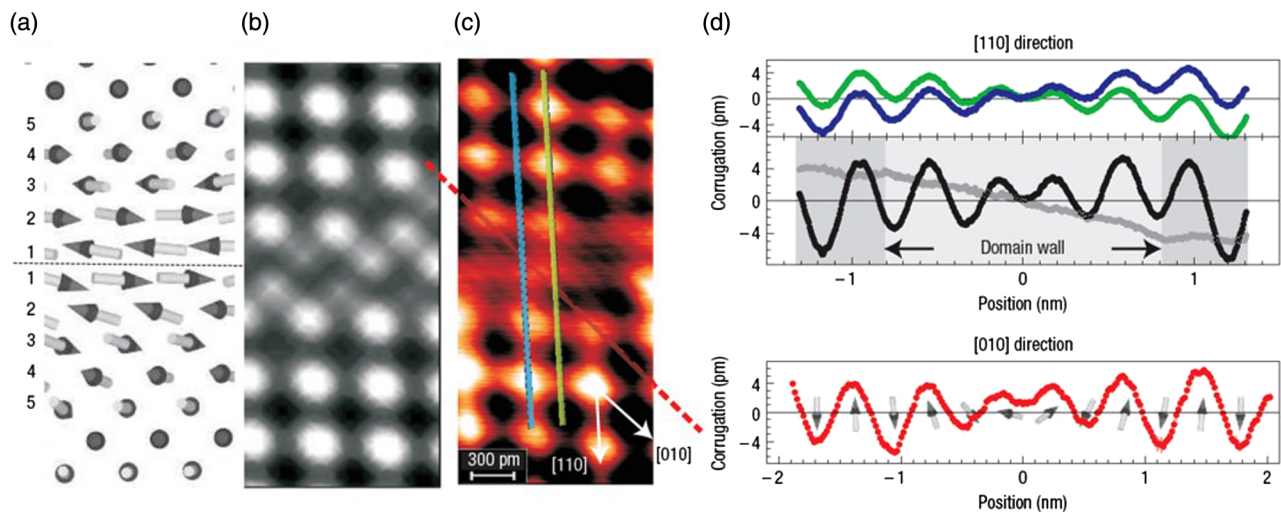


FIG. 11. Domain wall in antiferromagnetic Fe monolayer on W(001). (a) Monte Carlo simulation of the spin structure. (b) Simulated spin-polarized scanning tunneling microscopy images based on the spin structure and (c) corresponding experimental data. (d) Height profiles from (c). From [Bode \*et al.\*, 2006](#).

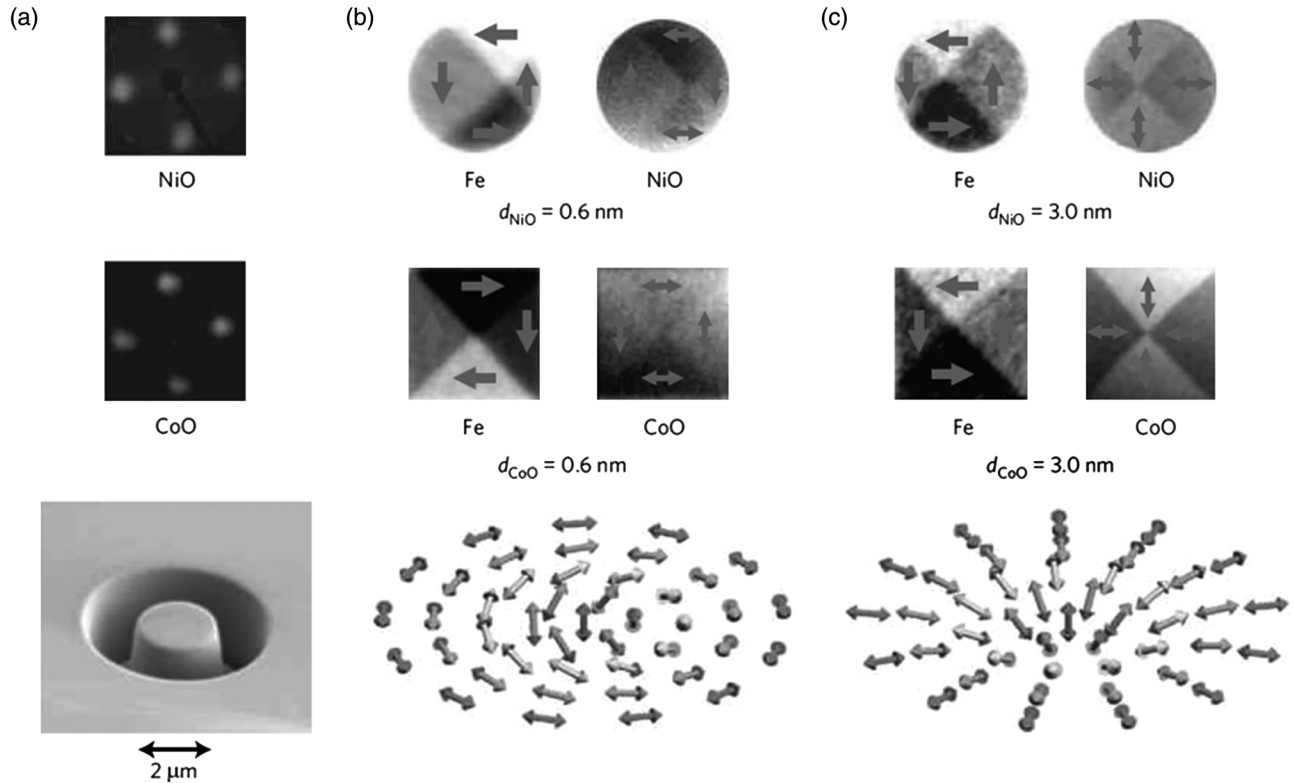


FIG. 12. (a) Low-energy electron diffraction patterns and scanning electron microscope image of single-crystalline NiO/Fe/Ag(001) and CoO/Fe/Ag(001) disks. (b), (c) Element-specific (x-ray magnetic linear dichroism) magnetic-domain images showing (b) curling and (c) divergent vortices (no ferromagnetic analog in disks) in antiferromagnetic NiO and CoO. From Wu *et al.*, 2011.

magnetic interfaces and require either bulk or interfacial Dzyaloshinskii-Moriya interaction (DMI) (Dzyaloshinskii, 1958; Moriya, 1960; Fert and Levy, 1980). Magnetic skyrmions hold great promise for future spintronic applications. They can be as small as a few nanometers, can be energetically much more stable than single domains, and can be created, manipulated, and annihilated electrically. The physics of skyrmions and related applications have been, for example, extensively discussed for the case of ferromagnets by Nagaosa and Tokura (2013) and Fert, Reyren, and Cros (2017). Skyrmions are categorized based on their topological index (also called their winding number) or based on a related quality known as their topological charge. Compared to skyrmions in ferromagnets, the advantage of skyrmions in (bipartite) antiferromagnets is that the topological charges  $G_A$  and  $G_B$  are opposite for each sublattice (Fig. 13). In two dimensions the topological charge of each sublattice is given by  $G \equiv s \int dx dy \mathbf{l} \cdot \partial_x \mathbf{l} \times \partial_y \mathbf{l} \equiv 4\pi s Q$ , where  $s$  is the sublattice spin and  $Q \in \mathbb{Z}$  is the topological index. This opposition cancels the Magnus force and thus eliminates the unwanted transverse velocity, thereby enhancing skyrmion mobility, as computed by Barker and Tretiakov (2016). Since bulk DMI prevails in antiferromagnetic materials, the prospect for skyrmions in antiferromagnets is potentially more promising. Although antiferromagnetic skyrmions have yet to be directly observed, indirect evidence of these textures has been reported (from magnetoresistive data), for example, in  $\text{La}_2\text{Cu}_{1-x}\text{Li}_x\text{O}_4$ , a  $\text{La}_2\text{CuO}_4$  antiferromagnetic insulator doped with Li (Raičević *et al.*, 2011).

### b. Relativistic dynamics

An effective low-energy long-wavelength theory of bipartite antiferromagnets can be developed in terms of the two continuum fields introduced earlier,  $\mathbf{l}(\mathbf{r}, t)$  and  $\mathbf{m}(\mathbf{r}, t)$ . In equilibrium and in the absence of external fields,  $\langle \mathbf{l} \rangle \neq 0$  and  $\mathbf{m} \equiv 0$  in the ordered phase. Under time reversal,  $\mathbf{l} \rightarrow -\mathbf{l}$  and

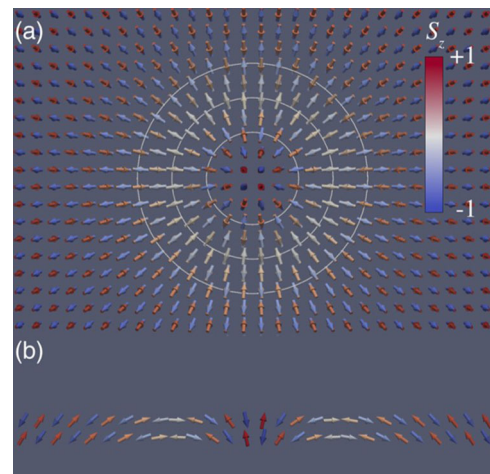


FIG. 13. Computed skyrmions in a  $G$ -type (checkerboard texture) antiferromagnet, analogous to the hedgehog skyrmion state of a ferromagnet but with one sublattice inverted ( $G_A = 1$  and  $G_B = -1$ ). (a) Top view and (b) cross section. The skyrmion radius is 2.1 nm. From Barker and Tretiakov, 2016.



$\mathbf{m} \rightarrow -\mathbf{m}$ , while under the space-group transformation the two sublattices are swapped,  $\mathbf{l} \rightarrow -\mathbf{l}$  and  $\mathbf{m} \rightarrow \mathbf{m}$  (together with a possible global rotation). The textbook Lagrangian density of the simplest isotropic cubic (Heisenberg) antiferromagnet (Auerbach, 1994; Sachdev, 1999) is given by

$$\mathcal{L}[\mathbf{l}, \mathbf{m}] = s\mathbf{m} \cdot \mathbf{l} \times \partial_t \mathbf{l} - \frac{A}{2}(\partial_t \mathbf{l})^2 - \frac{\mathbf{m}^2}{2\chi_\perp} - \mathbf{m} \cdot \mathbf{b}, \quad (14)$$

omitting the topological term (which is not important in two or three spatial dimensions) (Auerbach, 1994; Sachdev, 1999). Here  $s = \hbar S/\mathcal{V}$  is the saturated spin density ( $S$  is the local spin and  $\mathcal{V}$  is the volume per site),  $\mathbf{b} = \gamma s \mu_0 \mathbf{H}$  is the normalized magnetic field,  $A$  is the staggered-order stiffness,  $\chi_\perp$  is the (transverse) magnetic susceptibility, and  $i$  sums over spatial dimensions. Both  $A$  and  $\chi_\perp^{-1}$  are proportional to  $J_{\text{AF}} S^2$ , where  $J_{\text{AF}}$  is the microscopic exchange energy. This Lagrangian sets the stage for the nonlinear sigma model of coarse-grained antiferromagnetic dynamics (in real time  $t$ ) and thermodynamics (in imaginary time  $\tau = it$ ).

The coherent-state functional integration corresponding to the Lagrangian  $\mathcal{L}(\mathbf{l})$  is Gaussian with respect to  $\mathbf{m}$  and can be easily carried out to eliminate it [by completing the associated square in Eq. (14)], resulting in

$$\mathcal{L}[\mathbf{l}] = \frac{\chi_\perp}{2} (s\partial_t \mathbf{l} + \mathbf{l} \times \mathbf{b})^2 - \frac{A}{2} (\partial_t \mathbf{l})^2. \quad (15)$$

To this, local anisotropies can be added as functions of the Néel field  $\mathbf{l}$ ,  $\mathcal{L}_a(\mathbf{l})$ . For an easy-axis anisotropy along an axis  $\mathbf{c}$ , for example,  $\mathcal{L}_a = K(\mathbf{l} \cdot \mathbf{c})^2/2$ , where  $|\mathbf{c}| = 1$  and  $K > 0$ . The equation governing the dynamics of the Néel order parameter is thus

$$\begin{aligned} \mathbf{l} \times (c^2 \partial_t^2 \mathbf{l} - \partial_t^2 \mathbf{l} - \partial_t W_a) &= \frac{1}{s^2} (\mathbf{l} \cdot \mathbf{b}) \mathbf{l} \times \mathbf{b} + \frac{2}{s} (\mathbf{l} \cdot \mathbf{b}) \partial_t \mathbf{l} \\ &\quad - \mathbf{l} \times (\partial_t \mathbf{b} \times \mathbf{l}) + \frac{\alpha}{s\chi_\perp} \mathbf{l} \times \partial_t \mathbf{l}, \end{aligned} \quad (16)$$

where  $c = \sqrt{A/s^2\chi_\perp}$  is the magnon velocity and  $W_a = -L_a/s^2\chi_\perp$ . When  $\mathbf{b}, \alpha \rightarrow 0$ , the spatial and temporal derivatives appear in Lorentz-invariant combinations (Bar'yakhtar and Lvanov, 1983; Haldane, 1983; Ivanov and Kolezhuk, 1995). In other words, Eq. (16) is invariant under the transformations (Kim, Tserkovnyak, and Tchernyshyov, 2014)

$$t \mapsto t' = \frac{t - vx/c^2}{\sqrt{1 - v^2/c^2}}, \quad x \mapsto x' = \frac{x - vt}{\sqrt{1 - v^2/c^2}}. \quad (17)$$

This Lorentz invariance results in the relativisticlike dispersion of the antiferromagnetic spin waves mentioned earlier,  $\omega^2 \sim \omega_0^2 + c^2 q^2$  in uniaxial antiferromagnets. Following this transformation, the profile of the domain wall  $\mathbf{l}_v(x, t)$  can be obtained from the profile of the zero-velocity domain wall  $\mathbf{l}_0(x, t)$  as follows:

$$\mathbf{l}_v(x, t) = \mathbf{l}_0 \left( \frac{x - vt}{\sqrt{1 - v^2/c^2}}, \frac{t - vx/c^2}{\sqrt{1 - v^2/c^2}} \right). \quad (18)$$

Hence, antiferromagnetic domain walls experience Lorentz contraction when their velocity approaches  $c$  (Kosevich, Ivanov, and Kovalev, 1990). This contraction has been detected in both spin torque and magnon-driven domain-wall motion and will be further discussed in Secs. III and IV.

### c. Field-driven manipulation of domain walls

Although the Néel order parameter cannot always be readily manipulated using reasonable (i.e.,  $< 1$  T) static external magnetic fields (see Fig. 5 and corresponding text), different strategies have been proposed to induce domain-wall motion using fields varying in time or space. Gomonay, Klaui, and Sinova (2016) recently proposed exploitation of magnetic pulses. They showed that a magnetic pulse couples efficiently to the antiferromagnetic domain wall via a force  $F \sim \partial_t \mathbf{H} \cdot (\mathbf{l} \times \partial_t \mathbf{l})$ . Therefore, two adjacent walls move synchronously in the same direction. However, the direction of motion depends on the derivative of the magnetic pulse, such that a symmetric pulse induces no overall displacement. In contrast, an asymmetric magnetic pulse can enable “ratchet” motion of the wall (Gomonay, Klaui, and Sinova, 2016). In their work, Gomonay *et al.* introduced a specific example relevant to uniaxial antiferromagnets with high Néel temperature (such as  $\text{Mn}_2\text{Au}$  or  $\text{NiO}$ ), for which the average velocity of domain-wall motion was predicted to be  $0.44 \text{ m s}^{-1}$  for a train of 100 Oe nanosecond pulses.

Finally, we mentioned that Tveten *et al.* (2016) pointed out the potential relevance of the intrinsic magnetization that emerges from the spatial gradient of the Néel order parameter. In fact, they showed that such intrinsic magnetization  $\mathbf{m} \sim -\partial_t \mathbf{l}$  efficiently couples to an external field  $\mathbf{H}$ , such that the force exerted on the domain wall reads  $F \sim \partial_t \mathbf{H} \cdot \partial_t \mathbf{l}$ . Simulations demonstrate that a field gradient of about  $100 \text{ Oe nm}^{-1}$  induces a velocity of about  $50 \text{ m s}^{-1}$ .

## II. SPIN-TRANSFER ELECTRONICS

Spin-transfer electronics encompasses the phenomena resulting from the strong exchange interactions between the spins of conduction electrons and the local moments of the lattice. These effects cover the spin-transfer torque, enabling the electrical manipulation of ferromagnetic materials, for example, via domain-wall motion, and magnetization dynamics and reversal, as well as its Onsager reciprocal—the spin pumping effect—where a precessing magnetization pumps a spin current into an adjacent normal metal. This section reviews whether and how spin-transfer effects create effective torques on antiferromagnetic devices and textures, and how antiferromagnetic dynamics promote spin pumping. Microscopic parameters quantifying the spin-transfer effects, such as spin-mixing conductance and spin penetration depth, are also addressed. Finally, giant and tunneling magnetoresistive effects are discussed.

## A. Spin-transfer torque and spin pumping

### 1. Principle of spin-transfer torque

In ferromagnetic spin valves, tunnel junctions, or magnetic-domain walls, spin-transfer torque arises from the transfer of spin-angular momentum from a flowing spin current to the local magnetic environment. The study of spin-transfer torques in magnetic devices took off when [Slonczewski \(1996\)](#) and [Berger \(1996\)](#) independently predicted current-induced magnetization switching in metallic spin valves. Interested readers may complement their knowledge by consulting the various reviews available on this topic ([Ralph and Stiles, 2008](#); [Brataas, Kent, and Ohno, 2012](#)).

In ferromagnetic systems lacking spin-orbit coupling, spin torque can be expressed as the gradient of spin current, polarized transversally to the local magnetization  $\mathbf{m}$ , i.e.,

$$\boldsymbol{\tau} = -\mathbf{m} \times [(\nabla \cdot \mathbf{J}_s) \times \mathbf{m}], \quad (19)$$

where  $\mathbf{J}_s$  is the spin-current tensor [ $\mathbf{J}_s = (1/\Omega) \sum_n \langle \boldsymbol{\sigma} \otimes \mathbf{v} \rangle_n$ , where  $\Omega$  is the volume of the unit cell and  $\langle \cdots \rangle_n$  denotes the quantum average over states  $n$ ]. When spin relaxation and/or spin-orbit coupling are present, Eq. (19) is no longer valid since spin-angular momentum is not entirely transferred to the local magnetization. In general, it is more convenient to define the spin torque in terms of the torque between the local nonequilibrium spin density  $\delta\mathbf{s}$  and the magnetization,

$$\boldsymbol{\tau} = \frac{2\Delta}{\hbar} \delta\mathbf{s} \times \mathbf{m}, \quad (20)$$

where  $\Delta$  is the exchange parameter between itinerant and local electron magnetic momenta [see Eq. (3)].

In antiferromagnets, the moments' layout is staggered and it is difficult to attribute the spin torque to *total* spin-current absorption. Indeed, the incoming spins precess at different rates about the local magnetic moments of the different sublattices making up the antiferromagnet, resulting in local torques that are equal to the *local* transfer of angular momentum. Hence, to describe spin-transfer torque in antiferromagnets it is necessary to identify the torque exerted on each individual magnetic moment making up the antiferromagnetic unit cell. For instance, in compensated bipartite antiferromagnets, injected spins precess in opposite directions on the different sublattices causing spin torque to occur locally even though there is no overall spin precession at the level of the magnetic unit cell. In general, the torque exerted on a sublattice  $\alpha$  reads

$$\boldsymbol{\tau} = \tau_{\parallel}^{\alpha} \mathbf{m}_{\alpha} \times (\mathbf{p} \times \mathbf{m}_{\alpha}) + \tau_{\perp}^{\alpha} \mathbf{m}_{\alpha} \times \mathbf{p}, \quad (21)$$

where  $\mathbf{m}_{\alpha}$  is the local direction of the magnetic moment of sublattice  $\alpha$  and  $\tau_{\parallel}^{\alpha}$  ( $\tau_{\perp}^{\alpha}$ ) is the (possibly space-dependent) magnitude of the torque component that lies in (out of) the  $(\mathbf{m}_{\alpha}, \mathbf{p})$  plane. The vector  $\mathbf{p}$  is related to the symmetry of the system. For instance in spin valves and tunnel junctions, it represents the direction of the order parameter of the

polarizing layer (either ferromagnetic or antiferromagnetic), while in the context of spin-orbit torques, it is related to the direction of the charge current  $\mathbf{j}_C$  with respect to the symmetry of the structure (e.g.,  $\mathbf{p} \sim \mathbf{z} \times \mathbf{j}_C$  for spin Hall or Rashba torques). In Eq. (21) the first term is usually referred to as the dampinglike torque, while the second term is the fieldlike torque.

A crucial question is “what type of torque can reorient the Néel order parameter”? To address this question we consider three simple situations, depicted in Fig. 14. Figure 14(a) displays the case where an external field  $\mu_0 \mathbf{H}$  is applied perpendicular to the Néel order parameter (for simplicity, anisotropy fields are neglected). Under such a field, the magnetic moment of the two sublattices  $\mathbf{m}_A$  and  $\mathbf{m}_B$  cant in such a way that the torque exerted by the external field on each magnetic moment ( $\boldsymbol{\tau}_H$ ) exactly compensates for the exchange torque exerted by one sublattice on the other ( $\boldsymbol{\tau}_E$ ). The bottom panel shows the same situation represented in terms of the Néel order parameter  $\mathbf{l} = (\mathbf{m}_A - \mathbf{m}_B)/2$  and effective magnetic order parameter  $\mathbf{m} = (\mathbf{m}_A + \mathbf{m}_B)/2$ : the torques  $\sim \mathbf{l} \times \mathbf{m}$  and  $\sim \mathbf{m} \times \mathbf{H}$  compensate each other. Hence, the Néel order parameter cannot be reoriented by the magnetic field (unless one uses a sufficiently strong magnetic field to reach the spin-flop transition, see Sec. I.C.3). Let us now consider a situation where the external field is *staggered*, i.e., of opposite sign on opposite sublattices [Fig. 14(b)]; such a torque can be generated, e.g., in CuMnAs (see Sec. III.D.2). In this case, the staggered field cants the magnetic moments and does not compensate the exchange field, such that the Néel order parameter  $\mathbf{l}$  precesses around the induced magnetization  $\mathbf{m}$ . Similarly, when a dampinglike spin torque is applied [ $\sim \mathbf{m}_{\alpha} \times (\mathbf{p} \times \mathbf{m}_{\alpha})$ ], it also cants the magnetic moments but does not compensate the exchange torque, resulting in precession of the Néel order parameter around the effective magnetization  $\mathbf{m}$ ; see Fig. 14(c).

In other words, the torque that enables reorientation of the Néel order parameter takes the form either of an antidamping torque  $\sim \mathbf{m}_{\alpha} \times (\mathbf{p} \times \mathbf{m}_{\alpha})$  [ $\equiv \mathbf{l} \times (\mathbf{p} \times \mathbf{l})$ ] or that of a staggered fieldlike torque  $(-1)^{\alpha} \mathbf{m}_{\alpha} \times \mathbf{p}$  ( $\equiv \mathbf{l} \times \mathbf{p}$ ), with  $\alpha$  equal to 0 and 1 for sublattices  $A$  and  $B$ , respectively (here we do not consider spin flop as described in Sec. I.C.3 that may also allow reorientation of the order parameter). In both cases, the torque arises from a staggered spin density, i.e., a spin density that changes sign on opposite sublattices. Although the present discussion provides phenomenological arguments about the symmetry of the torque needed to control antiferromagnets, it is oversimplified as it disregards the role of magnetic anisotropies and damping, which are crucial to understanding the actual current-driven dynamics of antiferromagnets. These aspects are discussed in more detail in the next section.

## 2. Manipulation of the order parameter by spin-transfer torque

### a. Antiferromagnetic spin valves

Manipulating antiferromagnets efficiently and reliably is at the heart of all antiferromagnetic spintronics applications ([MacDonald and Tsoi, 2011](#)). For example, a simple switching of an antiferromagnetic order parameter could represent the writing operation of a magnetic random access memory

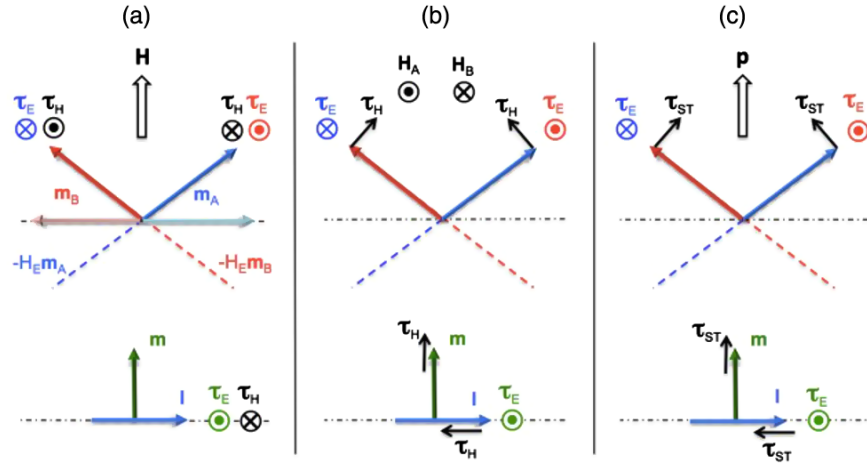


FIG. 14. Illustration of the torques ( $\tau_i$ ) exerted on two antiferromagnetically coupled magnetic moments  $\mathbf{m}_A$  and  $\mathbf{m}_B$ , for three different external forces: upon application of (a) an external field ( $\mathbf{H}$ ), (b) a staggered field ( $\mathbf{H}_A = -\mathbf{H}_B$ ), or (c) a spin-transfer torque [ $\sim \mathbf{m}_\alpha \times (\mathbf{p} \times \mathbf{m}_\alpha)$ ]. In the top panels, the arrows represent the normalized spin direction of the  $A$  and  $B$  sublattices, together with their respective exchange torques. The bottom panels show the effective (field-driven or exchange-driven) torques applied on the induced magnetization  $\mathbf{m}$  and Néel order parameter  $\mathbf{l}$ . In the case of an external field (a), the two torques compensate each other, simply resulting in a static canted configuration, while in the two other cases, (b) and (c), the exchange torque is not compensated and induces reorientation of the Néel order parameter  $\mathbf{l}$ .

based on antiferromagnetic elements. Such a switching of an antiferromagnet may be realized via the so-called spin-transfer torque effect which has been used successfully in ferromagnetic systems to switch magnetic moments by spin currents.

The first prediction of spin-transfer torques in antiferromagnets was made by Núñez *et al.* (2006). They studied spin transport in a one-dimensional metallic spin valve composed of two antiferromagnets separated by a metallic spacer. When injecting a current through the system, a staggered spin density builds up in the first antiferromagnet and is transmitted to the second antiferromagnet. When the two Néel order parameters are misaligned, the transmitted staggered spin density exerts a torque on the local magnetic moments of the second antiferromagnet. The torque computed by Núñez *et al.*, displayed in Fig. 15, produces a large staggered in-plane component and a spatially inhomogeneous out-of-plane component. In addition to the spin torque, they also predicted a magnetoresistive effect arising from spin-dependent quantum interferences in the metallic spacer (see Sec. II.C.1).

Noticeably, both torques extend over the length of the antiferromagnet in this model. Because of the alternating orientations of the moment in the antiferromagnetic layers, no global spin precession occurs at the level of the magnetic unit cell, resulting in a much weaker spin dephasing and therefore a much longer spin penetration length. This is in sharp contrast with ferromagnetic spin valves, where the torque is localized at the interface due to the large spin dephasing of the incoming spin current inside the ferromagnet (Stiles and Zangwill, 2002). Because of the alternating moment orientations in antiferromagnetic layers, commensurate staggered spin density and subsequent torques occur generically. It follows that spin-transfer torques in antiferromagnets can act cooperatively over a longer distance from the interface. This plus the absence of shape anisotropy in antiferromagnetic materials explains that smaller critical currents were predicted for

perfect antiferromagnets compared to ferromagnets (Núñez *et al.*, 2006). Similar results were obtained by first-principle methods on FeMn/Cu/FeMn (Xu, Wang, and Xia, 2008) and Cr/Au/Cr (Haney *et al.*, 2007), which confirmed the non-locality of the spin torque in antiferromagnets. Núñez *et al.* (2006) suggested that the staggered in-plane component of the torque (Fig. 15 top panel) makes electrical manipulation of the Néel order possible. However, as discussed, careful analysis of the Néel order dynamics indicates that it is rather the inhomogeneous out-of-plane torques (Fig. 15 bottom panel) that can be used to manipulate the antiferromagnetic order parameter.

These calculations considered clean metallic multilayers and idealized bipartite antiferromagnetic materials. In contrast, realistic magnetic multilayers possess dislocations, defects, and grain boundaries as well as interfacial roughness, resistivity mismatch, randomly spread spin-glass-like phases at antiferromagnetic interfaces, peculiar spin structures, etc. (Berkowitz and Takano, 1999). These imperfections stimulate quantum decoherence and momentum scattering that dramatically impact the spin transport in antiferromagnetic spin valves. In fact, in contrast to ferromagnetic spin valves, which are well described within incoherent semiclassical models, quantum coherence is crucial to enable the transmission of staggered spin density from one part of the spin valve to the other. Recent tight-binding calculations (Duine *et al.*, 2007; Saidaoui, Manchon, and Waintal, 2014) have indeed demonstrated that spin dephasing and mere spin-independent disorder in the spin valve dramatically quenches the spin torque efficiency (see Fig. 16).

Since dampinglike spin torques make electrical control of the Néel order parameter possible, spin-valve configurations involving a ferromagnetic polarizer rather than an antiferromagnetic should be more promising (Gomonay and Loktev, 2010). Haney and MacDonald (2008) revealed that the torque between the ferromagnet and the antiferromagnet vanishes

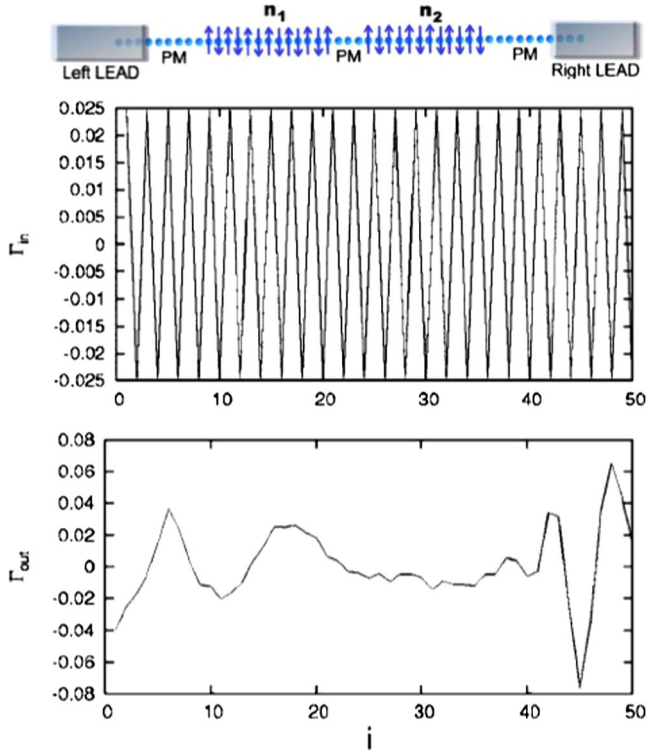


FIG. 15. Spatial profile of the local spin torque in the free antiferromagnetic layer of a one-dimensional spin valve. While the in-plane component is staggered, the out-of-plane component is spatially inhomogeneous, providing an effective nonvanishing torque. The order parameters of the right and left leads are rotated by  $\pi/2$  around the current direction, meaning that the out-of-plane torque points toward the current direction. Adapted from Núñez *et al.*, 2006.

when the ferromagnetic order parameter lies along one of the antiferromagnet's axes of spin-rotation symmetry. In compensated bipartite antiferromagnets, the torque has a  $\sim \sin(2\theta)$  angular dependence (Haney and MacDonald, 2008), while in antiferromagnets with a  $3Q$  spin structure [the  $3Q$  spin structure is, for example, that of  $\text{Ir}_{20}\text{Mn}_{80}$  in the  $L_2$  crystalline phase (see Table I)], the torque adopts the threefold symmetry of the antiferromagnet (Prakhya, Popescu, and Haney, 2014). Interestingly, in both cases they showed that when coherent quantum transport is maintained, the torque exerted by the antiferromagnet on the ferromagnet stabilizes the *perpendicular* configuration of the two magnetic order parameters.

Tight-binding approaches are powerful tools to investigate spin transport in antiferromagnets but lack transparency, particularly to model disordered systems. An alternative is to describe spin transport within the framework of spin-diffusion theory (Manchon, 2017a). This theory assumes that the transport is incoherent (scattering is strong) and parses the spin density in two components: a uniform  $\mathbf{s} = \mathbf{s}_A + \mathbf{s}_B$  and a staggered component  $\delta\mathbf{s} = \mathbf{s}_A - \mathbf{s}_B$ , where  $\mathbf{s}_{A,B}$  is the non-equilibrium spin density on sublattices  $A$  and  $B$ , respectively. The uniform spin density is governed by an anisotropic drift-diffusion equation with respect to the order parameter,

$$\partial_t \mathbf{s} + \vec{\nabla} \cdot \mathbf{J}_s = -\frac{1}{\tau_{sf}} \mathbf{s} - \frac{1}{\tau_\varphi} \mathbf{I} \times (\mathbf{s} \times \mathbf{I}), \quad (22)$$

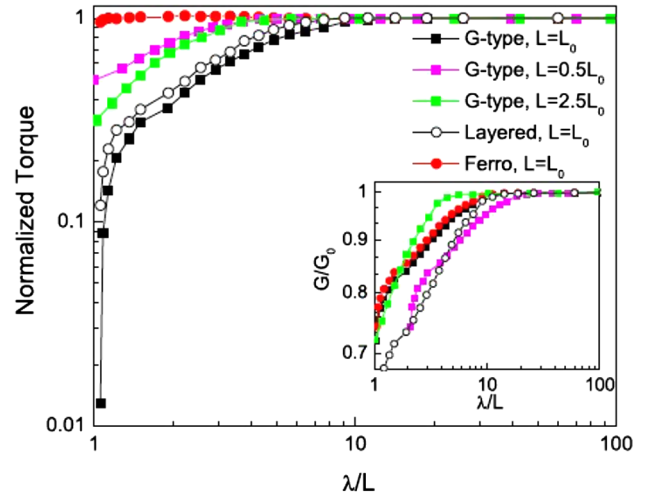


FIG. 16. Dependence of the torque as a function of the mean free path  $\lambda/L$  in the spacer in antiferromagnet/spacer/antiferromagnet spin valves ( $L$  being the length of the spacer).  $G$ -type (checkerboard) and  $A$ -type (layered) antiferromagnets were considered and the case of the ferromagnetic spin valve is given for comparison. From Saidaoui, Manchon, and Waintal, 2014.

where  $J_s$  is the total spin-current density (averaged over the magnetic unit cell); see Eq. (19). The first term on the right-hand side  $\propto 1/\tau_{sf}$  is the isotropic spin relaxation while the second term  $\propto 1/\tau_\varphi$  only relaxes the spin component *transverse* to the Néel order parameter  $\mathbf{I}$ . The latter accounts for the enhanced dephasing of the transverse spin components due to precession around the magnetic moments of the two sublattices. The staggered spin density then reads  $\delta\mathbf{s} = \eta \times \mathbf{s}$ , where  $\eta = \tau^*/\tau_\Delta$  is the ratio between the spin precession time around the magnetic moment of one sublattice  $\tau_\Delta$  and the time the carrier spends on this sublattice  $\tau^*$ . The torque exerted on the Néel order is therefore  $\mathbf{T} = (2\Delta/\hbar)\mathbf{I} \times \delta\mathbf{s}$ . Applying this theory to spin valves and metallic bilayers involving antiferromagnets confirms the results obtained using tight-binding models (Manchon, 2017a). It provides a useful tool to explicitly model spin transport and torque in such systems.

#### b. Antiferromagnetic tunnel junctions

Since spin torque is extremely sensitive to disorder in antiferromagnetic spin valves, one needs to find a way to prevent momentum scattering inside the spacer. This can be done by replacing the metallic spacer by a tunnel barrier (Merodio, Kalitsov *et al.*, 2014a).

Tight-binding models of one-dimensional (Merodio, Kalitsov *et al.*, 2014a) and two-dimensional antiferromagnetic tunnel junctions (Saidaoui, Waintal, and Manchon, 2017) were recently developed. The approach was extended to the case of tunnel junctions with ferrimagnetic electrodes (Merodio, Kalitsov *et al.*, 2014b). In the case of one-dimensional spin valves composed of a ferromagnetic polarizer and an antiferromagnetic free layer (Fig. 17) (Merodio, Kalitsov *et al.*, 2014a), the in-plane torque is found to be staggered as in their metallic counterparts (Fig. 15). In contrast with metallic spin valve though, the out-of-plane torque remains quite large.

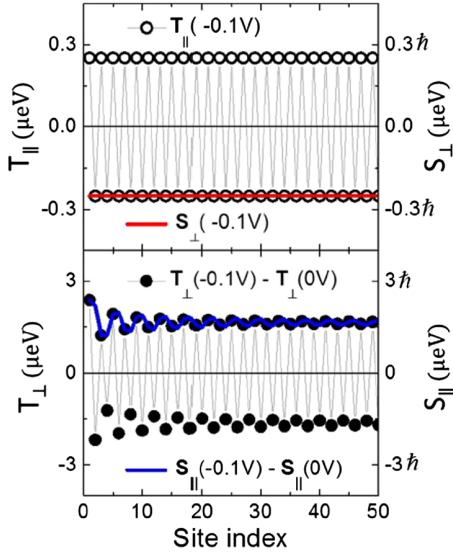


FIG. 17. Spatial distribution of the spin torque (left axis) and associated spin density (right axis) in a ferromagnet/tunnel-barrier/antiferromagnet. From Merodio, Kalitsov *et al.*, 2014a.

In antiferromagnet/tunnel-barrier/antiferromagnet tunnel junctions, the symmetry of the torques is found to be the same as in metallic spin valves and their bias dependence is similar to that in ferromagnetic tunnel junctions (Saidaoui, Waintal, and Manchon, 2017) (Fig. 18). Note that the staggered nature of the in-plane torque (in both metallic and tunneling spin valves) is lost when considering multiple bands (i.e., multiple orbitals, realistic Fermi surface, energy integration) due to enhanced dephasing.

### c. Seeking spin-transfer torque experimentally

The first prediction of antiferromagnetic spin-transfer torque (Núñez *et al.*, 2006) was soon followed by experiments aiming at probing the effects of spin-polarized currents on the antiferromagnetic order parameter. A simple ferromagnet/antiferromagnet (F/AF) bilayer (see Sec. I.C.3) represents a natural test system where an electrical current can be first (spin) polarized by being driven across the ferromagnetic layer and then injected directly into the antiferromagnet. Wei *et al.* (2007) explored the action of a spin current on an antiferromagnet with currents flowing perpendicular to plane across a  $F_s/N/F_{pol}/AF$  polycrystalline spin valve: CoFe(10 nm)/Cu(10 nm)/CoFe(3 nm)/FeMn(8 nm). The subscripts “s” and “pol” stand for “sensing” and “polarizing,” respectively, and N is a “nonmagnetic” metallic spacer. Here  $F_s/N$  is only a probe of the exchange-bias field. In order to achieve high enough current densities a point-contact technique was used.

The key experimental result of Wei *et al.* (2007) is shown in Fig. 19(a). The two-dimensional gray-scale plot shows the spin-valve resistance as a function of the applied magnetic field (down sweeps) and bias current. The transition at a large negative field (between  $-60$  and  $-30$  mT) corresponds to the reversal of  $F_{pol}$  and identifies  $H_{EB}$ ; this transition shifts approximately linearly with the applied current and highlights the dependence of  $H_{EB}$  on the applied current. Similar behavior was also found with IrMn alloys (Basset *et al.*,

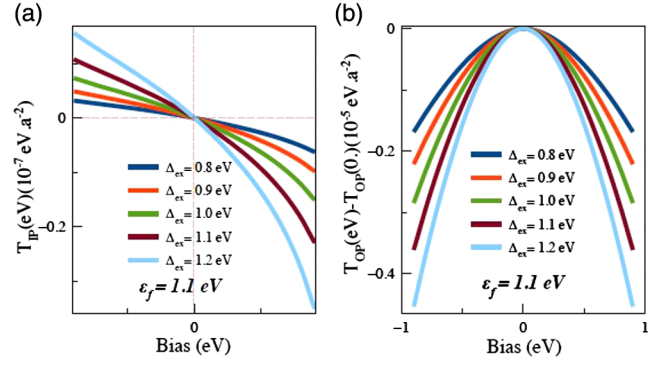


FIG. 18. Bias dependence of the (a) in plane and (b) out of plane in a two-dimensional antiferromagnet/tunnel-barrier/antiferromagnet tunnel junction for different exchange parameters. From Saidaoui, Waintal, and Manchon, 2017.

2008; Wei, Basset *et al.*, 2009). The intuitive picture describing the consequences of spin-transfer torque on an antiferromagnet is shown in Figs. 19(b)–19(d). The picture in Figs. 19(b)–19(d) highlights a major issue for potential applications of ferromagnet/antiferromagnet bilayers in antiferromagnet memory applications. The current-induced changes of antiferromagnetic order are present only as long as the current is present too. As soon as the current is removed the antiferromagnet goes back to its original state just as in an exchange spring. Furthermore, nonuniform current flows inherent to the point-contact technique (Wei *et al.*, 2007) give only a qualitative picture. In addition experiments are sometimes perturbed by unstable antiferromagnetic configurations (Urazhdin and Anthony, 2007) or reconfiguration originating from Joule heating and not spin-transfer torque (Tang *et al.*, 2007, 2010; Dai *et al.*, 2008). New experimental geometries and stacks symmetries need to be proposed to

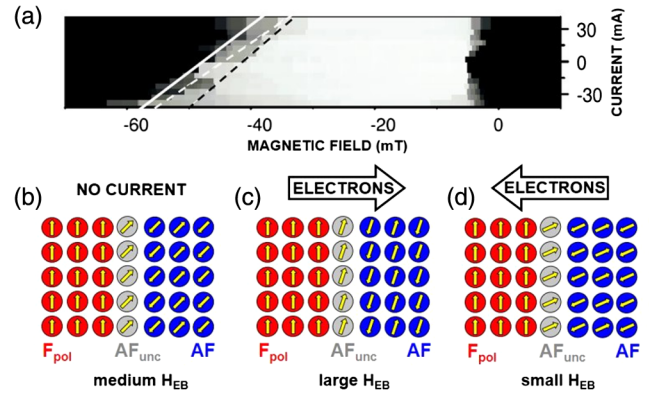


FIG. 19. (a) Two-dimensional gray-scale plot of the spin-valve resistance as a function of the applied magnetic field and bias current. The lighter color indicates higher resistance. Linear fits (see text for details) indicate the trend of exchange-bias field  $H_{EB}$  shift with current. (b)–(d) Intuitive picture of antiferromagnetic spin-transfer torque for a ferromagnet/antiferromagnet ( $F_{pol}/AF$ ) interface. The current gets spin polarized in  $F_{pol}$ . The transmitted (reflected) polarized current applies a torque on the uncompensated AF spins:  $AF_{unc}$ , which rotate away from (toward) the  $F_{pol}$  spins. It influences the  $F_{pol}$  magnetization reversal and results in a reduction (enhancement) of  $H_{EB}$ . From Wei *et al.*, 2007.

obtain quantitative data. The effects of disorder discussed earlier need to be empirically quantified too and possibly minimized.

This first set of experiments provides interesting clues as to the physics involved in exchange-biased ferromagnet/antiferromagnet interfaces but does not constitute a demonstration of antiferromagnetic spin-transfer torque *per se*. As a matter of fact, these experiments reveal the influence of spin-transfer torque on exchange bias, a complex phenomenon that is very sensitive to interface details (Sec. I.C.3), suggesting that the interfacial spin texture can be altered by spin torques. However, these systems remain quite different from the antiferromagnetic spin valves studied theoretically by Núñez and MacDonald (2006) and others. The major challenge that still needs to be addressed is whether spin current can be injected while independently detecting the Néel order parameter response. Up until now, attempts to detect magnetoresistance or torques in antiferromagnetic spin valves have remained unconvincing. As discussed in Sec. III, most of the difficulties can be solved by considering spin-orbit torques, rather than spin-transfer torques.

#### d. Current-driven dynamics

While the dynamics of antiferromagnets under ultrashort field pulses has been addressed in the context of optical manipulation, as introduced in Sec. I.C.3, their dynamics under current drive has only recently attracted interest. As mentioned in the previous section, the spin torque component that controls the antiferromagnetic order parameter arises from a staggered nonequilibrium local spin density and must have the generic form

$$\begin{aligned}\boldsymbol{\tau}_A &= \tau_{\parallel} \mathbf{m}_A \times (\mathbf{p} \times \mathbf{m}_A) + \tau_{\perp} \mathbf{m}_A \times \mathbf{p}, \\ \boldsymbol{\tau}_B &= \tau_{\parallel} \mathbf{m}_B \times (\mathbf{p} \times \mathbf{m}_B) - \tau_{\perp} \mathbf{m}_B \times \mathbf{p},\end{aligned}\quad (23)$$

which results in a torque on the order parameter

$$\partial_t^2 \mathbf{l} \times \mathbf{l}|_{\tau} = \gamma \frac{H_E \tau_{\parallel}}{2} \mathbf{l} \times (\mathbf{p} \times \mathbf{l}) + \gamma H_E \tau_{\perp} \mathbf{l} \times \mathbf{p}. \quad (24)$$

Gomonay and Loktev (2010, 2014) and Gomonay, Kunitsyn, and Loktev (2012) investigated the impact of the dampinglike torque  $\mathbf{l} \times (\mathbf{p} \times \mathbf{l})$  on the dynamics of an antiferromagnet considering various combinations of polarization direction vector  $\mathbf{p}$  and external magnetic field  $\mathbf{H}$  in the case of uniaxial and biaxial anisotropy.

This setup typically corresponds to a ferromagnetic/antiferromagnetic spin valve or to a bilayer composed of an antiferromagnet and a heavy metal with a spin Hall effect (see Sec. III). It is well known that in ferromagnetic spin valves spin transfer torque exerts either a damping or an antidamping effect on the ferromagnetic order parameter, depending on the current direction, leading to either stabilization or destabilization of the magnetic state. In contrast, uniaxial antiferromagnets possess two degenerate excitation modes [see Fig. 6(a)] so that, above a certain critical current density  $|J_{\text{cr}}|$ , one of them is damped while the other is excited. Hence, uniaxial antiferromagnets are excited whatever the direction of the current. Interestingly, the antiferromagnetic order

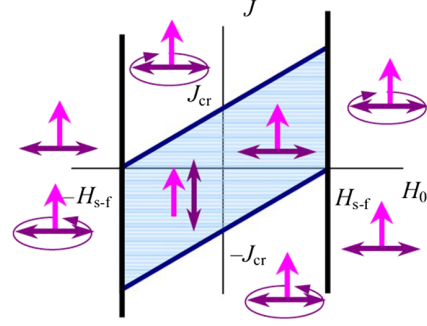


FIG. 20. Stability phase diagram of a ferromagnet/antiferromagnet bilayer. In the central region a bistable state is found where the antiferromagnetic order parameter (double-headed arrow) can be either perpendicular or parallel to the spin-current polarization (single-headed arrow). Above the critical current  $J_{\text{cr}}$  and above the spin-flop field  $H_{\text{s-f}}$ , the system oscillates about the polarization direction. From Gomonay and Loktev, 2010.

parameter tends to align perpendicularly to the polarization, i.e.,  $\mathbf{p} \perp \mathbf{l}$  consistently with Haney and MacDonald (2008) as illustrated in Fig. 20. The critical current above which excitations are triggered (Gomonay and Loktev, 2010) reads

$$J_{\text{cr}} = \frac{\alpha M_s d}{\xi} \omega_{\text{AF}}, \quad (25)$$

where  $\xi/M_s d = \partial \tau / \partial j_c$  is the spin torque efficiency,  $M_s$  is the saturation magnetization of one sublattice, and  $\omega_{\text{AF}} = \gamma \mu_0 \sqrt{H_K H_E}$  is the frequency of the excited mode, typically of the order of a few 100 GHz to 1 THz. Since this frequency is much higher than in ferromagnets ( $\sim$ GHz), the critical current above which such excitations are triggered is about 2 orders of magnitude larger. The case of biaxial or easy-plane anisotropy (e.g., NiO) presents instructive differences. Indeed, in this case the two excitation modes (acoustic and optical modes) are nondegenerate, and they behave differently in the presence of spin-transfer torque (Gomonay and Loktev, 2010). Depending on the configuration, the acoustic mode can be excited while the optical mode is damped. Cheng, Xiao, and Brataas (2016) recently demonstrated that spin Hall torque triggers self-sustained THz oscillations, as further discussed in Sec. III.D.  $\xi/M_s d$  directly relates to the mixing conductance and is therefore comparable to the conductance in ferromagnets. This parameter can be estimated and is of the order of 100 to 1000 Oe for a current density of  $10^8$  A cm $^{-2}$ .

The current-driven excitation of antiferromagnets has also been investigated theoretically by Cheng *et al.* (2015) who reported inertial switching of an antiferromagnet with uniaxial anisotropy under a current pulse. The principle of this switching is similar to that of the pulse field reversal computed by Wienholdt, Hinzke, and Nowak (2012). During the pulse duration, the dampinglike torque applied perpendicularly to the anisotropy axis cants the magnetic moment of the sublattices [see Fig. 14(c)]. Note that this canting remains very small ( $\sim$ 0.1%) due to the large exchange. Thus, energy is transferred from the flowing spin current to the antiferromagnetic exchange. When the dampinglike torque is turned off, the dynamics of the Néel order is triggered and may

switch if a large enough current drive is applied [estimated to be about  $(6-7) \times 10^7$  A cm<sup>-2</sup> in NiO].

Spin-transfer torques were also studied in less conventional structures, e.g., spin-transfer torque on an antiferromagnet sandwiched between two ferromagnets (Linder, 2011). In this case, the direction of the magnetization induced in the antiferromagnet depends on the relative magnetic orientation of the two ferromagnets.

Technical issues are among the main reasons why a direct experimental observation of the dynamics of antiferromagnetic thin films under the influence of a spin current has not been realized in spite of many theoretical predictions. The advancement and development of THz measurement technologies suitable for antiferromagnetic thin films are definitely required (Sec. I.C.3). In order to get around the THz measurement circuitry, downconversion of the measuring frequency to a microwave regime by the exchange coupled ferromagnetic/antiferromagnetic bilayer is again one of the possible schemes to extract the beneficial information of the antiferromagnet dynamics (Moriyama, Takei *et al.*, 2015). Measurement around the spin flopping (Sec. I.C.3) of the antiferromagnetic magnetization may be another alternative since the antiferromagnetic resonant frequency can come down to a microwave range when spin flopping occurs. For instance, MnF<sub>2</sub> alloys exhibit spin flop at around 9 T [Fig. 6(a)] and an antiferromagnetic dynamics is observed at tens of GHz which is comfortably measurable with the conventional microwave circuitry (Ross *et al.*, 2015).

### 3. Moving magnetic textures by spin-transfer torque

Spin-transfer torque can be used to efficiently manipulate antiferromagnetic domain walls and skyrmions. When the antiferromagnetic texture couples to electronic (Hals, Tserkovnyak, and Brataas, 2011; Swaving and Duine, 2011; Cheng and Niu, 2014) or magnonic (Kim, Tserkovnyak, and Tchernyshyov, 2014; Tveten, Qaiumzadeh, and Brataas, 2014) spin flows  $\mathbf{j}_S$ , the dynamic equations derived from the Lagrangian, Eq. (14), acquire additional torques  $\boldsymbol{\tau}$

$$\begin{aligned} s\partial_t \mathbf{l} &= \mathbf{l} \times \mathbf{f}_m + \boldsymbol{\tau}_l, \\ s(\partial_t \mathbf{m} + \alpha \mathbf{l} \times \partial_t \mathbf{l}) &= \mathbf{l} \times \mathbf{f}_l + \mathbf{m} \times \mathbf{f}_m + \boldsymbol{\tau}_m. \end{aligned} \quad (26)$$

Here the effect of the torque  $\boldsymbol{\tau}_l \sim (\mathbf{j}_e \cdot \nabla) \mathbf{l}$  is reduced relative to  $\boldsymbol{\tau}_m \sim \mathbf{l} \times (\mathbf{j}_e \cdot \nabla) \mathbf{l}$  by the small parameters  $\hbar\omega/J_{AF}$ ,  $\mu_B\mu_0 H/J_{AF}$ , which is rooted in the smallness of the susceptibility  $\chi_\perp \propto J_{AF}^{-1}$ . The physical meaning of  $\boldsymbol{\tau}_m$  is self-evident: it is the (local) net transfer of the (spin) angular momentum onto the antiferromagnetic state. In systems with weak spin-orbit coupling, such a transfer of spin is generally associated with hydrodynamic continuity flows. This makes it readily amenable to simple phenomenological treatments as further discussed. The equations of motion (26) have been derived and solved by several authors for the case of an electric drive. It was shown that the steady state velocity is given by the ratio  $\sim \tau_m/\alpha$ , similar to the case of ferromagnetic domain walls (Hals, Tserkovnyak, and Brataas, 2011; Swaving and Duine, 2011; Cheng and Niu, 2014). Yamane, Ieda, and Sinova (2016) recently analytically calculated the torque efficiency using a

tight-binding approach. They showed that a charge current predominantly couples to the Néel order parameter  $\mathbf{l}$  in an exchange-dominant regime, while it couples mostly to the induced magnetization  $\mathbf{m}$  in a mixing-dominant regime.

A convenient way to model the dynamics of magnetic solitons (such as domain walls and skyrmions, Sec. I.C.4) is to track the dynamics of collective coordinates parametrizing the slow modes of the system (Kosevich, Ivanov, and Kovalev, 1990; Tveten *et al.*, 2013; Kim, Tserkovnyak, and Tchernyshyov, 2014). For a rigid translational texture motion  $\mathbf{l}(\mathbf{r}, t) = \mathbf{l}[\mathbf{r} - \mathbf{R}(t)]$ , the momentum  $\mathbf{P}$  canonically conjugate to the center-of-mass position  $\mathbf{R}$  is given (componentwise) by

$$P_i = \partial_{\dot{R}_i} L(\mathbf{R}, \dot{\mathbf{R}}) = - \int dV \pi \cdot \partial_{r_i} \mathbf{l}, \quad (27)$$

where  $L$  is the total Lagrangian associated with the rigid solitonic dynamics with the rigid solitonic dynamics, Eq. (14). The stochastic (solitonic quasiparticle) equations of motion (Kim, Tchernyshyov, and Tserkovnyak, 2015) are then found as

$$\hat{M} \dot{\mathbf{R}} = \mathbf{P}, \quad \dot{\mathbf{P}} + \hat{\Gamma} \dot{\mathbf{R}} = \mathbf{F} + \mathbf{F}^{\text{th}}. \quad (28)$$

Here  $\mathbf{F} \equiv -\partial_{\mathbf{R}} U$  is the deterministic force,  $\hat{\Gamma}$  is the damping tensor with components  $\Gamma_{ij} \equiv \alpha s \int dV (\partial_i \mathbf{l} \cdot \partial_j \mathbf{l})$ , and  $\hat{M} = \tau \hat{\Gamma}$  is the mass tensor, where  $\tau \equiv \rho/\alpha s$  is the viscous relaxation time. The stochastic force obeys the fluctuation-dissipation relation

$$\langle F_i^{\text{th}}(t) F_j^{\text{th}}(t') \rangle = 2k_B T \Gamma_{ij} \delta(t - t'), \quad (29)$$

in the classical limit that is relevant for the slow dynamics. Focusing on the simplest case of an isotropic soliton,  $\hat{M}$  and  $\hat{\Gamma}$  become scalars,  $M$  and  $\Gamma$ . Combining Eqs. (28), we then get a damped stochastic Newton's law

$$\tau \ddot{\mathbf{R}} + \dot{\mathbf{R}} = \mu \mathbf{F} + \boldsymbol{\eta}, \quad (30)$$

where  $\mu \equiv \Gamma^{-1}$  is the mobility and

$$\langle \eta_i(t) \eta_j(t') \rangle = 2D \delta(t - t'). \quad (31)$$

$D \equiv k_B T \mu$  (Einstein-Smoluchowski relation) gives the diffusion coefficient. Magnetic solitons thus undergo an ordinary Brownian motion of massive particles through a viscous medium.

In contrast to the one-dimensional case, motion of the two-dimensional solitons (in the  $x$ - $y$  plane), such as skyrmions, differs drastically in the antiferromagnets compared to the ferromagnets (Barker and Tretiakov, 2016; Zhang, Zhou, and Ezawa, 2016; Göbel *et al.*, 2017), as depicted schematically in Fig. 21. For ferromagnets, Eq. (28) is complemented with a gyrotropic force (Tretiakov *et al.*, 2008; Wong and Tserkovnyak, 2010):

$$(\Gamma - G\mathbf{z} \times) \dot{\mathbf{R}} = \mathbf{F} + \mathbf{F}^{\text{th}}, \quad (32)$$

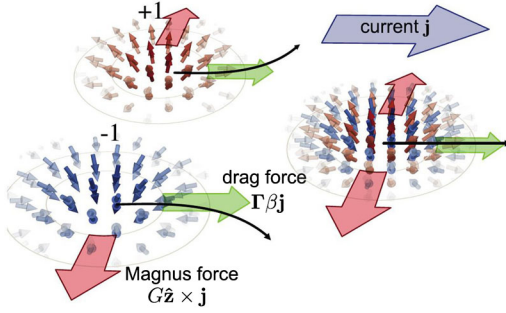


FIG. 21. The Magnus force associated with skyrmion motion (relative to either a static background or an electronic or magnonic flow) is proportional to the topological charge in the ferromagnetic case. This transverse force is absent in antiferromagnets as the topological charge is odd under reversal of the local spin orientation and thus cancels between the two tightly exchange-bound antiferromagnetic sublattices. From [Barker and Tretiakov, 2016](#).

where  $G \equiv s \int dx dy \mathbf{l} \cdot \partial_x \mathbf{l} \times \partial_y \mathbf{l} \equiv 4\pi s Q$ , in terms of the topological (skyrmion) charge  $Q \in \mathbb{Z}$  (Sec. I.C.4). Note also that at the present level of treatment, disregarding possible internal degrees of freedom (apart from the translational motion), ferromagnetic solitons have no inertia (i.e., effectively  $\rho \rightarrow 0$ ). The diffusion coefficient is thus reduced in the ferromagnetic case ([Schütte \*et al.\*, 2014](#))

$$D = k_B T \frac{\Gamma}{\Gamma^2 + G^2}. \quad (33)$$

In the typical case of weak damping  $\alpha \ll 1$ , so that  $\Gamma \ll G$ ,  $D \propto \Gamma/G^2$  and the diffusion coefficient is sped up by increasing the Gilbert damping  $\alpha$ . This is opposite to the antiferromagnetic case  $D \propto 1/\Gamma$ . Brownian motion of ferromagnetic and antiferromagnetic skyrmions was studied numerically by [Barker and Tretiakov \(2016\)](#).

Including additional collective internal degrees of freedom can tremendously enrich the solitonic dynamics. A one-dimensional domain wall in an easy-axis antiferromagnet possesses not only the kinetic energy and inertia associated with its translational motion, but also rotational energy and moment of inertia associated with the precession of the order parameter at the domain-wall center about the easy axis ([Kim, Tserkovnyak, and Tchernyshyov, 2014](#)). The coupled rotational and translational dynamics of such domain walls, as well as their interactions with spin waves [which can induce their motion ([Kim, Tserkovnyak, and Tchernyshyov, 2014](#); [Tveten, Qaiumzadeh, and Brataas, 2014](#))], have the Lorentz symmetry [see Eq. (17) and related text]. The associated effective speed of light is given by the spin-wave velocity. Further insight on the thermal motion of antiferromagnetic textures and their interaction with spin waves is given in Sec. IV.

#### 4. Spin pumping from antiferromagnets

We have seen in the previous section that currents can act on the antiferromagnetic order parameter. The reciprocal phenomenon exists and antiferromagnets can also be used to generate pure spin currents through spin pumping as first

discussed by [Takei \*et al.\* \(2014\)](#). The pumped currents are actually connected to current-induced torques via Onsager reciprocity relations. We remind readers that spin pumping (Sec. I.C.2) results from the nonequilibrium magnetization dynamics of a spin injector, which pumps a spin current [ $\mathbf{J}_s \approx (\hbar/4\pi) g_r^{\uparrow\downarrow} \mathbf{m} \times \partial_t \mathbf{m}$ ] into an adjacent spin sink layer. The initial theoretical framework of spin pumping is built on adiabatic charge pumping and involves the interfacial parameter called spin-mixing conductance ( $g_r^{\uparrow\downarrow}$ ) ([Tserkovnyak, Brataas, and Bauer, 2002](#)); see also Sec. II.B.1. More recently, a linear-response formalism was developed to complete the existing theories and describe spin pumping near thermal equilibrium ([Ohnuma \*et al.\*, 2014](#)). The mixing conductance of a collinear (ferro or antiferro)magnetic system  $g_r^{\uparrow\downarrow}$  is independent of the order parameter and therefore is non-vanishing in antiferromagnets. As a consequence, when an antiferromagnetic order parameter precesses, it also pumps a spin current into the adjacent normal metal of the form

$\mathbf{J}_s \approx (\hbar/4\pi) g_r^{\uparrow\downarrow} \mathbf{l} \times \partial_t \mathbf{l}$  ([Cheng \*et al.\*, 2014](#)), as illustrated in Fig. 22. Furthermore, upon magnetic field rf excitation, antiferromagnetic resonance produces two types of resonances related to two precession modes. These modes are accompanied by a small ferromagnetic component [ $|\mathbf{m}| \sim \sqrt{H_K/H_E}$ , where  $H_K$  is the anisotropy and  $H_E$  corresponds to the exchange interactions between moments in the antiferromagnet, see Eqs. (9) and (11)] that oscillates very fast and can thereby induce an additional spin current [ $\mathbf{J}_s \approx (\hbar/4\pi) g_r^{\uparrow\downarrow} \mathbf{m} \times \partial_t \mathbf{m}$ ]. [Cheng \*et al.\* \(2014\)](#) argued that the smallness of the magnetic moment ( $H_K \ll H_E$ ) is compensated in part by the large precession frequency (THz). A recent spin Seebeck signal in antiferromagnet seems to confirm this concept ([Seki \*et al.\*, 2015](#); [S. M. Wu \*et al.\*, 2016](#)). [Sekine and Nomura \(2016\)](#) recently highlighted nontrivial charge responses resulting from spin excitations in antiferromagnetic insulators with spin-orbit coupling. Because of the time dependences and spatial variations of the antiferromagnetic order parameter they calculated chiral magnetic and anomalous Hall effects, respectively. [Sekine and Chiba \(2016\)](#) took advantage of the reciprocal process to theoretically demonstrate electric-field-induced antiferromagnetic resonance.

Some of the potential pitfalls hampering experimental observation of the proposed phenomena were pointed out by [Cheng \*et al.\* \(2014\)](#). It turns out that the efficiency of the microwave absorption close to resonance is also proportional to  $\sqrt{H_K/H_E}$ , which means that spin pumping is likely to be quenched in antiferromagnets with weak anisotropy, such as  $\text{MnF}_2$  ( $< 0.1$ ) ([Ross, 2013](#)). Antiferromagnets with large  $\sqrt{H_K/H_E}$  ratio such as  $\text{FeF}_2$  ( $\sim 0.6$ ) are promising candidates for the experimental demonstration of spin pumping, as illustrated in Fig. 22 (bottom). Microwave absorption is also maximal when the local easy axis is perpendicular to the oscillating magnetic field excitation. In polycrystalline antiferromagnetic films, spatial dispersion in the anisotropy properties from grain to grain will take the system away from maximal absorption and therefore from maximal spin-current creation. Optimization and control of the spatial variability of magnetic properties (see also discussion in Sec. I.C.2) also contributes to enhancing experimental signals.



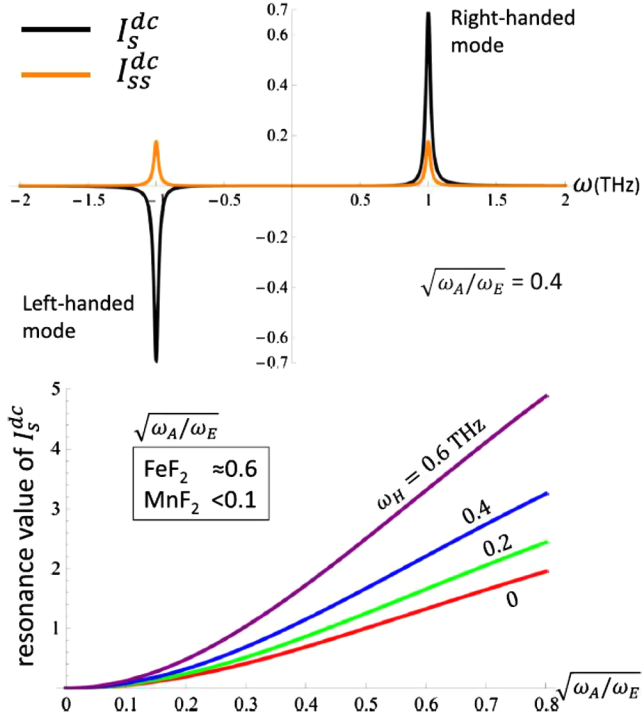


FIG. 22. dc spin pumping calculated at the antiferromagnet's resonance. From Cheng *et al.*, 2014.

Finally, Cheng *et al.* (2014) suggested that microwave absorption could be enhanced by increasing the resonance frequency by applying a magnetic field (Sec. I.C.3) as they noticed that combining high frequency and high absorption efficiency may be difficult to achieve. Johansen and Brataas (2017) showed that some of these limitations can be circumvented in uniaxial antiferromagnets such as MnF<sub>2</sub> and FeF<sub>2</sub> close to the spin-flop transition.

Another appealing way to generate pure spin current is through the spin Hall effect. The spin Hall effect in antiferromagnets is dealt with in Sec. III.C. The spin Seebeck and Nernst effects also make it possible to generate angular momentum currents in antiferromagnets and are dealt with in Sec. IV.A.

## B. Spin-mixing conductance and penetration depths

Whether and how spin currents can be injected and transmitted in antiferromagnets is discussed in this section both theoretically and through the experimental data tabulated in Tables IV and V.

### 1. Spin-mixing conductance at antiferromagnetic interfaces

The interfacial mixing conductance is a parameter quantifying the amount of spin momentum absorbed at magnetic interfaces upon reflection and transmission (Brataas, Tserkovnyak, and Bauer, 2006). This concept is also particularly suitable to describe mechanisms such as spin pumping (see previous section) and spin-transfer torque. Cheng *et al.* (2014) and Takei *et al.* (2014) calculated the reflected mixing conductance (Brataas, Tserkovnyak, and Bauer, 2006),  $g^{\uparrow\downarrow} = S^{-1} \sum_{mn} (\delta_{mn} - r_{mn}^{\uparrow\downarrow} r_{mn}^{\downarrow\uparrow*})$  ( $r_{mn}^{\sigma}$  is the reflection coefficient of a

TABLE IV. Spin-mixing conductance for various interfaces containing antiferromagnets. The investigation temperature was 300 K and values were measured by spin pumping. YIG stands for yttrium ion garnet (Y<sub>3</sub>Fe<sub>5</sub>O<sub>12</sub>).

Interface X/AF	$g_{X/AF}^{\uparrow\downarrow}/S$ (nm <sup>-2</sup> )	Reference
Cu/Ir <sub>20</sub> Mn <sub>80</sub>	10	Ghosh <i>et al.</i> (2012) and Merodio, Ghosh <i>et al.</i> (2014)
Cu/Ir <sub>50</sub> Mn <sub>50</sub>	12	W. Zhang <i>et al.</i> (2014)
Cu/Fe <sub>50</sub> Mn <sub>50</sub>	7	Merodio, Ghosh <i>et al.</i> (2014)
YIG/Ir <sub>20</sub> Mn <sub>80</sub>	0.1–1 (0.43 × YIG/Pt)	Mendes <i>et al.</i> (2014)
YIG/Fe <sub>50</sub> Mn <sub>50</sub>	4.9 ± 0.4	Du <i>et al.</i> (2014a)
YIG/Cr	0.83 ± 0.07	Du <i>et al.</i> (2014a)
YIG/Mn	4.5 ± 0.4	Du <i>et al.</i> (2014a)
YIG/NiO	3.4 <sup>a</sup>	H. Wang <i>et al.</i> (2014)
YIG/NiO	3.2 <sup>b</sup>	H. Wang <i>et al.</i> (2015)
YIG/α-NiFe <sub>2</sub> O <sub>4</sub>	1.6 <sup>b</sup>	H. Wang <i>et al.</i> (2015)
YIG/α-YIG	1.0 <sup>b</sup>	H. Wang <i>et al.</i> (2015)
YIG/Cr <sub>2</sub> O <sub>3</sub>	0.75 <sup>b</sup>	H. Wang <i>et al.</i> (2015)
SrMnO <sub>3</sub> /Pt	0.34–0.49	Han <i>et al.</i> (2014)

<sup>a</sup>Value estimated from  $g_{YIG/AF}^{\uparrow\downarrow}/S = 4\pi M_{S,YIG} t_{YIG} \alpha^p / |\gamma| \hbar$  with literature values for  $M_{S,YIG}$ : 140 kA/m (Zhang and Zou, 2014),  $t_{YIG} = 25$  nm, and  $\alpha^p = 19.1 \times 10^{-4}$  (H. Wang *et al.*, 2014).

<sup>b</sup>Estimated with  $t_{YIG} = 20$  nm (H. Wang *et al.*, 2015) and  $\alpha^p = 18, 9, 6,$  and  $4 \times 10^{-4}$  for NiO, α-NiFe<sub>2</sub>O<sub>4</sub> α-YIG, and Cr<sub>2</sub>O<sub>3</sub>, respectively (H. Wang *et al.*, 2015).

quantum state with spin  $\sigma$  from mode  $m$  to mode  $n$ ) at the interface between antiferromagnets and normal metal using tight-binding models (see Fig. 23).

At first sight, it might seem surprising that the mixing conductance is nonvanishing at such interfaces. This is particularly intriguing in the case of a compensated interface, which does not possess an overall magnetization. However, one needs to notice that the mixing conductance, originally defined for magnetic interfaces, is independent of the magnetization direction and therefore does not have to vanish in collinear antiferromagnets. As a matter of fact, although antiferromagnets do not possess time-reversal symmetry, they are invariant upon the combination of time reversal and crystal symmetry operations, such as translation in bipartite antiferromagnets. Hence, spin mixing occurs through intersublattice (or, equivalently, Umklapp) scattering processes, as revealed by Haney and MacDonald (2008) and Takei *et al.* (2014). Indeed, as discussed in Sec. I.C.1 in the case of the bipartite antiferromagnet, although spin states are degenerate, their wave functions are associated with different superpositions of the two sublattice states. Therefore, a spin-flip event is associated with a flip of the sublattice state.

Saidaoui, Manchon, and Waintal (2014) showed that the potential for electrically injecting a spin current from an antiferromagnet into a normal metal drastically depends on the type of antiferromagnetic texture. Figure 24 shows three configurations: (a) ferromagnetic, (b) *G*-type [or checkerboard texture, as in Fig. 1(a)], and (c) *A*-type antiferromagnets (i.e., layered along the injection direction). Both *A*-type and *G*-type antiferromagnets result in a staggered spin density in reflection, while the transmitted current remains unpolarized. These

TABLE V. Spin penetration depth and resistivity ( $\rho$ ) for various antiferromagnetic materials. Finite-size effects on  $\rho$  are reported when available. Unless specified otherwise, NiFe is close to Ni<sub>81</sub>Fe<sub>19</sub>, the composition of Permalloy, and YIG stands for epitaxial Y<sub>3</sub>Fe<sub>5</sub>O<sub>12</sub>. When not specified the investigation temperature was 300 K. CPP-GMR refer to perpendicular to plane excitation—giant magnetoresistance detection, SP and SP ( $\Delta H$ ) refer to ferromagnetic resonance spin pumping excitation—inverse spin Hall effect detection when not specified, and ferromagnetic resonance linewidth detection when ( $\Delta H$ ) is specified, ST-FMR and ST-FMR (HR) refer to spin torque ferromagnetic resonance excitation induced by spin Hall effect as a result of an ac current flow—anisotropic magnetoresistance detection when not specified, and second harmonic response detection of the anomalous Hall effect and/or anisotropic magnetoresistance when (HR) is specified, and SSE refer to spin Seebeck excitation induced by a thermal gradient—inverse spin Hall effect detection.

AF material	Spin penetration depth (nm)	$\rho$ ( $\mu\Omega$ cm)	Technique	Stack	Reference
Metallic AF in a F/N/AF stack, electronic transport through N					
Ir <sub>20</sub> Mn <sub>80</sub>	0.7	270	SP ( $\Delta H$ )	NiFe/Cu/IrMn	Ghosh <i>et al.</i> (2012) and Merodio, Ghosh <i>et al.</i> (2014)
Ir <sub>50</sub> Mn <sub>50</sub>	0.7 $\pm$ 0.2	293.3	SP	NiFe/Cu/FeMn	W. Zhang <i>et al.</i> (2014)
Ir <sub>20</sub> Mn <sub>80</sub>	$\leq 1$ (4.2 K)	126	CPP-GMR	NiFe/Cu/IrMn/Cu/NiFe	Park <i>et al.</i> (2000) and Acharyya <i>et al.</i> (2010, 2011)
Pd <sub>50</sub> Mn <sub>50</sub>	1.3 $\pm$ 0.1	223	SP	NiFe/Cu/PdMn	W. Zhang <i>et al.</i> (2014)
Fe <sub>50</sub> Mn <sub>50</sub>	$\leq 1$ (4.2 K)	87.5 $\pm$ 5	CPP-GMR	NiFe/Cu/FeMn/Cu/NiFe	Park <i>et al.</i> (2000), Acharyya <i>et al.</i> (2010, 2011), and Dassonneville <i>et al.</i> (2010)
Fe <sub>50</sub> Mn <sub>50</sub>	1.8 $\pm$ 0.5	167.7	SP	NiFe/Cu/FeMn	W. Zhang <i>et al.</i> (2014)
Fe <sub>50</sub> Mn <sub>50</sub>	1.9	135	SP ( $\Delta H$ )	NiFe/Cu/FeMn	Merodio, Ghosh <i>et al.</i> (2014)
Pt <sub>50</sub> Mn <sub>50</sub>	0.5 $\pm$ 0.1	164	SP	NiFe/Cu/PtMn	W. Zhang <i>et al.</i> (2014)
Pt <sub>50</sub> Mn <sub>50</sub>	2.3	119 + 260/ $t_{AF}$ (nm)	ST-FMR (HR)	FeCoB/Hf/PtMn	Ou <i>et al.</i> (2016)
Metallic AF in a F/AF stack, electronic, and magnonic transport regimes					
Ir <sub>25</sub> Mn <sub>75</sub>	0.5	250	ST-FMR	NiFe/IrMn	Soh <i>et al.</i> (2015)
Fe <sub>50</sub> Mn <sub>50</sub>	2	166	ST-FMR (HR)	NiFe/FeMn/Pt	Yang <i>et al.</i> (2016)
Fe <sub>50</sub> Mn <sub>50</sub>	<2 electronic	...	SP	NiFe/FeMn/W	Saglam <i>et al.</i> (2016)
Fe <sub>50</sub> Mn <sub>50</sub>	9 magnonic	...	SP	NiFe/FeMn/W	Saglam <i>et al.</i> (2016)
Cr	2.1	25–325	SSE	YIG/Cr	Qu, Huang, and Chien, (2015)
Cr	4.5 (4.2 K)	180 $\pm$ 20	CPP-GMR	Fe/Cr/Fe	Bass and Pratt (2007)
Cr	13.3	500–1200	SP	YIG/Cr	Du <i>et al.</i> (2014a)
Mn	10.7	980	SP	YIG/Mn	Du <i>et al.</i> (2014a)
Insulating AF in a F/AF stack, magnonic transport					
NiO	1.3	$\gg$	SSE	YIG/NiO/Ta	Lin <i>et al.</i> (2016)
NiO	2.5	$\gg$	SSE	YIG/NiO/Pt	Lin <i>et al.</i> (2016)
NiO	2–5.5 (180–420 K)	$\gg$	SSE	YIG/NiO/Pt	Prakash <i>et al.</i> (2016)
NiO	2	$\gg$	SP	YIG/NiO/Pt	Hahn <i>et al.</i> (2014)
NiO	3.9	$\gg$	SP	YIG/NiO/Pt	Hung <i>et al.</i> (2017)
NiO	9.8	$\gg$	SP	YIG/NiO/Pt	H. Wang <i>et al.</i> (2015)
NiO	10	$\gg$	SP	YIG/NiO/Pt	H. Wang <i>et al.</i> (2014)
NiO	50	$\gg$	ST-FMR	NiFe/NiO/Pt	Moriyama, Takei <i>et al.</i> (2015)
$\alpha$ -NiFe <sub>2</sub> O <sub>4</sub>	6.3	$\gg$	SP	NiFe/ $\alpha$ -NiFe <sub>2</sub> O <sub>4</sub> /Pt	H. Wang <i>et al.</i> (2015)
$\alpha$ -YIG	3.9	$\gg$	SP	NiFe/ $\alpha$ -YIG/Pt	H. Wang <i>et al.</i> (2015)
Cr <sub>2</sub> O <sub>3</sub>	1.6	$\gg$	SP	Cr <sub>2</sub> O <sub>3</sub>	H. Wang <i>et al.</i> (2015)

results show that antiferromagnets are active materials even from the most rudimentary spin transport perspective and call for further first-principle investigations and further investigations of noncollinear antiferromagnets.

Let us now turn our attention toward the experimental determination of interfacial spin-mixing conductance. In a lattice, the transfer of angular momentum between incoming spins and local moments is linked to various mechanisms controlled by several parameters. When entering the antiferromagnet, electron spins experience two types of spin-memory loss mechanisms: spin-flip relaxation and spin dephasing. The former relaxes the spin-angular momentum through the lattice via spin-orbit coupling and magnetic impurities. The latter occurs in magnetic materials (ferromagnets and antiferromagnets) and relaxes the component of the spin density that is transverse to the magnetic order parameter. These various mechanisms determine the manner incident

spins are reoriented upon reflection at the interface and how far they propagate inside the material while retaining their spin state. The former is quantified by the interfacial spin-mixing conductance while the latter is measured in terms of spin penetration depth. Independently of the considerations related to relaxation mechanisms, interfacial spin-mixing conductance and spin penetration depth must be as large as possible to efficiently transmit spin information.

Most frequently, magnetoresistive and dynamic experiments are used to study the parameters controlling the transfer of angular momentum. These experiments are commonly applied to ferromagnetic layers, but they are not ideal for antiferromagnetic films, which display low magnetoresistive signals and require very high frequency (THz) to induce dynamic excitation (see Sec. I.C.3). Early attempts to determine both spin-mixing conductance and characteristic lengths in IrMn and FeMn were conducted using NiFe/Cu/AF/Cu/NiFe spin

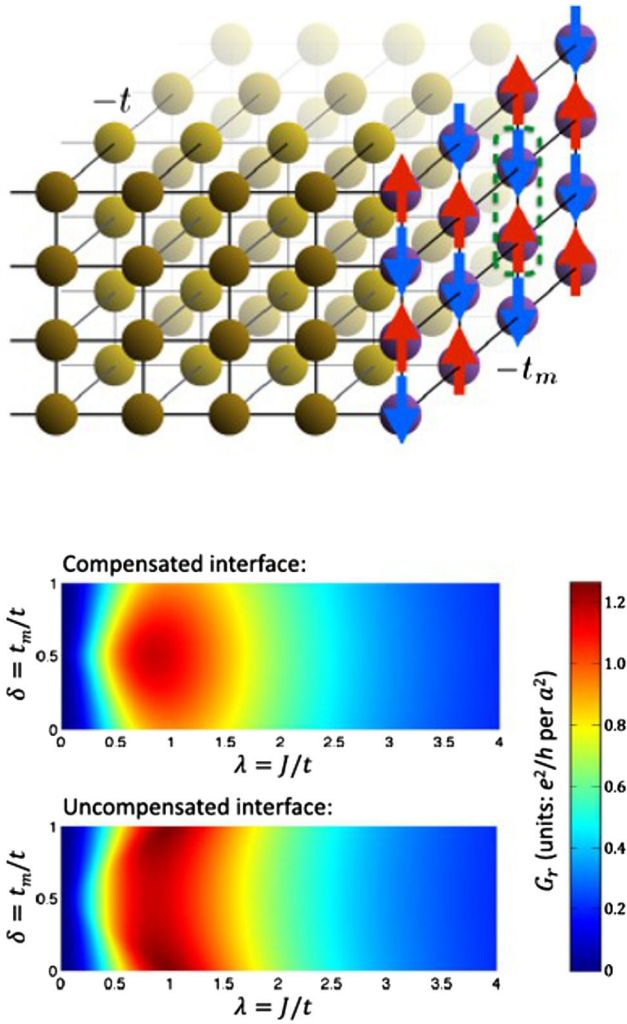


FIG. 23. Mixing conductance calculated at the interface between an antiferromagnet and a normal metal for two types of interfacial magnetic configurations: compensated and uncompensated. Here  $t$  and  $t_m$  are the hopping parameters of the normal metal and antiferromagnet, respectively, and  $J$  is the antiferromagnetic exchange energy. From Cheng *et al.*, 2014.

valves, cryogenic temperatures, fits using drift-diffusion models (Valet and Fert, 1993), and considerations on the magnetoresistance data (Acharyya *et al.*, 2010, 2011). These studies indicated significant spin flipping at (IrMn,FeMn)/Cu interfaces and nanometric spin penetration depths in IrMn and FeMn, although no precise values could be determined.

An alternative method, better suited to antiferromagnetic materials, is based on the absorption of a spin current created by spin pumping from a neighboring ferromagnet. This method has attracted considerable attention owing to its versatility (Tserkovnyak *et al.*, 2005; Ando, 2014). The technique is applicable no matter the magnetic order (ferromagnetism, ferrimagnetism, or antiferromagnetism) and the electrical state (metal, insulator, or semiconductor) of the spin sink. A schematic representation of the experiment is illustrated in Fig. 25 for a NiFe spin injector and an IrMn spin sink. In this method, unlike what was described in Sec. II.A.4, the antiferromagnet is no longer the spin injector but becomes the spin sink. We recall that the spin sink absorbs the current

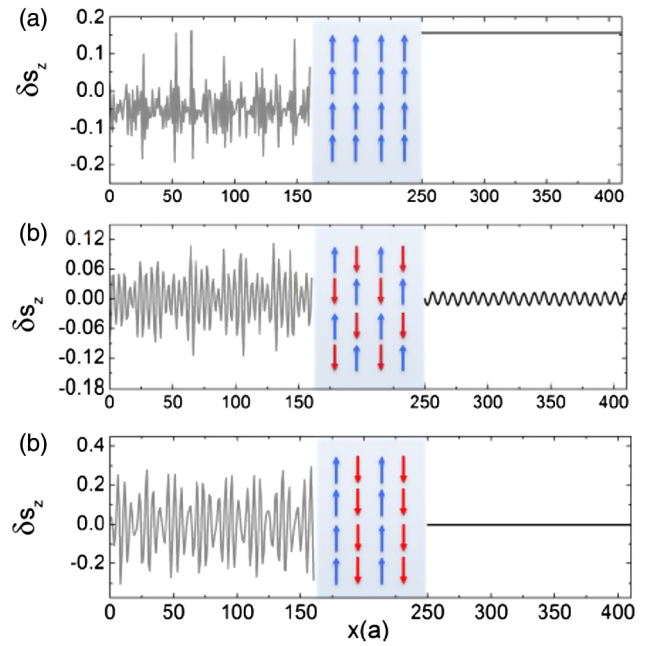


FIG. 24. Spin polarization upon electrical injection through (a) a ferromagnet, (b) a  $G$ -type antiferromagnet, and (c) an  $A$ -type antiferromagnet. From Saidaoui, Manchon, and Waintal, 2014.

to an extent that depends on its spin-dependent properties (Tserkovnyak, Brataas, and Bauer, 2002). In practice, ferromagnetic resonance generally drives the magnetization dynamics in these systems.

The interfacial spin-mixing conductance can be recorded from spin pumping experiments [Figs. 25(a) and 25(b)] based on the difference in ferromagnetic damping ( $\alpha^P$ ) compared to a reference sample with no spin sink ( $\alpha^0$ ). Table IV lists the spin-mixing conductance measured for various interfaces containing antiferromagnets. The interpretation of Table IV is certainly not straightforward. The spin-mixing conductance can be very sensitive to the quality of the interface and therefore to the nature and quality of the stacking. Structure dependent spin-mixing conductance were shown by Tokaç *et al.* (2015). Different measurements, furthermore, yield an effective spin-mixing conductance which is convoluted with the spin relaxation and/or spin Hall physics away from the interface. This, for example, limits the level of comparison between insulating-YIG/metallic-IrMn and metallic-Cu/metallic-IrMn bilayers.

## 2. Spin penetration depths and relaxation mechanisms

The spin penetration depth in the spin sink can be recorded by measuring the thickness dependence of the changes induced in the ferromagnetic damping  $\alpha^P$  [Fig. 25(b)]. Alternatively, the inverse spin Hall contribution to the transverse voltage ( $V$ ) can be used to deduce spin penetration depths. This contribution results from the spin-to-charge current conversion ( $I_C$ ) occurring directly in the antiferromagnetic spin sink (Saitoh *et al.*, 2006) [see Fig. 25(c)] or in the topmost capping layer in the case of insulating antiferromagnets. We deal specifically with the physics of the spin Hall effect in antiferromagnetic layers in Sec. III.C.2. For now,

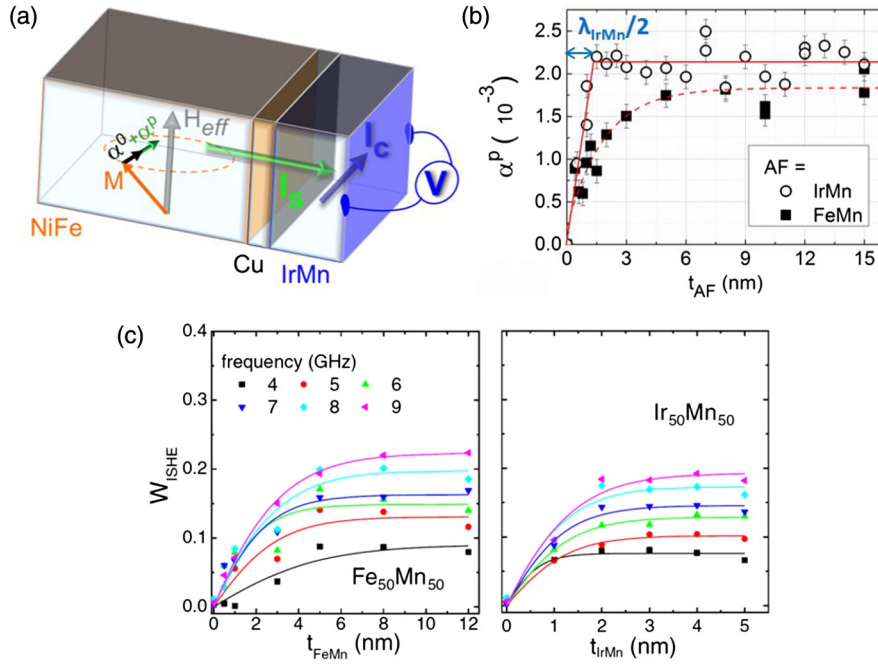


FIG. 25. (a) Schematic representation of the experiment performed with a NiFe spin injector, a Cu spin conductor (to eliminate direct exchange interactions) and an IrMn spin sink. In reflection conditions, the NiFe damping is the sum of local intrinsic damping ( $\alpha^0$ ) and additional nonlocal damping ( $\alpha^P$ ) associated with the spin sink. In transmission conditions, the inverse spin Hall effect converts the spin current ( $I_S$ ) to a charge current ( $I_C$ ) in the antiferromagnetic spin sink. (b) Dependence of  $\alpha^P$  on spin sink thickness ( $t_{AF}$ ) for  $Ir_{20}Mn_{80}$  and  $Fe_{50}Mn_{50}$  antiferromagnets. The spin penetration depth in the spin sink is  $\lambda_{IrMn,FeMn}$ . Adapted from Merodio, Ghosh *et al.*, 2014. (c) Relationship between the inverse spin Hall contribution ( $W_{ISHE}$ ) to the dc voltage ( $V$ ) measured across the  $Ir_{50}Mn_{80}$  and  $Fe_{50}Mn_{50}$  spin sink layers and  $t_{AF}$ . The measured voltage  $V$  is the result of several contributions: a contribution due to anisotropic magnetoresistance ( $V_{AMR}$ ) and a contribution due to the inverse spin Hall effect ( $V_{ISHE}$ ).  $W_{ISHE}$  is defined as  $1/(1 + V_{AMR}/V_{ISHE})$  and represents the weight of the inverse spin Hall contribution. Adapted from W. Zhang *et al.*, 2014.

Table V lists the spin penetration depth for various antiferromagnetic materials separated into three different cases.

First, in ferromagnetic/nonmagnetic-metal/antiferromagnetic metallic trilayers the transport is purely electronic through the nonmagnetic metal. In the electronic transport regime, it was shown theoretically (see Sec. II.A) that while destructive interferences due to spin precession are reduced in staggered antiferromagnets, disorder dramatically enhances spin decoherence, thereby strongly reducing the magnitude of the current-induced staggered spin density. Moreover, some metallic antiferromagnetic compounds possess heavy metal constituents (IrMn, PtMn), resulting in large spin-orbit-driven spin relaxation. This explains why some experimental values for the electronic penetration length are finite. In Fig. 26, it can be seen that the electronic spin penetration depth is inversely proportional to the resistivity for most XMn materials, except for one PtMn data. This proportionality suggests that spin relaxation in these XMn alloys is mostly due to diffusion mechanisms (Bass and Pratt, 2007). The resulting product of resistivity and spin-diffusion length is a constant, with a value of around  $2.5 \text{ f}\Omega \text{ m}^2$ , as expected for metallic films. It should be noted that these data relate to polycrystalline films. In such a case, the different direction of the moments probably averages out any anisotropic spin-relaxation contribution due to the magnetic order. This type of signal averaging argument for polycrystals was discussed by W. Zhang *et al.* (2014, 2015) in the frame of the anisotropy of the spin Hall

effect: it will be discussed in more detail in Sec. III.C.2, which is devoted to spin Hall effect in antiferromagnets. Finally, for similar reasons, in Fig. 25(b) it can be observed that the amplitude of the spin sink efficiency ( $\alpha^P$ ) of polycrystalline IrMn layers is constant around the magnetic phase transition [at 300 K, thin IrMn films are paramagnetic below a film thickness of 2.7 nm and antiferromagnetic above (Frangou

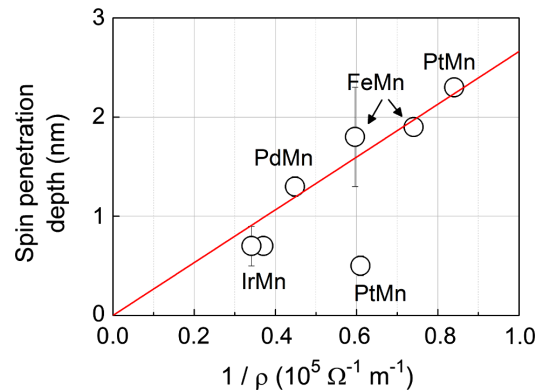


FIG. 26. Spin penetration depth is inversely proportional to bulk resistivity for some metallic antiferromagnets. Data are from Table V (metallic AF in a F/N/AF stack, electronic transport through N) and references therein. The straight line is a fit excluding the lowest data point for PtMn and constrained to pass through (0,0).

*et al.*, 2016)]. Once again, the spin pumping contribution of the static magnetic ordering of the spin sink at low temperature probably averages out.

Second, in exchange-biased (Sec. I.C.3) ferromagnetic/antiferromagnetic metallic bilayers transfer and propagation of spin-angular momentum also involves magnonic transport, i.e., spin waves produced by the oscillating ferromagnet feed directly into the antiferromagnet. In this case, both electronic and magnonic transport regimes may coexist, which makes it difficult to study. The data presented in Table V appear to suggest that overall spin currents propagate more easily when the metallic antiferromagnet is exchange biased to a ferromagnet. This is because spin currents carried by magnons decay more slowly than those carried by electrons. Note that the initial amplitude of the spin-angular momentum transfer contribution mediated by magnons through ferromagnetic/antiferromagnetic metallic interfaces is directly related to the interfacial exchange-coupling amplitude, as demonstrated by Tshitoyan *et al.* (2015). Using spin pumping and measuring the inverse spin Hall effect in NiFe/FeMn/W trilayers, Saglam *et al.* (2016) managed to disentangle electronic- and magnonic-transport-related penetration lengths in FeMn (see also Table V). They took advantage of the relatively large magnitude and opposite sign of spin Hall effects in W compared to FeMn to detect when magnonic transport takes over, i.e., when spin currents reach the W layer for FeMn thickness well above the electronic spin-diffusion length. Although transmission was purely electronic through the nonmagnetic metal in the previous case of ferromagnetic/nonmagnetic-metal/antiferromagnetic stacks, we believe that conversion of charge currents into magnons and vice versa cannot be excluded. These types of conversions are extensively discussed for the case of ferromagnets in the review on magnon spintronics by Chumak *et al.* (2015).

Third, in exchange-biased ferromagnetic/antiferromagnetic bilayers where the antiferromagnet is insulating, the transport is purely magnonic. Again, the data presented in Table V suggest or confirm that overall spin currents carried by magnons propagate more readily than their electronic counterparts, as previewed previously. In fact, a theoretical framework where the spin current in the antiferromagnet is carried by an evanescent spin-wave mode was established for the coherent coupled low-temperature dynamics (Takei *et al.*, 2015; Khymyn *et al.*, 2016). At finite temperatures, thermal magnons open an additional channel for spin transport (Rezende, Rodríguez-Suárez, and Azevedo, 2016b). In the antiferromagnet, the two magnon modes have different frequencies and hence different thermal populations, making magnonic spin transport possible. The precessing magnetization in the adjacent ferromagnet could pump oppositely polarized magnons differently into the antiferromagnet. These propagation mechanisms will be discussed further in Sec. IV, which is devoted to spin caloritronics in antiferromagnets. It should also be noted that magnons created by spin pumping or by the spin Seebeck effect have different frequencies and modes, which may contribute to data discrepancies.

As in ferromagnetic spintronics, heterostructure engineering with conductance matching is required to increase spin transport efficiency (Du *et al.*, 2014b; Ou *et al.*, 2016), which necessitates thorough investigations of interfacial qualities

(roughness, stacking faults, species intermixing, etc.) (Berkowitz and Takano, 1999). In addition, spin absorption mechanisms in antiferromagnetic materials are not currently entirely understood. Further investigation of how spins are transmitted through these materials is therefore required, including systematic quantification of the influence of heavy scatterer content or degree of crystallinity. The extent to which the static magnetic order affects transmission is also currently unclear. A better understanding of electronic and magnonic transport in metallic antiferromagnets is highly desirable, in particular, by finding efficient ways to distinguish between them, which would then potentially make it possible to control one over the other. Finite-size effects will have to be studied since the antiferromagnetic order is strongly influenced by size effects, in particular, those occurring at nanopillar edges due to grain size reduction (Baltz *et al.*, 2005) and reduced spin coordinations (Baltz, Gaudin *et al.*, 2010).

### C. Giant and tunnel magnetoresistance

The most popular and successful spintronics phenomena for data reading in practical applications are the giant magnetoresistance (GMR) and tunnel magnetoresistance (TMR). Their antiferromagnetic counterparts, antiferromagnetic GMR and TMR, were proposed to exist in so-called antiferromagnetic spin valves and magnetic tunnel junctions, respectively. The experimental demonstration of these antiferromagnetic phenomena, however, remains elusive.

#### 1. Giant magnetoresistance

In ferromagnets, (current-perpendicular-to-plane) giant magnetoresistance arises from the transmission of spin accumulation from one ferromagnetic electrode to the other. In antiferromagnets, although no such spin accumulation survives at the level of the magnetic unit cell, Núñez *et al.* (2006) demonstrated that the coherent buildup of a spin-dependent wave function in an antiferromagnetic spin valve results in a magnetoresistive signal (see also Sec. II.A.2 for the theoretical basis).

Several attempts have been made to demonstrate the antiferromagnetic giant magnetoresistance effect in antiferromagnetic spin valves where two antiferromagnets (AF) are separated by a nonmagnetic (N) spacer. According to the original predictions (Núñez *et al.*, 2006), the resistance of an antiferromagnetic spin valve AF/N/AF should depend on the relative orientation of magnetic order parameters in the two antiferromagnets. To control the relative orientation of the two antiferromagnets one usually employs the exchange-bias phenomenon by placing one or both antiferromagnets in contact with ferromagnets (F), e.g., in AF/N/AF/F or F/AF/N/AF/F structures. For a sufficiently thin antiferromagnet the reversal of the ferromagnet by a magnetic field should be accompanied by a reversal of the adjacent antiferromagnet thanks to the exchange coupling across the ferromagnet/antiferromagnet interface. Some experiments (Wang *et al.*, 2009; Wei, Sharma *et al.*, 2009) observed a small (0.1%–0.5%) change in resistance in such structures (AF = FeMn or IrMn, F = CoFe, N = Cu), which correlates with the reversal

of ferromagnets (antiferromagnets). However, a detailed study of these resistance variations in a large number of various structures (AF/N/AF, F/AF/N/AF, F/AF/N/AF/F, AF/F/N/AF, AF/F, and AF/N/F) and single (F, AF) layers showed no conclusive evidence of an antiferromagnetic giant magnetoresistance effect and could be associated with ferromagnetic contributions from either the ferromagnets or uncompensated magnetic moments in the antiferromagnets. The fact that giant magnetoresistance in antiferromagnetic spin valves has never been clearly experimentally observed may be related to the need for quantum coherence effects and minimal disorder.

## 2. Tunnel magnetoresistance

In ferromagnets, tunnel magnetoresistance arises from spin-dependent tunneling between ferromagnetic electrodes. Its magnitude is governed by the spin polarization of the density of states at the interface between the magnetic electrodes and the tunnel barrier (Tsymbal, Mryasov, and LeClair, 2003). In antiferromagnets, even though the interfacial density of states might not be spin polarized (e.g., in collinear compensated antiferromagnets), ballistic tunneling between antiferromagnets can also lead to a magnetoresistive signal (see also Sec. II.A.2 for the theoretical basis).

The first experimental search for such an antiferromagnetic tunnel magnetoresistance was performed by Y. Y. Wang *et al.* (2014a) in [Pt/Co]/IrMn/AlO<sub>x</sub>/IrMn/[Pt/Co] multilayers (see Fig. 27). The two IrMn antiferromagnetic layers are controlled via the exchange coupling by adjacent Pt/Co ferromagnetic multilayers with perpendicular magnetic anisotropy. For sufficiently thin antiferromagnetic layers ( $\leq 6$  nm) the resistance of such tunnel junctions was found to be slightly ( $<0.1\%$ ) different when saturated by positive or negative magnetic fields. The difference was attributed to different magnetic configurations of the two antiferromagnetic layers associated with partial rotations of the exchange spring propelled by the applied magnetic field. Investigations of Cr(001)-based tunnel junctions are also ongoing (e.g., studies on tunnel mediated coupling, electronic structure and magnetization of the surfaces and interfaces). More specifically, Leroy *et al.* (2013) demonstrated two two-dimensional localized states for the Cr surface that persist at the Cr/MgO interface: a  $\Delta_1$  and a  $\Delta_5$  state. The  $\Delta_1$  state is associated with

Cr surface magnetism. They found that the interface moment ( $0.02 \mu\text{B}/\text{Cr}$  atom) is tenfold smaller than expected from theoretical calculations and previous results (Leroy *et al.*, 2015). This is promising for the study of truly antiferromagnetic Cr-based junctions since the ferromagneticlike contribution should be minimal. The  $\Delta_5$  state mostly influences transport and coupling in Cr/MgO epitaxial systems. In Cr/MgO/Cr tunnel junctions, they demonstrated tunnel magnetic coupling between the antiferromagnetic Cr layers through the MgO insulator. They showed that this coupling can be amplified thanks to the presence of resonant states exhibiting the same  $\Delta_5$  symmetry at the interface (Leroy *et al.*, 2014).

## III. SPIN ORBITRONICS

The most encouraging developments in antiferromagnetic spintronics are currently building on spin-orbit interactions. Spin-orbit effects can be readily understood by considering the motion of an electron in a potential gradient  $\nabla V$  and how fields are transformed between inertial frames. The net electric field created by the potential gradient becomes a magnetic induction field in the electron's rest frame  $\mathbf{B}_{\text{SO}}$ . This momentum ( $k$ ) dependent magnetic field couples to the magnetic moment of the electron  $\boldsymbol{\mu}$  through a Zeeman term  $-\boldsymbol{\mu} \cdot \mathbf{B}_{\text{SO}}$ . In magnetic materials, this interaction interconnects the direction of electron flow and the magnetic order parameter, resulting in anisotropic magnetoresistance (McGuire and Potter, 1975) or anomalous Hall effect (Nagaosa *et al.*, 2010). Atomic spin-orbit interactions, where  $V$  is the potential with lattice periodicity, can be distinguished from effective spin-orbit interactions, which result from combining the atomic spin-orbit interaction with particular crystal or multilayer systems. In crystals or structures lacking inversion symmetry the  $k$ -dependent magnetic field becomes *odd* in momentum, resulting in Dresselhaus or Rashba fields (Manchon *et al.*, 2015). This provides a unique means to manipulate the order parameter in antiferromagnets. Here we review how spin-orbit effects occur in antiferromagnetic materials and how they can represent a promising alternative to conventional spin-transfer torque for the manipulation of the antiferromagnetic order. In addition, we will see how spin-orbit effects also make detection of the antiferromagnetic order possible.

### A. Anisotropic magnetoresistance

The anisotropic magnetoresistance effect was first found in 3d transition metals and alloys (Thomson, 1856). It is typically associated with the orientation of the material's magnetization with respect to the direction of electrical current flow. In these materials, the scattering of itinerant electrons (and hence the conductivity) depends on the magnetization direction because of the anisotropy of the electronic structure induced by spin-orbit coupling. The angular dependence of the effect is well described by cosine and sine trigonometric functions (De Ranieri *et al.*, 2008). These correspond to longitudinal and transversal anisotropic magnetoresistances, respectively (the latter is also known as the planar Hall effect). The phenomenon has been widely used as a detection element

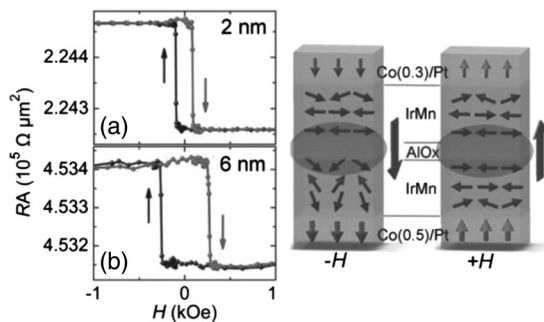


FIG. 27. (Left) Resistance times area product ( $RA$ ) vs out-of-plane magnetic field ( $H$ ) for IrMn-based tunnel junctions with different IrMn thickness. (Right) Scheme showing the moment arrangements in the junction for positive and negative applied magnetic fields. Adapted from Y. Y. Wang *et al.*, 2014a.

in early magnetic recording technology. However, its amplitude is typically limited to a few tens of percent.

Interestingly, anisotropic magnetoresistance is *even* in magnetization  $\sim(\mathbf{m} \cdot \mathbf{j}_C)^2$ , i.e., it is invariant upon magnetization reversal. Hence, such an effect also exists in antiferromagnets. Such type of (noncrystalline) anisotropic magnetoresistance was therefore demonstrated in collinear antiferromagnets such as FeRh (Marti *et al.*, 2014; Moriyama, Matsuzaki *et al.*, 2015), CuMnAs (Wadley *et al.*, 2016), MnTe (Kriegner *et al.*, 2016), and Mn<sub>2</sub>Au (H.-C. Wu *et al.*, 2016). The effect was also detected isothermally in IrMn (Galceran *et al.*, 2016). A typical example of noncrystalline anisotropic magnetoresistance at room temperature in an antiferromagnet (FeRh) is plotted in Fig. 28.

The noncrystalline component of the anisotropic magnetoresistance effect arises from the deviation of the current direction with respect to the magnetization. There exists another anisotropic magnetoresistance component that depends on the crystal symmetries: the crystalline anisotropic magnetoresistance. Recently this component of anisotropic magnetoresistance was found to be rather significant in oxides comprising a 5d transition metal (Fina *et al.*, 2014; C. Wang *et al.*, 2014, 2015). The experiment by Fina *et al.* (2014) reported on experimental observation of the crystalline anisotropic magnetoresistance in a 6-nm-thick film of antiferromagnetic semiconductor Sr<sub>2</sub>IrO<sub>4</sub>. The antiferromagnetic film in this experiment was exchange coupled to a ferromagnet

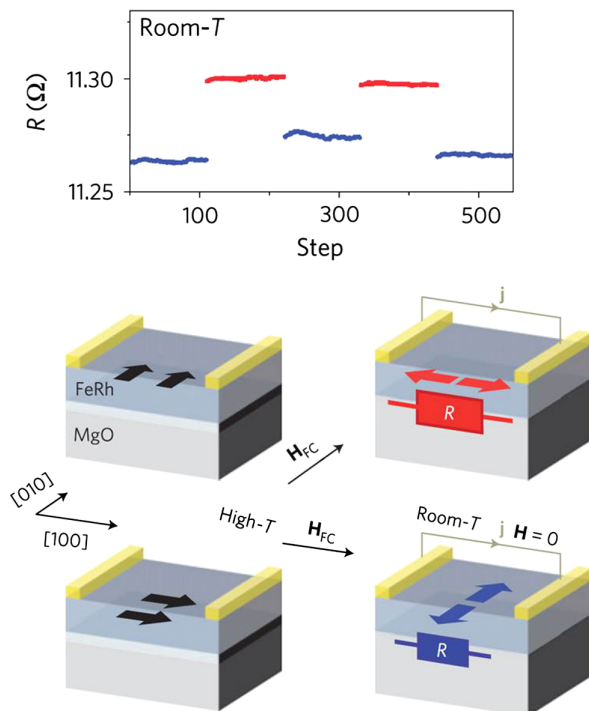


FIG. 28. Anisotropic magnetoresistance effect measured at room temperature in the antiferromagnetic FeRh alloy. The antiferromagnetic order is alternatively set toward two orthogonal directions [100] or [010] by raising the temperature above the metamagnetic phase transition, saturating the ferromagnetic order with a magnetic field (either along the [010] or [100] crystal axis), and field cooling through the phase transition. From Marti *et al.*, 2014.

[La<sub>0.67</sub>Sr<sub>0.33</sub>MnO<sub>3</sub> (LSMO)] that was used to reorient the antiferromagnetic order parameter by applying an external magnetic field. Here the field was assumed to rotate the ferromagnet which in turn reorients the antiferromagnet via the exchange spring effect (see Sec. I.C.3). Resistivity measurements of this exchange-biased ferromagnetic/antiferromagnetic bilayer placed in an in-plane rotating magnetic field clearly showed correlations between the bilayer resistance and the angle between magnetization and crystal axes. Since for the in-plane field rotations the angle between the electrical current (flows along the out-of-plane *c* axis) and in-plane magnetic moments remains constant, the observed  $\sim 1\%$  effect can be associated with the crystalline component of anisotropic magnetoresistance. The experiments by C. Wang *et al.* (2014) demonstrated a much larger magnetoresistive effect in a single crystal of Sr<sub>2</sub>IrO<sub>4</sub> antiferromagnet without any ferromagnets in proximity. However, in this particular case, the results were observed at weak external magnetic fields. Part of the magnetoresistive effect was thus probably due to uncompensated moments rather than being associated with the antiferromagnetic order.

Point-contact measurements (see Fig. 29) revealed negative magnetoresistances (up to 28%) for modest magnetic fields (250 mT) applied within the IrO<sub>2</sub> *a-b* plane and electric currents flowing perpendicular to the plane. Here the point-contact technique was used as a local probe of magnetotransport properties on the nanoscale, as opposed to standard bulk measurements, and demonstrated the scalability of the effect for future applications. As the currents were flowing perpendicular to the in-plane magnetic moments, the observed magnetoresistance was attributed to the crystalline component of anisotropic magnetoresistance. The angular dependence of magnetoresistance showed a crossover from fourfold to twofold symmetry in response to an increasing magnetic field with angular variations in resistance from 1% to 14%. This field-induced transition can be associated with the effects of applied field on the canting of antiferromagnetic-coupled moments in Sr<sub>2</sub>IrO<sub>4</sub>. It should be noted that the Néel temperature in bulk Sr<sub>2</sub>IrO<sub>4</sub> (240 K) is well below room temperature and it is even smaller in thin films (100 K); see Sec. I.B and Table III. The latter makes practical applications of Sr<sub>2</sub>IrO<sub>4</sub> questionable and calls for materials science efforts to find an appropriate antiferromagnet to demonstrate room-temperature crystalline anisotropic magnetoresistance.

We finally point out here that anisotropic magnetoresistance was also demonstrated in another class of interesting materials: antiferromagnetic Heusler alloys. Relying on exchange-bias coupling (Sec. I.C.3) between a Fe<sub>2</sub>CrSi ferromagnet and a Ru<sub>2</sub>MnGe antiferromagnetic Heusler alloy, Hajiri *et al.* (2017) demonstrated the angular dependence of the in-current resistance on the direction of magnetic moments in plane geometry. The result was some combination of anisotropic magnetoresistance in both layers, since the ferromagnetic layer alone shows only a fraction of the magnetoresistance of the whole system.

## B. Tunnel anisotropic magnetoresistance

Similar to Ohmic anisotropic magnetoresistance, tunnel anisotropic magnetoresistance possesses noncrystalline and

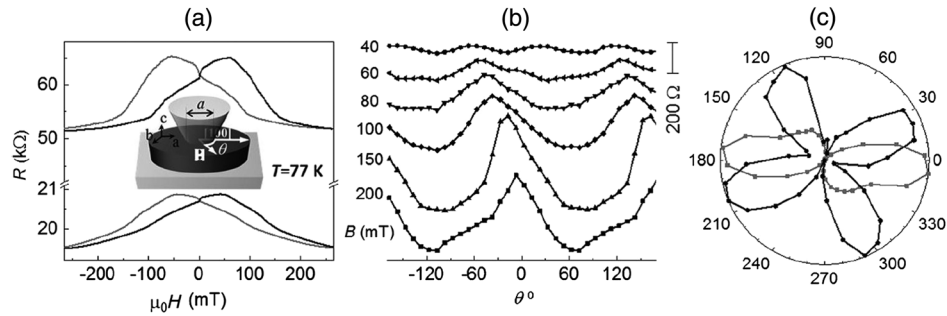


FIG. 29. (a) Resistance vs in-plane magnetic field measured at 77 K for two point contacts (3 and 1  $\mu\text{m}$ ) between a Cu tip and a  $\text{Sr}_2\text{IrO}_4$  crystal. The inset shows a schematic of the experiment. (b) Angular dependence of a point-contact resistance for different magnetic fields. (c) Polar plots of the normalized anisotropic magnetoresistance at 40 mT (black) and 270 mT (gray). From C. Wang *et al.*, 2014.

crystalline components. Tunnel anisotropic magnetoresistance is driven by the relative orientation of magnetic moments and the axes of current direction and crystalline anisotropy. The difference compared to Ohmic anisotropic magnetoresistance is that the noncrystalline tunnel anisotropic magnetoresistance component is difficult to separate from the crystalline component since in multilayers the crystal is different in the in-plane and out-of-plane directions. Basically, in a ferromagnet/tunnel-barrier/nonmagnet trilayer (F/B/N), the amount of current tunneling perpendicularly through the junction is proportional to the nonmagnet and ferromagnet densities of states at the Fermi level and the tunneling matrix elements. These tunneling matrix elements and ferromagnet density of states depend on the ferromagnet's orientation with respect to the crystalline anisotropy axes. Hence, by varying the ferromagnetic orientation (e.g., by applying an external magnetic field  $H$ ), the resistance ( $R$ ) of the trilayer can be changed. Some of the explanations for tunnel anisotropic magnetoresistance are based on Rashba- or Rashba and Dresselhaus-induced spin-orbit coupling (Shick *et al.*, 2006; Matos-Abiadue and Fabian, 2009). The effect was first experimentally shown to exist in (Ga,Mn)As-based tunnel junctions (Gould *et al.*, 2004) and has been widely studied since then for various ferromagnetic-based tunnel junctions. For ferromagnetic materials, only small tunnel anisotropic magnetoresistance signals have been reported at low temperature. This lack of signal is related to the fact that spin-orbit coupling in ferromagnetic transition metals which have the potential for room-temperature tunnel anisotropic magnetoresistance is too weak. Thus, the tunnel anisotropic magnetoresistance reaches a few percentage points at 4 K and can rise to 10% when the spin-orbit interaction is boosted by additional heavy elements, e.g., in [Co/Pt] multilayers (Park *et al.*, 2008).

Interestingly, Shick *et al.* (2010) predicted large tunnel anisotropic magnetoresistance signals for alloys such as IrMn and  $\text{Mn}_2\text{Au}$  containing a heavy noble metal (Ir, Au) and a transition metal (Mn) (see Fig. 30). In this case, the  $5d$  shell of the noble metal offers large spin-orbit coupling and the  $3d$  shell of the transition metal adds complementary large spontaneous moments. As indicated by Park *et al.* (2011): “as Mn carries the largest moment among transition metals and most of the bimetallic alloys containing Mn order antiferromagnetically, the goals of strong magnetic anisotropy phenomena and of antiferromagnetic spintronics seem to

merge naturally,” although the phenomenon is mainly driven by spin-orbit interactions and the role played by the magnetic order remains to be understood.

The predicted tunnel anisotropic magnetoresistance structures were experimentally confirmed for  $\text{Ir}_{20}\text{Mn}_{80}$  using in-plane anisotropy (160% at 4 K) (Park *et al.*, 2011; Martí *et al.*, 2012). Full hysteretic  $R$  vs  $H$  loops with bistable remanent states were obtained by forcing the antiferromagnetic configuration thanks to a neighboring exchange-biased ferromagnetic layer (see Sec. I.C.3 for antiferromagnetic order manipulation by exchange bias). In this case, the antiferromagnetic configuration is driven by exchange bias on one side and the tunnel anisotropic magnetoresistance is detected for the other side. What matters is that the antiferromagnetic moments are dragged through the whole system when reversing the ferromagnet so as to achieve the most extensive change in the angle of the antiferromagnetic moments on the tunnel-barrier side, and hence the largest possible tunnel anisotropic magnetoresistance signal. How easily and how deep the antiferromagnetic moments are dragged by the ferromagnet depends on external stimuli such as temperature and is also partly system dependent, since it depends on the

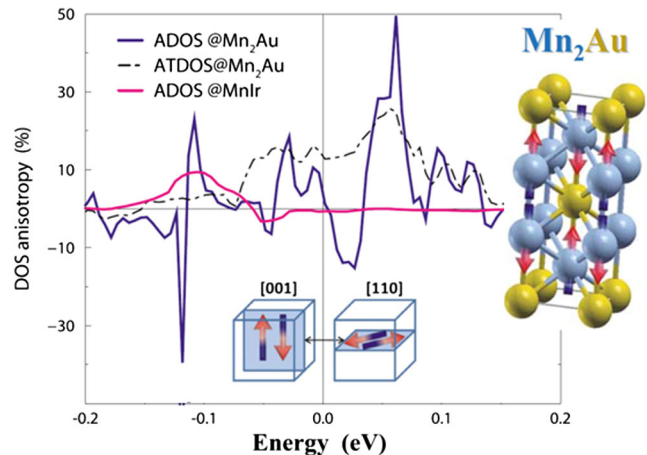


FIG. 30. Anisotropy of the densities of state between the [001] and [110] axes for  $\text{Mn}_2\text{Au}$  and MnIr films. The inset shows a  $\text{MoSi}_2$ -type body-centered-tetragonal structure and the spin arrangement in  $\text{Mn}_2\text{Au}$ . The Fermi level is at 0 eV. From Shick *et al.*, 2010.



amplitude of exchange energy between the ferromagnet and the antiferromagnet, and antiferromagnetic exchange stiffness. For NiFe/IrMn/MgO/Pt tunnel junctions, Reichlová *et al.* (2016) observed tunnel anisotropic magnetoresistance at room temperature and determined the optimal NiFe/IrMn thickness ratio to be 10/4.

Y. Y. Wang *et al.* (2012, 2014b) exploited the thermal stability of antiferromagnet-based systems with out-of-plane anisotropy to further demonstrate room-temperature (antiferromagnetic) tunnel anisotropic magnetoresistance ( $\sim 0.2\%$ ) and hysteretic behavior for [Pt/Co]/IrMn, FeMn/B/N stacks (see Fig. 31).

Given the previous results, tunnel anisotropic magnetoresistance is a promising means to analyze antiferromagnetic configurations, despite the small signals it delivers so far and even though room-temperature signals can be measured only when a ferromagnetic layer with perpendicular anisotropy is present to pull the antiferromagnetic spins out of plane. This requirement has so far prevented the development of a (ferro) magnet-free device readable by means of tunnel anisotropic magnetoresistance. Another alternative would be to use antiferromagnetic alloys containing a  $5d$  shell element but with a heavier noble metal than Ir and a larger ratio of noble metal to magnetic moment-carrying transition metal. These conditions should make Pt<sub>50</sub>Mn<sub>50</sub> or mixed antiferromagnets (Akmaldinov *et al.*, 2014) terminated with a Pt<sub>50</sub>Mn<sub>50</sub> interface good candidates. Antiferromagnetic semiconductors could also be used to benefit from carrier-mediated magnetism. Promising recent studies described additional examples of this type of alternative room-temperature antiferromagnetic material with potential for large tunnel anisotropic magnetoresistance. These included metallic Mn<sub>2</sub>Au alloys (Wu *et al.*,

2012; Barthem *et al.*, 2013) and semimetallic CuMnAs (Wadley *et al.*, 2013); see also Sec. III.D.2.

### C. Anomalous and spin Hall effects

#### 1. Anomalous Hall effect in noncollinear antiferromagnets

Traditionally, the charge Hall effect exists in three main variants: (i) in the presence of an external magnetic field upon applying a Lorentz force [ordinary (normal) Hall effect  $\rho_{yx}^N$ ], (ii) in magnetic materials with spin-orbit coupling (anomalous Hall effect  $\rho_{yx}^A$ ), and (iii) in chiral magnetic textures (topological Hall effect  $\rho_{yx}^T$ ) [for a review, see Nagaosa *et al.* (2010)]. Charge Hall effects produce a transverse resistivity of the following form:

$$\rho_{yx} = \rho_{yx}^N + \rho_{yx}^A + \rho_{yx}^T = R_0 B + R_S \mu_0 M + \rho_{yx}^T, \quad (34)$$

where  $R_0$  and  $R_S = S_A \rho_{xx}^2 / \mu_0$  correspond to the (field-independent) normal and anomalous Hall effect coefficients, respectively,  $B$  is the magnetic induction, and  $M$  is the magnetization (Kanazawa *et al.*, 2011). The three variants indicate that the charge Hall effect is produced by a combination of time-reversal symmetry breaking and some sort of “effective Lorentz force.” The former is achieved by applying a nonvanishing magnetic field and the latter can be obtained through nonzero Berry curvature of the band structure, which provides anomalous velocity. It is notable that the anomalous Hall effect is odd in magnetization (while anisotropic magnetoresistance, discussed in Sec. III.A, is even). Since antiferromagnetic materials lack overall magnetization, it was long (incorrectly) believed that they show no charge Hall effect.

Although antiferromagnets do not possess time-reversal symmetry, they are invariant when time-reversal symmetry is combined with a crystal symmetry operation [such as spatial translation by the vector connecting the two sublattices in the case of a bipartite antiferromagnet, or mirror symmetry in the case of the two-dimensional kagome lattice studied by Chen, Niu, and MacDonald (2014)]. If crystal symmetry is broken, a nonvanishing Berry curvature is produced leading to the emergence of a finite anomalous Hall effect. This property is absent in collinear antiferromagnets but has been predicted for some noncollinear antiferromagnetic compounds: distorted  $\gamma$ -Fe<sub>x</sub>Mn<sub>1-x</sub>, and NiS<sub>2</sub> (Shindou and Nagaosa, 2001), IrMn<sub>3</sub> (Chen, Niu, and MacDonald, 2014), Mn<sub>3</sub>Ge, and Mn<sub>3</sub>Sn (Kübler and Felser, 2014). Figure 32 presents the anomalous Hall conductivity calculated for IrMn<sub>3</sub>. This conductivity was induced by tilting the magnetic moments out of the (111) planes in the absence (red triangles) and presence (black squares) of spin-orbit coupling (Chen, Niu, and MacDonald, 2014). From the figure, it is clear that without spin-orbit coupling, the anomalous Hall effect is present only when the moments are tilted out of plane. It is therefore similar to the topological Hall effect observed in ferromagnetic textures such as vortices and skyrmions (Neubauer *et al.*, 2009). With the spin-orbit coupling turned on, a large anomalous Hall conductivity is obtained, even when the antiferromagnet is fully compensated (zero angle).

This large anomalous Hall effect was recently experimentally confirmed in certain noncollinear antiferromagnets such

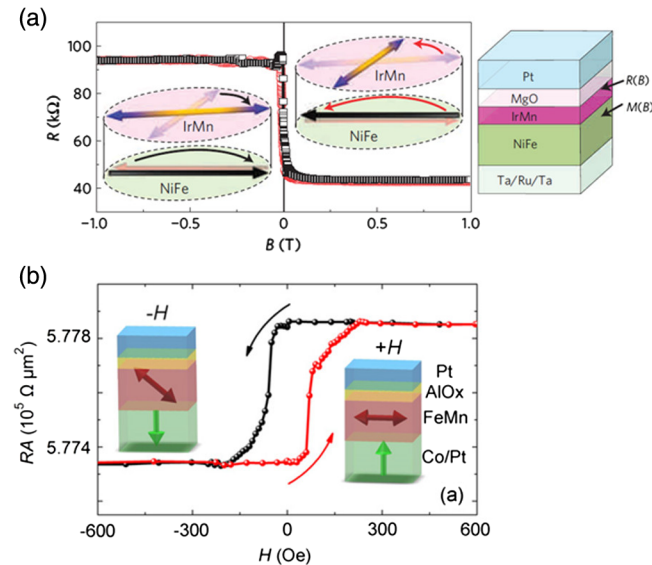


FIG. 31. (a) Hysteretic resistance ( $R$ ) vs magnetic induction ( $B$ ) showing extensive antiferromagnetic tunnel anisotropic magnetoresistance at 4 K for IrMn. From Park *et al.*, 2011. (b) Hysteretic resistance area product ( $RA$ ) vs magnetic field ( $H$ ) showing room-temperature antiferromagnetic tunnel anisotropic magnetoresistance and binary remanence for FeMn, facilitated by the out-of-plane anisotropy of the ferromagnetic layer. From Y. Y. Wang *et al.*, 2014b.

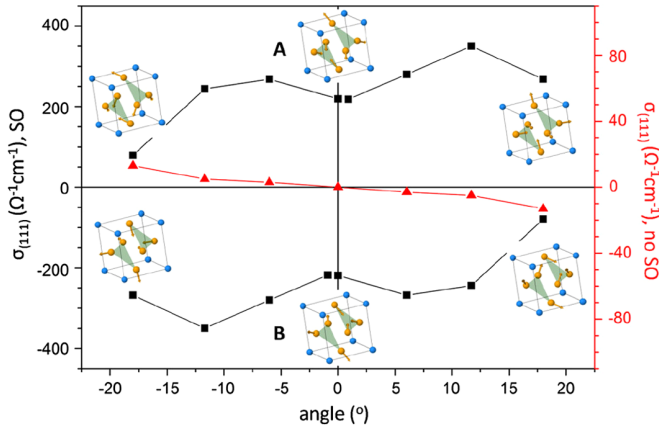


FIG. 32. Anomalous Hall effect in IrMn<sub>3</sub> calculated from first principles in the absence (red triangles) and presence (black squares) of spin-orbit coupling. From Chen, Niu, and MacDonald, 2014.

as Mn<sub>5</sub>Si<sub>3</sub> (Sürgers *et al.*, 2014, 2016) (see Fig. 33), Mn<sub>3</sub>Sn (Nakatsuji, Kiyohara, and Higo, 2015), Mn<sub>3</sub>Ge (Nayak *et al.*, 2016), and GdPtBi (Suzuki *et al.*, 2016) single crystals. It should be noted that the anomalous Hall effect in noncollinear antiferromagnets combines with longitudinal spin currents (i.e., the charge current is spin polarized). This was recently predicted by Železný, Zhang *et al.* (2017) and it will be discussed with respect to the spin Hall effect in the next section in greater detail.

## 2. Spin Hall effect

The spin Hall effect derives from coupling of the charge and spin currents due to spin-orbit interaction (Dyakonov, 2010; Hoffmann, 2013; Sinova *et al.*, 2015). Through this interaction, a charge current ( $\mathbf{j}_C$ ) induces a pure spin current ( $\mathbf{j}_S$ ) orthogonal to the electric current. This process depends on the spin ( $\mathbf{s}$ ) and the direction of the spin current follows  $\mathbf{s} \times \mathbf{j}_C$ . The inverse process or inverse spin Hall effect, whereby the spin current induces an orthogonal charge current, is also present. The spin Hall effect was first experimentally confirmed in semiconducting GaAs (Kato *et al.*, 2004;

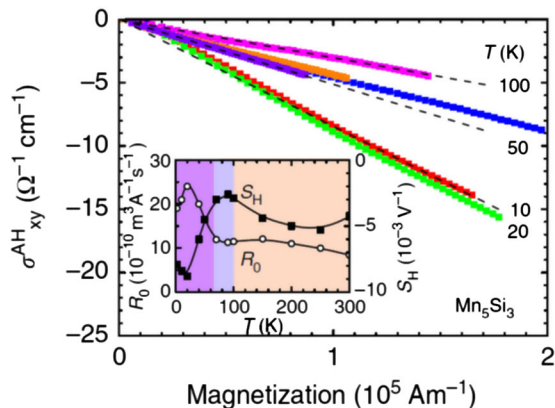


FIG. 33. Anomalous Hall effect measured in Mn<sub>5</sub>Si<sub>3</sub> layers. Adapted from Sürgers *et al.*, 2014.

Wunderlich *et al.*, 2005); it was subsequently detected in metallic materials with large spin-orbit interaction, such as platinum (Saitoh *et al.*, 2006; Valenzuela and Tinkham, 2006). The spin Hall effect can be induced by two classes of physical mechanisms: extrinsic and intrinsic. Extrinsic mechanisms, such as skew and side jump scattering, are associated with charge-to-spin conversion during scattering events. In contrast, the intrinsic mechanism is not affected by (weak) scattering and depends only on the band structure of the material (Murakami, Nagaosa, and Zhang, 2003). The Berry curvature resulting from the geometric phase in the momentum space creates a local magnetic field that exerts a spin-dependent Lorentz force on the flowing spins resulting in spin Hall effect (Sinova *et al.*, 2015). Thus, the spin Hall effect is not limited to nonmagnetic materials, and indeed a sizable spin Hall effect was recently experimentally observed in ferromagnetic (Miao *et al.*, 2013; Du *et al.*, 2014a) and antiferromagnetic materials (Table VI).

The spin Hall effect is generally quantified in terms of the spin Hall angle  $\theta_{SH}$ , which represents the conversion ratio between the spin-current density and the charge current density  $\theta_{SH} = j_s/j_c$  (Hoffmann, 2013). Notably, this definition assumes small  $\theta_{SH}$  to allow for the Taylor approximation of the tangent function near zero. Various experimental measurement techniques have been employed to determine the value of  $\theta_{SH}$ , including spin torque ferromagnetic resonance (Liu *et al.*, 2011), spin pumping experiments exploiting the inverse spin Hall effect (Saitoh *et al.*, 2006) [see also Figs. 25(a) and 25(b)], magnetization switching (Suzuki *et al.*, 2011), domain-wall dynamics (Emori *et al.*, 2013), second harmonic measurement (Pi *et al.*, 2010), and dc Hall measurement (Kawaguchi *et al.*, 2013).

Pioneering experimental measures of the spin Hall effect in antiferromagnets were reported by Mendes *et al.* (2014) in Ir<sub>20</sub>Mn<sub>80</sub> layers; see Fig. 34. They showed that the Hall angle of Ir<sub>20</sub>Mn<sub>80</sub> is comparable to that of platinum:  $\theta_{SH, IrMn} \sim 0.8\theta_{SH, Pt}$ . Thorough investigations based on similar measurement techniques were subsequently reported for a number of other materials (see Table VI).

In particular, W. Zhang *et al.* (2014, 2015) confirmed that 5*d* metal alloys, such as IrMn and PtMn, have a larger spin Hall angle than 4*d* metal alloys, such as PdMn, and 3*d* metal alloys, such as FeMn. These results highlighted the important role that spin-orbit coupling of the heavy elements plays in determining the properties of their simple alloy (Seemann *et al.*, 2010; Chen, Niu, and MacDonald, 2014). Further studies (Du *et al.*, 2014a; H. L. Wang *et al.*, 2014) demonstrated the impact of *d*-orbital filling and highlighted the additive nature of effects due to atomic number and orbital filling as calculated by Tanaka *et al.* (2008). Antiferromagnetic alloys also seem to obey this rule (see Table VI and corresponding Fig. 35). Thus, within the same *d* shell, the orbital filling seems to govern the spin Hall effect. In contrast, for different materials with the same (valence) electron number, the influence of the atomic number seems to prevail. For example, PtMn and PdMn share the same electron number but show very different Hall angles since PtMn is a 5*d* alloy whereas PdMn is 4*d*. In this case, the ratio of Hall angles obeys the  $Z^4$  dependence:  $\theta_{SH, PtMn}/\theta_{SH, PdMn} \sim (Z_{PtMn}/Z_{PdMn})^4 \sim 4$ .

TABLE VI. Spin Hall angles determined for various antiferromagnets. When not specified, the investigation temperature was 300 K, and the layers were polycrystalline. SP and SP ( $\Delta H$ ) refer to ferromagnetic resonance spin pumping excitation—detection based on the inverse spin Hall effect, or ferromagnetic resonance linewidth [when ( $\Delta H$ ) is specified], ST-FMR and ST-FMR (HR) refer to spin torque ferromagnetic resonance excitation induced by spin Hall effect subsequent to an ac current flow—detection based on anisotropic magnetoresistance, or second harmonic response detection of the anomalous Hall effect and/or anisotropic magnetoresistance [when (HR) is specified], MOD refer to spin Hall effect excitations induced by a dc current flow—detection of the modulation of the ferromagnetic resonance damping, ST-FMS refer to spin torque ferromagnetic switching induced by spin Hall effect subsequent to a dc current flow—anomalous Hall effect detection, SSE refer to spin Seebeck excitation induced by a thermal gradient—inverse spin Hall effect detection, and oop stand for the out-of-plane magnetization. DL and FL refer to dampinglike and fieldlike torque components, respectively.

AF material	Effective spin Hall angle (%)	Technique	Stack	Reference
Pt <sub>50</sub> Mn <sub>50</sub>	6 ± 1	SP	NiFe/Cu/PtMn	W. Zhang <i>et al.</i> (2014)
Pt <sub>50</sub> Mn <sub>50</sub>	6.4–8.1	ST-FMR	NiFe/Cu/PtMn	Zhang <i>et al.</i> (2015)
Pt <sub>50</sub> Mn <sub>50</sub>	8 (DL) 2 (FL)	MOD	NiFe/Cu/PtMn	Zhang <i>et al.</i> (2015)
Pt <sub>50</sub> Mn <sub>50</sub> ( <i>c</i> axis)	4.8–5.2	ST-FMR	NiFe/Cu/PtMn	Zhang <i>et al.</i> (2015)
Pt <sub>50</sub> Mn <sub>50</sub> ( <i>a</i> axis)	8.6–8.9	ST-FMR	NiFe/Cu/PtMn	Zhang <i>et al.</i> (2015)
Pt <sub>50</sub> Mn <sub>50</sub>	10	ST-FMS	[Co/Ni]/PtMn (oop)	Fukami <i>et al.</i> (2016)
Pt <sub>50</sub> Mn <sub>50</sub>	16–19 (DL) <sup>a</sup> 4–0 (FL)	ST-FMR (HR)	Co/PtMn And reversed	Ou <i>et al.</i> (2016)
Pt <sub>50</sub> Mn <sub>50</sub>	9.6–17.4 (DL) <sup>a</sup> 4.3–3.6 (FL)	ST-FMR (HR)	FeCoB/PtMn And reversed	Ou <i>et al.</i> (2016)
Pt <sub>50</sub> Mn <sub>50</sub>	11 (DL) <sup>a</sup> 4 (FL)	ST-FMR (HR)	FeCoB/PtMn (oop)	Ou <i>et al.</i> (2016)
Pt <sub>50</sub> Mn <sub>50</sub>	24 (DL) <sup>a</sup>	ST-FMR (HR)	FeCoB/Hf/PtMn (oop)	Ou <i>et al.</i> (2016)
Ir <sub>50</sub> Mn <sub>50</sub>	2.2 ± 0.5	SP	NiFe/Cu/IrMn	W. Zhang <i>et al.</i> (2014)
Ir <sub>50</sub> Mn <sub>50</sub>	5.3–5.7	ST-FMR	NiFe/Cu/PtMn	Zhang <i>et al.</i> (2015)
Ir <sub>50</sub> Mn <sub>50</sub> (~poly, tentatively <i>a</i> axis)	2.3	ST-FMR	NiFe/Cu/PtMn	Zhang <i>et al.</i> (2015)
Ir <sub>50</sub> Mn <sub>50</sub> ( <i>c</i> axis)	5 ± 0.5	ST-FMR	NiFe/Cu/PtMn	Zhang <i>et al.</i> (2015)
$\gamma$ – Ir <sub>20</sub> Mn <sub>80</sub>	0.8–6.4; 0.8 × Pt <sup>b</sup>	SP and SSE	YIG/IrMn	Mendes <i>et al.</i> (2014) and Rojas-Sánchez <i>et al.</i> (2014)
Ir <sub>20</sub> Mn <sub>80</sub>	2.9 ± 1.5 (DL)	ST-FMR (HR)	CoFeB/IrMn	Reichlová <i>et al.</i> (2015)
Ir <sub>20</sub> Mn <sub>80</sub>	4.3 ± 0.1 (DL)	MOD	NiFe/Cu/IrMn	Tshitoyan <i>et al.</i> (2015)
Ir <sub>20</sub> Mn <sub>80</sub>	5.6 ± 0.9	ST-FMR	NiFe/Cu/IrMn	Tshitoyan <i>et al.</i> (2015)
Ir <sub>22</sub> Mn <sub>78</sub>	5.7 ± 0.2 (DL)	ST-FMR (HR)	CoFeB/IrMn	D. Wu <i>et al.</i> (2016)
Ir <sub>20</sub> Mn <sub>80</sub>	> 10.9 <sup>c</sup>	ST-FMR	NiFe/IrMn	Tshitoyan <i>et al.</i> (2015)
Ir <sub>20</sub> Mn <sub>80</sub>	13.5 (DL)	MOD	NiFe/IrMn	Tshitoyan <i>et al.</i> (2015)
Ir <sub>25</sub> Mn <sub>75</sub>	2	ST-FMR	NiFe/IrMn	Soh <i>et al.</i> (2015)
Ir <sub>25</sub> Mn <sub>75</sub>	~9	ST-FMR	NiFe/IrMn	Zhang <i>et al.</i> (2016)
Ir <sub>25</sub> Mn <sub>75</sub> (111)	~11	ST-FMR	NiFe/IrMn	Zhang <i>et al.</i> (2016)
Ir <sub>25</sub> Mn <sub>75</sub> (100)	~20	ST-FMR	NiFe/IrMn	Zhang <i>et al.</i> (2016)
Pd <sub>50</sub> Mn <sub>50</sub>	1.5 ± 0.5	SP	NiFe/Cu/PdMn	W. Zhang <i>et al.</i> (2014)
Pd <sub>50</sub> Mn <sub>50</sub>	2.8–4.9	ST-FMR	NiFe/Cu/PtMn	Zhang <i>et al.</i> (2015)
Pd <sub>50</sub> Mn <sub>50</sub> ( <i>c</i> axis)	3.2 ± 0.6	ST-FMR	NiFe/Cu/PtMn	Zhang <i>et al.</i> (2015)
Pd <sub>50</sub> Mn <sub>50</sub> ( <i>a</i> axis)	3.9 ± 0.5	ST-FMR	NiFe/Cu/PtMn	Zhang <i>et al.</i> (2015)
Cr	–5.1 ± 0.5	SP	YIG/Cr	Du <i>et al.</i> (2014a)
Cr (30–345 K)	–9 (–1.38 × 20 × Cu)	SSE	YIG/Cr	Qu, Huang, and Chien (2015)
Mn	–0.19 ± 0.01	SP	YIG/Mn	Du <i>et al.</i> (2014a)
Fe <sub>50</sub> Mn <sub>50</sub>	0.8 ± 0.2	SP	NiFe/Cu/FeMn	W. Zhang <i>et al.</i> (2014)
Fe <sub>50</sub> Mn <sub>50</sub>	2.2–2.8	ST-FMR	NiFe/Cu/FeMn	Zhang <i>et al.</i> (2015)
$\gamma$ -Fe <sub>50</sub> Mn <sub>50</sub>	–(7.4 ± 0.8) × 10 <sup>–3</sup>	SP	YIG/FeMn	Du <i>et al.</i> (2014a)

<sup>a</sup>Values of the spin torque efficiency [effective interface transparency ( $<1$ ) × spin Hall angle].

<sup>b</sup>The values of the effective spin Hall angle for Pt were taken from Rojas-Sánchez *et al.* (2014) and typically range between values close to 1% and 10%.

<sup>c</sup>Linear increase with the IrMn thickness.

These pioneering theoretical and experimental works highlighted the need for further investigation (Sklenar *et al.*, 2016): first to quantify spin-orbit interactions prior to testing their efficiency as will be discussed later, second to experimentally determine how the magnetic order influences the spin Hall effect, and above all to maximize the spin Hall effect in antiferromagnets. Complementary studies on the role played by heavy elements in determining the properties of spin-orbit

interaction in antiferromagnetic alloys could involve doping the antiferromagnet with impurities up to the limits of solubility so as to investigate the resultant change in spin Hall angle and the dominant underlying mechanism. How much the static magnetic order, and related noncollinear spin texture, influence the amplitude of the spin Hall effect motivated several studies. In Fig. 25(c) it can be observed that, similar to spin pumping [Fig. 25(b)], the amplitude of the

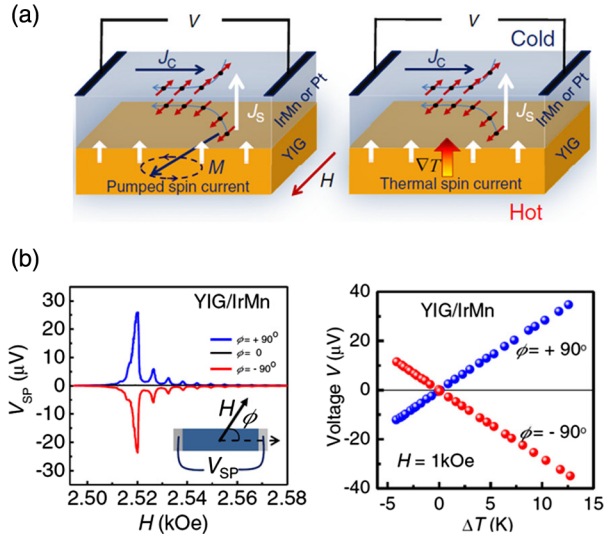


FIG. 34. (a) Sketch showing the spin-current density generated by spin pumping (left) and spin Seebeck (right) effects and the resulting charge current density converted by inverse spin Hall effect. (b) Voltages measured for these spin currents across the IrMn layer while varying the magnetic field ( $H$ ) or temperature difference across the stack ( $\Delta T$ ). From Mendes *et al.*, 2014.

inverse spin Hall effect in polycrystalline IrMn layers is constant around the magnetic phase transition [i.e., around  $t_{\text{IrMn}} = 2.7$  nm (Frangou *et al.*, 2016)]. The inverse spin Hall effect in such noncollinear polycrystalline IrMn layers ( $3Q$  spin structure in bulk, Table I) is probably mainly sensitive to the nature of the elements making up the alloy, and to a lesser extent to the magnetic order where the different directions of the moments average out the spin Hall signal, as computed by W. Zhang *et al.* (2014). This effect will be discussed in detail next. The inverse spin Hall effect in polycrystalline Cr with a preferred (110) texture was also reported to be independent of the ordering of the metal (Qu, Huang, and Chien, 2015). This finding was probably due to the combination of unusual spin density wave antiferromagnetic ordering and texture

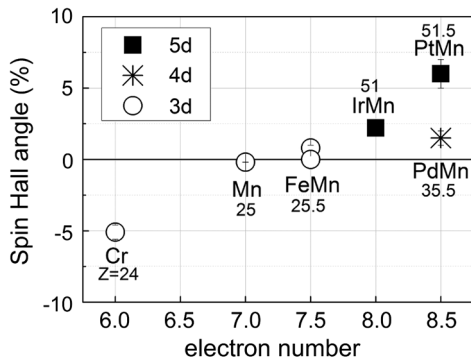


FIG. 35. Spin Hall angle vs electron number. The data are from Table VI and references therein (only data measured with the SP technique are plotted so as to avoid possible misleading technique-related dispersions of the data point, see text). For memory, the outer electronic shell filling patterns are as follows: Cr ( $3d^5 4s^1$ ), Mn ( $3d^5 4s^2$ ), Fe ( $3d^6 4s^2$ ), Ir ( $5d^9 6s^0$ ), Pt ( $5d^9 6s^1$ ), and Pd ( $4d^{10} 5s^0$ ).

averaging out the spin Hall signal, although this effect remains to be accurately theoretically demonstrated.

First-principles calculations based on density functional theory actually show anisotropy of the spin Hall effect, meaning that spin Hall conductivity is sensitive to the direction of staggered magnetization with respect to the crystallographic axes (W. Zhang *et al.*, 2014). By averaging the spin Hall conductivities computed for staggered magnetization oriented along different axes W. Zhang *et al.* (2014) could qualitatively reproduce their experimental findings on polycrystalline PtMn, IrMn, and FeMn films. Zhang *et al.* (2015) further showed that epitaxial CuAu-I type antiferromagnets (PtMn, PdMn, IrMn, and FeMn, see also Table I) could effectively be used to study how the magnitude of the spin Hall effect is influenced by the magnetic order. More specifically, CuAu-I type PtMn, PdMn, IrMn, and FeMn antiferromagnets have a collinear staggered spin structure (see Table I), the orientation of which depends on the crystal growth. The anisotropy of the spin Hall effect arises from the anisotropy of both chemical and magnetic structures. Zhang *et al.* (2015) (see Table VI) experimentally demonstrated the anisotropy of the spin Hall effect in antiferromagnets and corroborated data by first-principles calculations using density functional theory.

We emphasize that estimation of the actual spin Hall angle value in antiferromagnets faces the same problems already encountered for more common materials, such as Pt. Variations in the spin Hall angle were found with various measurement methods and material combinations. In some cases, these variations were ascribed to spin-memory loss at interfaces (Rojas-Sánchez *et al.*, 2014). With some techniques (see Table VI), a charge-to-spin-current conversion occurs in the antiferromagnet (e.g., with the ST-FMR, ST-FMS, and MOD techniques). In these cases, there are alternatives to the spin Hall effect as sources of spin current (e.g., inverse spin galvanic effects). These alternative sources may explain why the effective Hall angle deduced by these techniques overestimates the actual Hall angle compared to other techniques such as SP and SSE (see Table VI). Note also that ST-FMR data can be extracted from either ratio or amplitude analysis of symmetric and antisymmetric contributions to an FMR line shape. These alternatives may also contribute to the slight data dispersion observed, although similar data have been obtained by the two methods (Zhang *et al.*, 2015). While the values for ST-FMR and MOD were larger than those for SP, the results presented by Zhang *et al.* (2015) hopefully demonstrate that the trends (i.e., the overall increase of effective Hall angle from FeMn to PdMn, IrMn, and PtMn for the reasons detailed in Fig. 35 and corresponding discussion) are qualitatively the same when similar samples are measured (see Table VI).

When interpreting these data, care must be taken when the antiferromagnetic material is in direct contact with a ferromagnet. Ferromagnetic/antiferromagnetic exchange-bias interactions (Sec. I.C.3) appear to increase the effective spin Hall angle compared to data obtained with ferromagnetic/nonmagnetic-metal/antiferromagnetic trilayers (Tshitoyan *et al.*, 2015); see Table VI. One should remember that for ferromagnetic/nonmagnetic/antiferromagnetic multilayers no direct exchange interaction takes place between ferromagnet and antiferromagnet, meaning that the transport regime is

purely electronic through the nonmagnetic metal (mostly Cu). In contrast, for ferromagnetic/antiferromagnetic multilayers, due to magnetic coupling, transfer and propagation of spin-angular momentum directly involves magnonic transport, i.e., spin waves from the oscillating ferromagnet feed directly into the antiferromagnet. As the origin of the spin transport is different, spin transmission efficiency (spin-mixing conductance) through interfaces may be significantly different (Sec. II.B). Tshitoyan *et al.* (2015) showed that the enhancement of the spin-angular-momentum transfer through a ferromagnetic/antiferromagnetic interface is indeed directly related to the interfacial exchange-coupling amplitude. Such an effect makes calculation of the actual spin Hall angle of the antiferromagnet more difficult. However, ferromagnetic/antiferromagnetic coupling increases the spin torque efficiency, making it an advantage for current-induced switching of the ferromagnet. Section III.D.4 focuses on the use of the multifunctionalities of antiferromagnets (spin Hall torques and exchange bias) to deterministically reverse the out-of-plane magnetization of a ferromagnet in zero applied magnetic field (Brink *et al.*, 2016; Fukami *et al.*, 2016; Lau *et al.*, 2016; Oh *et al.*, 2016; Sklenar *et al.*, 2016). Note also that Ou *et al.* (2016) further highlighted the importance and complexity of interfacial engineering (see also Sec. II.B.1). They demonstrated a twofold increase in spin torque efficiency in FeCoB/Hf/PtMn trilayers compared to FeCoB/PtMn bilayers. In this case, the reduction of transmission inherent to the separation of the FeCoB ferromagnet and the PtMn antiferromagnet is compensated by the increased transmission following the introduction of the Hf spacer. Similarly, the same groups showed that inserting a thin Hf layer between Pt and FeCoB layers improves spin-orbit torque efficiencies (Nguyen *et al.*, 2015).

Recently, Železný, Zhang *et al.* (2017) predicted that a charge current flowing through noncollinear antiferromagnets may become spin polarized, resulting in bulk spin currents. Similar to the spin currents present in ferromagnets, they possess a spin component longitudinal to the (antiferro) magnetic order parameter. In contrast to ferromagnets, noncollinear antiferromagnets also possess a spin component transverse to the magnetic order parameter. These longitudinal and transversal spin currents are odd under time reversal whereas spin Hall effect spin currents are even. Železný, Zhang *et al.* (2017) showed that the transversal contribution of spin currents in noncollinear antiferromagnets can be greater than the spin Hall effect spin currents, thus opening up new avenues for the understanding of spin-orbit torques in ferromagnet/noncollinear antiferromagnet bilayers.

### 3. Spin Hall magnetoresistance

Magnetic multilayers containing heavy metals adjacent to ferromagnets have recently been shown to display anisotropic magnetoresistance with symmetries differing from those traditionally found in bulk ferromagnets (Kobs *et al.*, 2011). While anisotropic magnetoresistance in bulk polycrystalline films depends on the angle between the flowing current and the magnetization direction  $\sim(\mathbf{m} \cdot \mathbf{j}_C)^2$  in ultrathin films an additional (interfacial) anisotropic magnetoresistance emerges that depends on the angle between the magnetization

and the direction transverse to the current flow  $\sim[\mathbf{m} \cdot (\mathbf{z} \times \mathbf{j}_C)]^2$ . Several mechanisms have been identified to explain this behavior, such as interfacial Rashba spin-orbit coupling (Wang, Pauyac, and Manchon, 2014; Zhang, Vignale, and Zhang, 2015) and a spin Hall effect in the normal metal adjacent to the ferromagnet (Chen *et al.*, 2013; Nakayama *et al.*, 2013). This effect has been reported in a wide range of magnetic multilayers and is designated under the broad name of spin Hall magnetoresistance. Since the effect is unaffected by magnetization reversal it would appear natural to observe it in antiferromagnetic multilayers (Manchon, 2017b). Indeed, it has been reported for several antiferromagnets: metallic IrMn in YIG/IrMn stacks (Zhou *et al.*, 2015), insulating SrMnO<sub>3</sub> in SrMnO<sub>3</sub>/Pt stacks (Han *et al.*, 2014), and insulating NiO in Pt/NiO/YIG trilayers (Shang *et al.*, 2016; Hou *et al.*, 2017; Hung *et al.*, 2017; Lin and Chien, 2017).

With metallic antiferromagnets, much attention must be paid to disentangling spin Hall magnetoresistance from anisotropic magnetoresistance induced in the antiferromagnet by potential uncompensated magnetic moments (also referred to as magnetic proximity effects). To do so, systematic angular dependences of the magnetoresistance must be determined. For example, in YIG/IrMn bilayers, Zhou *et al.* (2015) demonstrated that the competition between spin Hall magnetoresistance and magnetic proximity effects can lead to a peculiar sign change of the spin Hall-like magnetoresistance with temperature. Spin Hall magnetoresistance has also been reported in metallic FeMn/Pt bilayers (Yang *et al.*, 2016). However, in this work, the FeMn alloy was not antiferromagnetic. Its saturation magnetization was nonzero, with a value of 250 emu cm<sup>3</sup> for the 2 nm thick FeMn alloy and 25 emu cm<sup>3</sup> for 7 nm. As expected, the spin Hall magnetoresistance signal scaled with the residual ferromagnetism.

With regard to insulating antiferromagnets, several teams (Shang *et al.*, 2016; Hou *et al.*, 2017; Hung *et al.*, 2017; Lin and Chien, 2017) studied Pt/NiO/YIG trilayers. NiO was demonstrated to not only convey the spin information through spin waves to the YIG (see Table V) but to be the source of the magnetoresistive signal (Hou *et al.*, 2017). This effect was linked to enhanced spin Hall magnetoresistance at the magnetic phase transition of NiO (Hou *et al.*, 2017; Lin and Chien, 2017). An unconventional negative signal was also detected (Shang *et al.*, 2016; Hou *et al.*, 2017; Lin and Chien, 2017). Hou *et al.* (2017) suggested that this negative signal is due to spin-flop coupling (90° exchange coupling) between the NiO and YIG magnetic orders, whereas Lin and Chien (2017) linked the effect to spin-flip reflection from the NiO antiferromagnet exchange coupled with the YIG layer.

### D. Spin-orbit torques

#### 1. Principle of spin-orbit torques

In magnetic systems lacking inversion symmetry (globally or locally) and possessing sizable spin-orbit coupling, the transfer of angular momentum between the orbital angular momentum of carriers and the spin-angular moment of the localized electrons results in so-called spin-orbit torques [see, e.g., the following general articles: Gambardella and Miron

(2011), Brataas and Hals (2014), and Manchon (2014)]. Current-driven switching [e.g., in Pt/Co (Miron *et al.*, 2011) and Ta/CoFeB (Liu *et al.*, 2012) stacks], resonance (Liu *et al.*, 2011) and domain-wall motion (Miron *et al.*, 2010) in transition metals, as well as in noncentrosymmetric magnetic semiconductors [(Ga,Mn)As, (Ga,Mn)(As,P), and (Ni,Mn)Sb] (Chernyshov *et al.*, 2009; Fang *et al.*, 2011; Kurebayashi *et al.*, 2014; Ciccarelli *et al.*, 2016) have attracted much attention in the past five years, opening fascinating venues for nonvolatile memory and logic applications.

Up until now, two main mechanisms have been identified as the origin of spin-orbit torque: bulk or interfacial inverse spin galvanic effect and spin Hall effect. The former is the electrical generation of a nonequilibrium spin density [see Fig. 36(a)]. In systems lacking (bulk or interfacial) inversion symmetry, the spin-orbit coupling becomes odd in momentum. Examples are linear and cubic Dresselhaus spin-orbit coupling in strained zinc-blende semiconductors, Rashba spin-orbit coupling in bulk wurtzite, and at interfaces between dissimilar materials as well as cubic Rashba spin-orbit coupling in oxide heterostructures (Manchon *et al.*, 2015). Such odd-in- $k$  spin-orbit coupling enables current-driven spin densities that can be used for switching the magnetization direction of ferromagnetic materials. On the other hand, a heavy metal adjacent to the ferromagnet can create spin-orbit torques driven by the spin Hall effect [see Fig. 36(b)]. Through the combination of in-plane charge current and spin-orbit interaction in the heavy metal, a pure spin current is induced orthogonal to the electric current, thereby exerting a torque on the neighboring ferromagnet. Both inverse spin galvanic and spin Hall effects produce a torque of the form

$$\boldsymbol{\tau} = \tau_{\parallel} \mathbf{m} \times [(\mathbf{u} \times \mathbf{j}_C) \times \mathbf{m}] + \tau_{\perp} \mathbf{m} \times (\mathbf{u} \times \mathbf{j}_C), \quad (35)$$

where  $\mathbf{u}$  is a unit vector determined by the symmetry of the system and  $\mathbf{j}_C$  is the current density. In the case of a magnetic multilayer perpendicular to  $\mathbf{z}$ , as depicted in Fig. 36(b)  $\mathbf{u} = \mathbf{z}$ . As in the case of spin-transfer torque (see Sec. II.A.1), the first term is named the dampinglike torque, while the second is called the fieldlike torque.

Note that spin-orbit torques present some crucial differences compared to spin-transfer torques. Spin-transfer torques require the existence of two ferromagnets: the first one acts as a spin polarizer and the second acts as the free layer. In contrast, spin-orbit torques require only inversion symmetry breaking, and no

additional ferromagnetic spin polarizer. Hence, they cover both spin Hall torque and inverse spin galvanic torque, in spite of their very different origin. The inverse spin galvanic torque is really an intrinsic torque, taking advantage of the nature of the spin-orbit coupling in bulk or at the interface of the magnet (Bernevig and Vafeek, 2005; Manchon and Zhang, 2008; Garate and MacDonald, 2009), while spin Hall torque arises from a spin current generated away from the interface, in the bulk of the heavy metal (Haney *et al.*, 2013).

Both torques, inverse spin galvanic torque and spin Hall torque, are also present in antiferromagnetic systems lacking inversion symmetry and can provide a unique tool to manipulate the magnetic order, as predicted (Železný *et al.*, 2014) and demonstrated recently (Wadley *et al.*, 2016). Železný, Gao *et al.* (2017) recently analyzed the symmetries of spin-orbit torques in magnets lacking either local or global inversion symmetry, determining the tensorial forms of the torques for the different noncentrosymmetric point groups.

## 2. Manipulation of the order parameter by spin-orbit torque

The simplest model system on which such a spin-orbit torque has been proposed is the Rashba antiferromagnetic two-dimensional electron gas (Železný *et al.*, 2014). The band structure of this system presents striking differences with the ferromagnetic Rashba system, as illustrated in Fig. 37. In fact, in a normal metal with Rashba spin-orbit coupling the low-energy dispersion of the eigenstates is given by  $\epsilon_k^s = \hbar^2 k^2 / 2m + sak$  [see Fig. 37(a)], while in ferromagnets, the band structure is given by  $\epsilon_k = \hbar^2 k^2 / 2m + s\sqrt{\Delta^2 + a^2 k^2}$  [see Fig. 37(b)—we take the magnetization perpendicular to the plane for simplicity]. Here  $a$  is the Rashba spin-orbit coupling parameter,  $\Delta$  is the  $s$ - $d$  exchange energy, and  $s = \pm 1$  refer to the different spin chiralities. While Rashba spin-orbit coupling splits the electronic bands of normal metals, in ferromagnets there is a direct competition between the exchange and Rashba spin-orbit coupling and in the large exchange limit the spin splitting is mostly driven by the exchange. In contrast, in antiferromagnets  $\epsilon_k = \eta(\sqrt{\gamma_k^2 + \Delta^2} + sak)$  [see Eq. (4), Sec. I.C.1], i.e., the spin splitting is directly given by Rashba spin-orbit coupling, no matter how strong the exchange [see Fig. 37(c)]. Here  $\eta = \pm 1$  refers to the valence and conduction bands.

As a consequence, in the case of ferromagnetic Rashba gas with disorder broadening  $\Gamma$ , the two components of the torque

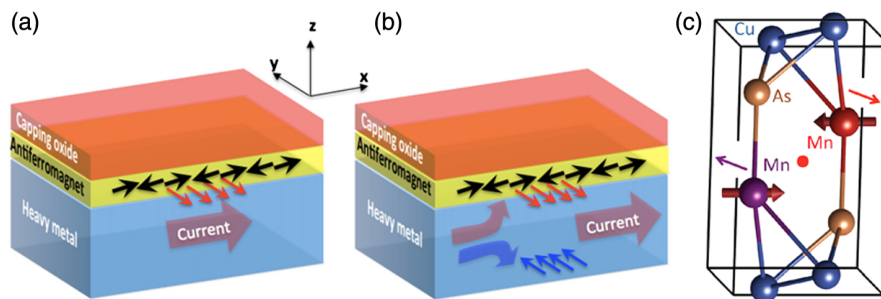


FIG. 36. Schematics of various origins of the spin-orbit torque: (a) inverse spin galvanic effect arising at the interface with the heavy metal, (b) spin Hall effect taking place in the bulk of the heavy metal, and (c) inverse spin galvanic effect emerging from bulk inversion asymmetry, from Jungwirth *et al.*, 2016.

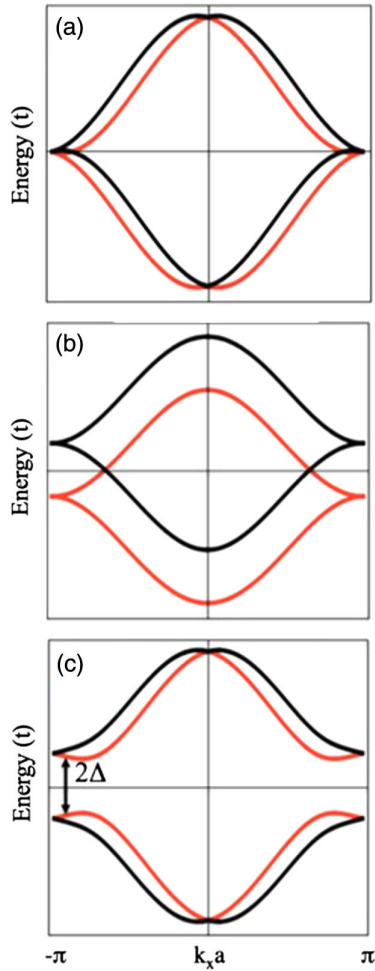


FIG. 37. Band structure of (a) a normal metal with Rashba spin-orbit coupling, (b) a ferromagnet with Rashba spin-orbit coupling, and (c) an antiferromagnet with Rashba spin-orbit coupling (generalization of Fig. 1 to the case of any nonzero spin-orbit term). These band structures were calculated for a nearest-neighbor tight-binding model with the same parameters. (a) and (c) are obtained by adding the Rashba term  $\hat{H}_R = \alpha \hat{\tau}_x \otimes \hat{\sigma} \cdot (\vec{k} \times \vec{z})$  to the Hamiltonian given in Eq. (3).

scale  $\tau_{\perp} \propto \alpha/\Gamma$ ,  $\tau_{\parallel} \propto \alpha/\Delta$  [strong exchange limit in the Kubo formalism—see, e.g., Li *et al.* (2015)], while in the case of an antiferromagnetic Rashba gas, it reads  $\tau_{\perp} \propto \alpha/\Gamma$ ,  $\tau_{\parallel} \propto \alpha\Delta/\varepsilon_F^2$  (Železný, Gao *et al.*, 2017). The first term is the intraband contribution, it arises from perturbation of the carrier distribution function by the electric field and is an extrinsic contribution to the nonequilibrium spin density, i.e., it is impurity dependent. This intraband contribution is proportional to the charge conductivity. The second term is an interband contribution, i.e., it arises from perturbation of the wave function under the electric field and is therefore independent of the scattering in the weak scattering limit. This contribution can be formally related to the Berry curvature of the band structure in mixed spin-momentum space and is therefore an intrinsic material property in the clean limit (Kurebayashi *et al.*, 2014).

Overall, it was demonstrated that the spin density on sublattice  $i$ , besides a strong angular dependence, reads

$$\mathbf{S}_i = s_{\perp} \mathbf{z} \times \mathbf{j}_C + s_{\parallel} \mathbf{m}_i \times (\mathbf{z} \times \mathbf{j}_C). \quad (36)$$

More specifically, the inverse spin galvanic effect arising from intraband transitions (first term) produces the same spin density on the two sublattices  $s_{\perp}$ , while the magnetoelectric effect arising from interband transitions produces a staggered spin density  $s_{\parallel}$ , which thus induces the torque efficient for the electrical control of the order parameter (Železný *et al.*, 2014).

In the same theoretical study, Železný *et al.* reported that current-induced “Néel-order” spin-orbit fields whose sign alternates between the spin sublattice can arise even in the bulk of centrosymmetric antiferromagnets such as  $\text{Mn}_2\text{Au}$  [or  $\text{CuMnAs}$ , see Fig. 36(c)]. The general case of spin polarization due to atomic site asymmetries within the crystal rather than space-group asymmetries was also developed by X. Zhang *et al.* (2014). Actually, each sublattice has broken inversion symmetry but together form “inversion partners.” Then, each sublattice experiences an opposite inverse spin galvanic effect (Železný *et al.*, 2014). Therefore, in this case, the efficient torque enabling the manipulation of the order parameter is a staggered fieldlike torque [see Fig. 14(b)]. Roy, Otxoa, and Wunderlich (2016) used the example of  $\text{Mn}_2\text{Au}$ -based devices to further compute the influence of spin-orbit field strength, current pulse properties, and damping on switching. They demonstrated robust picosecond writing with minimal risk of overshoot. These pioneering studies are encouraging in view of triggering antiferromagnetic order reversal by current injection.

#### a. Manipulation by inverse spin galvanic torque

Recently, the current-driven order parameter reversal in antiferromagnets was indeed observed [Figs. 36(a) and 38]: in  $\text{CuMnAs}$  via global electrical measurements (anisotropic magnetoresistance) (Wadley *et al.*, 2016; Olejnik *et al.*, 2017a) as well as via local direct imaging of the antiferromagnetic domains (x-ray magnetic linear dichroism photoelectron emission microscopy) (Grzybowski *et al.*, 2017), and in  $\text{Mn}_2\text{Au}$  via global electrical measurements (anisotropic magnetoresistance) (Bodnar *et al.*, 2017; Meinert, Graulich, and Matalla-Wagner, 2017).  $\text{CuMnAs}$  and  $\text{Mn}_2\text{Au}$  crystals possess local inversion symmetry breaking in bulk crystal, as explained (see also Table III), and display anisotropic magnetoresistance allowing for the electrical detection of the order parameter orientation. Wadley *et al.* demonstrated that the order parameter could be switched reversibly by  $90^\circ$  upon electrical injection. While numerous aspects are under deeper investigation [e.g., the role of temperature (Meinert, Graulich, and Matalla-Wagner, 2017), details of the reversal dynamics (Olejnik *et al.*, 2017b), and the mechanism of domain formation], these experiments constitute the first clear demonstration of current-driven Néel order manipulation. Most importantly for applications, Olejnik *et al.* (2017b) recently demonstrated ultrafast reversible switching in  $\text{CuMnAs}$  using 1 ps long writing pulses obtained from THz electromagnetic transients. This reversal is 2 orders of magnitude faster than the one obtained from ferromagnets using spin-orbit torques (Garello *et al.*, 2014), establishing the advantage of antiferromagnets for ultrafast operation.

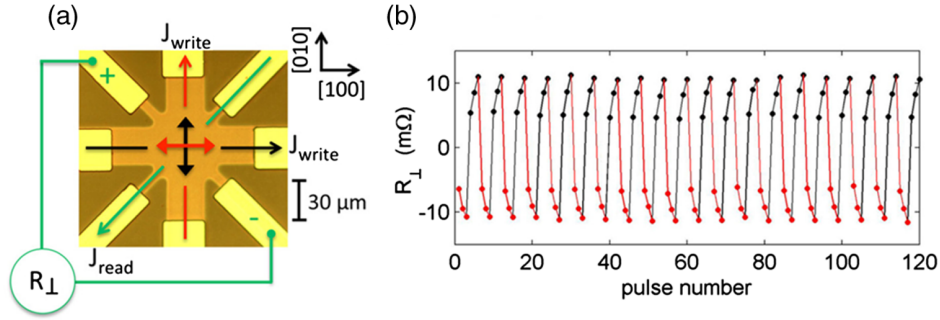


FIG. 38. Current-induced switching of CuMnAs with the inverse spin galvanic effect and subsequent electrical detection with the anisotropic magnetoresistance effect. From [Wadley \*et al.\*, 2016](#).

### b. Manipulation by spin Hall torque

Another promising configuration is to use the spin Hall effect arising from an adjacent heavy metal [see Fig. 36(b)]. Strictly speaking, this torque behaves as a spin-transfer torque (Sec. II) from a virtual ferromagnet polarized along the spin Hall polarization direction, i.e.,  $\sim \mathbf{z} \times \mathbf{j}_C$ . The torque is therefore a dampinglike torque with the form  $\mathbf{m} \times [(\mathbf{z} \times \mathbf{j}_C) \times \mathbf{m}]$  [see Fig. 14(c)]. These bilayer structures present some advantages compared to ferromagnet/spacer/antiferromagnet spin valves, as the spin current is directly injected from the normal metal into the antiferromagnet and survives in the diffusive regime ([Manchon, 2017a](#)). Learning how to exploit spin Hall torques to reverse the antiferromagnetic order is yet another challenge to be addressed.

Experimentally, spin Hall torque was reported by [Reichlová \*et al.\* \(2015\)](#) in Ta/IrMn, using the second harmonic method. Detectability of the signal below the Néel temperature and its insensitivity to external fields supported the hypothesis that the torque relates to the antiferromagnetic order. Other attempts reported efficient spin Hall assisted magnetic order reversal in FeMn and IrMn alloys ([Han \*et al.\*, 2016](#); [Yang \*et al.\*, 2016](#)). However, these alloys were directly grown on SiO<sub>2</sub> layers, a process which is known to hamper the production of good quality antiferromagnets. As a result, FeMn and IrMn alloys with nonzero saturation magnetization were obtained. A value of 250 emu cm<sup>3</sup> was reported for the 2 nm thick FeMn alloy and 25 emu cm<sup>3</sup> for the 7 nm thick alloy ([Yang \*et al.\*, 2016](#)). The low saturation magnetization of the (nonantiferromagnetic) FeMn and IrMn alloys on SiO<sub>2</sub> readily explains the large effective fields (low critical current) obtained.

Although spin Hall torque presents opportunities in terms of system design, the dynamics of spin Hall driven antiferromagnets are no different from those of the spin-torque-induced systems initially studied by [Gomonay and Loktev \(2010, 2014\)](#). Current-driven switching and excitations are governed by the same physics. In a recent study, [Cheng, Xiao, and Brataas \(2016\)](#) proposed exploitation of the spin Hall torque to trigger THz oscillations. In their study, they considered the case of a biaxial antiferromagnet and showed that when the spin Hall torque is increased, the frequency of the optical mode is progressively reduced, while the frequency of the acoustic mode is enhanced. At the critical value  $J_{cr}$  both modes are degenerate, which triggers THz excitations (see Fig. 39). Uniform steady state oscillations can be sustained

thanks to the dynamic feedback from the pumped spin current: the spin-current backflow renormalizes the spin-transfer torque in a nonlinear manner, which is sufficient to stabilize the THz oscillations ([Cheng, Zhu, and Xiao, 2016](#)). Note that in this case the critical current is given by Eq. (25), with  $\omega_{AF} = \gamma\mu_0 \sqrt{H_{\perp}^2/4 + \alpha^2(2H_{\parallel} + H_{\perp})H_E}$ , i.e., it is mostly governed by the hard-axis anisotropy. Using parameters for NiO, they predicted a critical current density of about  $10^8$  A cm<sup>-2</sup>. The oscillation threshold could be further reduced by considering a uniaxial antiferromagnet ( $H_{\perp} \rightarrow 0$ ) such as MnF<sub>2</sub>. Finally, in a recent work [Daniels \*et al.\* \(2015\)](#) investigated the ability of spin Hall torque to drive spin-wave excitations in model insulating antiferromagnets. Their results indicated that surface spin waves can be excited at much lower current density than bulk spin waves due to surface anisotropy. A similar effect had previously been observed in ferromagnetic insulators ([Xiao and Bauer, 2012](#)).

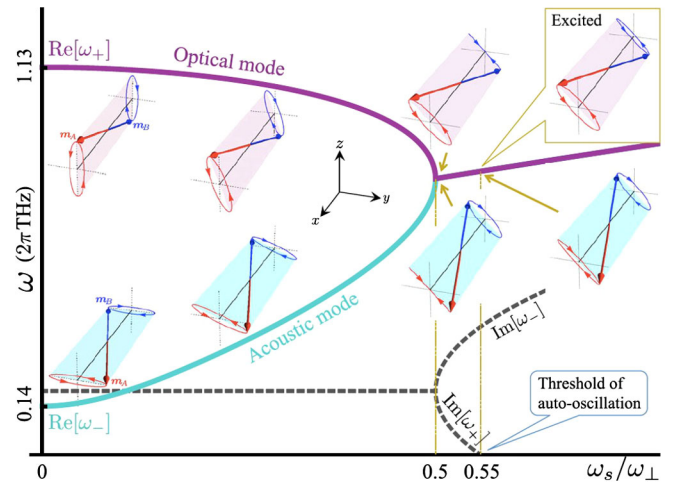


FIG. 39. Evolution of the eigenfrequencies of NiO submitted to spin Hall torque. In the region  $\omega_s < \omega_{\perp}/2$ , the frequency of the optical mode is reduced while the frequency of the acoustic mode increases. Note that the sublattice moments  $\mathbf{m}_{A,B}$  oscillate with opposite chiralities. At  $\omega_s = \omega_{\perp}/2$ , both modes are degenerate, whereas above  $\omega_s > 0.55\omega_{\perp}$ , auto-oscillations are triggered. In this regime,  $\mathbf{m}_{A,B}$  and the Néel vector  $\mathbf{l}$  oscillate with the same chiralities. Here  $\omega_{\perp} = \gamma\mu_0 H_{\perp}$ , where  $H_{\perp}$  is the out-of-plane anisotropy as defined in the text. From [Cheng, Xiao, and Brataas, 2016](#).



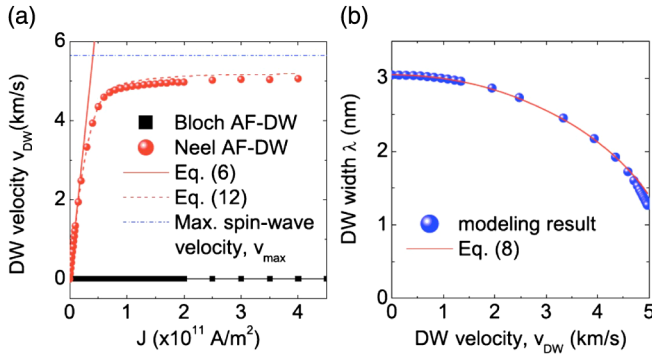


FIG. 40. (a) Domain-wall velocity as a function of current density in the presence of spin Hall torque. The blue dot-dashed line represents the spin-wave velocity which sets the upper bound for domain-wall velocity. Note that only Néel domain walls can be moved by spin Hall torque. (b) Domain-wall width as a function of domain-wall velocity, displaying Lorentz contraction. Note that Eqs. (6), (8), and (12) from the figure refer to equations defined in Shiino *et al.* (2016) and not to equations from the present review article. From Shiino *et al.*, 2016.

### 3. Moving magnetic textures by spin-orbit torque

Spin-orbit torques, such as dampinglike and staggered fieldlike torques, present an interesting paradigm for the manipulation of antiferromagnetic textures. Two theoretical studies recently investigated the motion of domain walls in the presence of staggered fieldlike torques (Gomonay, Jungwirth, and Sinova, 2016) and in the case of spin Hall (dampinglike) torques (Shiino *et al.*, 2016). The former modeled the current-driven motion of domain walls in bulk noncentrosymmetric antiferromagnet such as CuMnAs, while the latter aimed at modeling Néel walls in antiferromagnet/normal metal bilayers. In both cases, they emphasized that the azimuthal angle of the wall was not affected by the current, in sharp contrast with what occurs in ferromagnets. As a result, antiferromagnetic domain walls do not experience Walker breakdown and can reach very high velocities (as introduced in Sec. I.C.4). The largest velocity attainable by the wall is set by the spin-wave velocity, of the order of 1 to 10 km s<sup>-1</sup> for current densities of about  $10^7$  A cm<sup>-2</sup>. This is about 2 orders of magnitude more efficient than what can be achieved with ferromagnetic domain walls. Close to this upper limit, antiferromagnetic domain walls experience Lorentz contraction (see Fig. 40) (and emit spin waves in the THz regime. These predictions are encouraging for the development of domain-wall control. Current experimental development is focused on producing current-driven domain-wall motion.

### 4. Current-induced switching by antiferromagnets

More recently, researchers used spin Hall torques produced by antiferromagnets (see Sec. III.C.2) to excite and reverse ferromagnets without applying any external magnetic fields. The magnetization direction of ferromagnets with in-plane magnetic anisotropy can be reversed by spin Hall torques in zero applied magnetic field (Liu *et al.*, 2012). However, ferromagnets with out-of-plane anisotropy require additional symmetry breaking, for example, by applying an in-plane

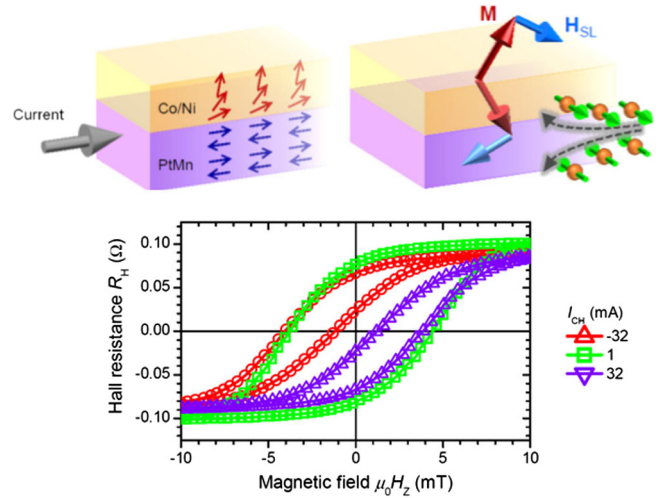


FIG. 41. An antiferromagnet can be used to switch a ferromagnet: ferromagnetic/antiferromagnetic exchange bias and current-induced spin Hall torques from the antiferromagnet combine to reverse the magnetization direction of a ferromagnet with out-of-plane anisotropy. Adapted from Fukami *et al.*, 2016.

magnetic field (along the current flow direction) (Cubukcu *et al.*, 2014) or by introducing geometric asymmetries (Yu *et al.*, 2014; Safeer *et al.*, 2015), for spin Hall torques to switch their magnetization in a deterministic way.

Four groups (Brink *et al.*, 2016; Fukami *et al.*, 2016; Lau *et al.*, 2016; Oh *et al.*, 2016) simultaneously used the magnetic interactions between a ferromagnet with out-of-plane anisotropy (Co/Ni, CoFe and CoFe/Ni, Co/Pt, CoFeB) and an antiferromagnet (PtMn, IrMn) to create in-plane exchange bias and break the symmetry. Their results showed that the spin Hall torques, either directly from the antiferromagnet (Fukami *et al.*, 2016; Oh *et al.*, 2016) (see Fig. 41) or from an additional heavy metal (Brink *et al.*, 2016; Lau *et al.*, 2016) could then deterministically reverse the out-of-plane magnetization of the ferromagnet in zero applied magnetic field. In all these experiments, it was also confirmed that the dampinglike torque contribution prevails over the fieldlike torque contribution (see Sec. III.C and Table VI where the spin Hall effect in antiferromagnets is discussed, regardless of its further impact on neighboring ferromagnets). For example, Fig. 42 reproduces the findings of Zhang *et al.* (2015) for NiFe/Cu/antiferromagnet trilayers. The signatures of dampinglike and fieldlike torques were determined by measuring the changes in NiFe resonance linewidth and resonant frequency, respectively, when a dc current is injected in the plane of the antiferromagnet. For NiFe/Cu/PtMn trilayers, they found that the dampinglike torque contribution is 4 times more efficient than the fieldlike torque (see also Table VI).

## IV. SPIN CALORITRONICS AND SUPERFLUIDITY

Spin caloritronics aims at using thermal gradients to generate and manipulate spin currents (Bauer, Saitoh, and van Wees, 2012; Boona, Myers, and Heremans, 2014). This possibility is particularly interesting in insulating magnets, where spin currents are transported by spin waves rather than itinerant electrons. While most of the research in this area has

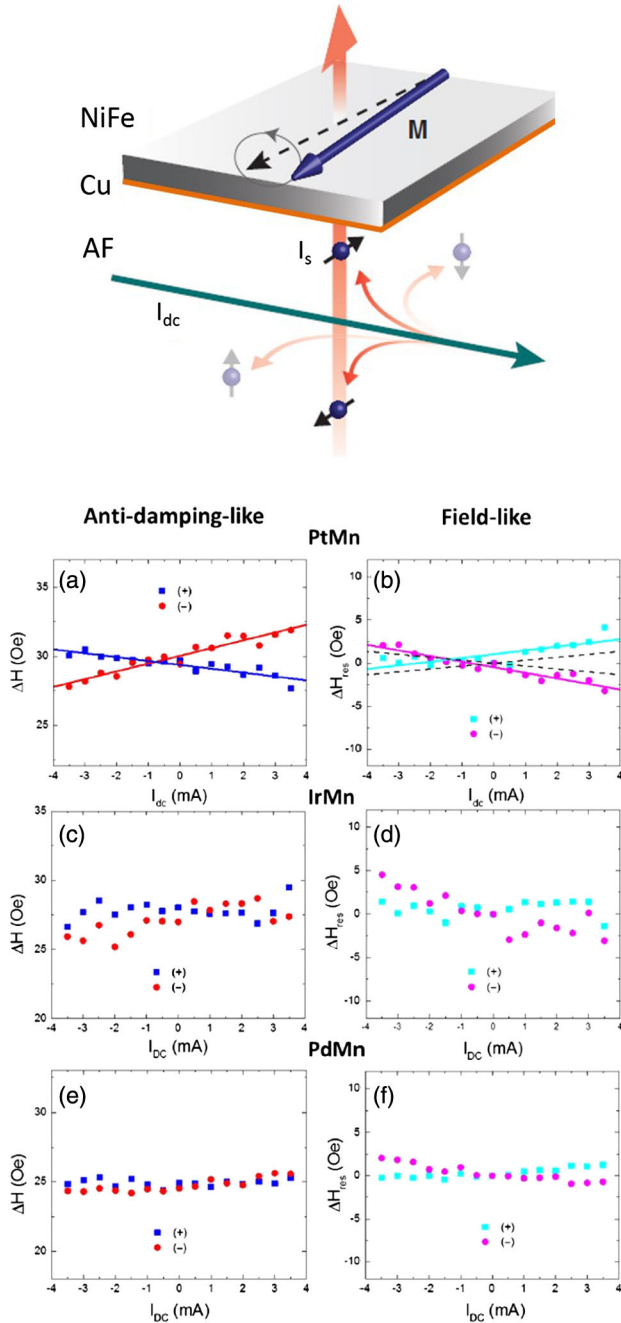


FIG. 42. (Top) The experimental setup. An in-plane dc current ( $I_{dc}$ ) flowing in the antiferromagnet (AF) generates transverse spin currents that modulate the magnetization dynamics (damping and/or resonance frequency) of a ferromagnetic NiFe layer. Adapted from [Ando \*et al.\*, 2008](#). (Bottom) Signatures of dampinglike and fieldlike torques based on measurement of the changes in resonance linewidth and resonant frequency with  $I_{dc}$  for positively (+) and negatively (-) magnetized NiFe. From [Zhang \*et al.\*, 2015](#).

focused on ferromagnets (and, in particular, on the yttrium iron garnet ferromagnetic insulator), progress has recently been made in the field of antiferromagnets. This section reviews the latest achievements in this field in terms of thermal generation of spin current and spin transport (Sec. II.B) driven by antiferromagnetic spin waves.

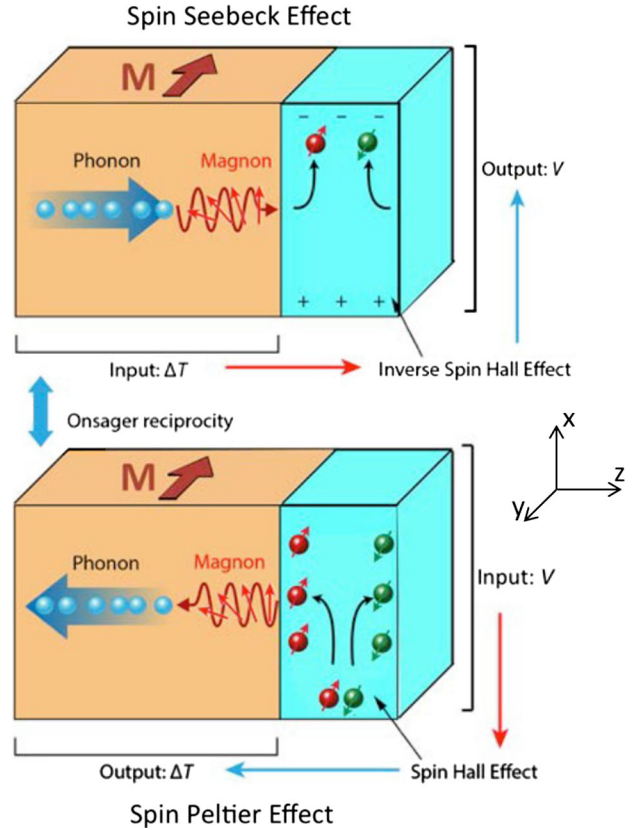


FIG. 43. The reciprocal spin Peltier and spin Seebeck effects manifested in a heavy metal/magnetic insulator bilayer. A mutual viscous drag can significantly impact the coupled thermal transport of magnons and phonons in the insulator. From [Hellman \*et al.\*, 2017](#).

### A. Thermally induced spin currents

Spin currents can be readily induced in magnetic insulators by the application of a thermal gradient. The prototypical example of this was established by the demonstration of the spin Seebeck effect at the interface between a heavy metal and ferrimagnetic yttrium iron garnet ([K. Uchida \*et al.\*, 2010a, 2010b](#)). The thermal gradient applied normal to the interface is believed to induce a magnonic spin current in the magnetic insulator, which is converted into an electronic spin current via the exchange coupling between (*s*-like) itinerant and the (*d*-like) localized spins at the interface. The latter is then detected as a transverse voltage via the inverse spin Hall effect (see Sec. III.C.2). Phenomenologically, the spin Seebeck physics is thus manifested as a Nernst effect of the heavy metal/magnetic insulator bilayer (Fig. 43), i.e., transversal voltage in response to a thermal gradient is produced due to the combination of the spin Seebeck effect in the magnetic insulator and the inverse spin Hall effect in the metal.

The essential physics at the interface is the exchange induced spin-magnon transmutation: itinerant electrons scattering off the interface can inelastically flip their spin  $\hbar/2$  while producing a spin- $\hbar$  magnon. The magnons, in turn, can decay at the interface, while reemitting a spin- $\hbar$  electron-hole pair (see Fig. 44). Since magnons carry energy as well as

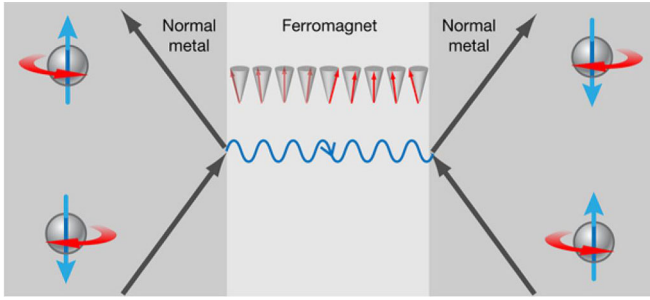


FIG. 44. Generation of a magnon (directional wavy line and snapshot of the magnetization) associated with an electron spin flip indicated by spheres, at the left interface between normal metal and ferromagnet, and the reciprocal magnon decay at the right interface. Such electron spin-flip processes accompanied by creation and annihilation of magnons are expected for any collinear magnetic system, including antiferromagnets. From Bauer and Tserkovnyak, 2011.

spin, these inelastic processes reflect the intimately coupled nature of the spin and heat flows in magnetic insulators. Macroscopically, these magnon creation and decay processes are manifested through the Onsager-reciprocal spin-transfer torque and spin pumping (Tserkovnyak *et al.*, 2005; Brataas *et al.*, 2012).

The theory of such interfacially induced thermal spin currents produced by a ferromagnetic insulator is well established, at least qualitatively. With the early efforts being based on a semiclassical stochastic Landau-Lifshitz-Gilbert treatment (Xiao *et al.*, 2010; Hoffman, Sato, and Tserkovnyak, 2013), a systematic quantum-kinetic description was formulated by Bender and Tserkovnyak (2015). In general, the spin and the associated heat flow at a magnet/metal interface are driven by the effective temperature as well as chemical potential drops over the interface (with the counterpart of the magnonic chemical potential on the metallic side being provided by the spin accumulation, i.e., the vectorial difference of the spin-up and spin-down electronic chemical potentials) (Bender and Tserkovnyak, 2015). For example, when the spin accumulation  $\mu_s$  is collinear with the magnetic order parameter, the interfacial spin current (which is polarized along the same direction) is given by (Bender, Duine, and Tserkovnyak, 2012; Bender *et al.*, 2014)

$$j_x = \frac{\hbar g^{\uparrow\downarrow}}{\pi s} \int_{\hbar\omega}^{\infty} d\epsilon D(\epsilon)(\epsilon - \mu_s) \{ n_{\text{BE}}[(\epsilon - \mu)/k_B T_m] - n_{\text{BE}}[(\epsilon - \mu_s)/k_B T_e] \}, \quad (37)$$

where  $\mu$  is the magnonic chemical potential,  $T_m$  and  $T_e$  are the magnon and electron temperatures, respectively,  $g^{\uparrow\downarrow}$  is the (real part of the) spin-mixing conductance (Tserkovnyak *et al.*, 2005; Brataas, Bauer, and Kelly, 2006) parametrizing the exchange-coupling strength at the interface,  $D(\epsilon)$  is the magnon density of states,  $\hbar\omega$  is the magnon gap, and  $n_{\text{BE}}(x) \equiv (e^x - 1)^{-1}$  is the Bose-Einstein distribution function. The energy flux is given by a similar expression but with an additional factor of  $\epsilon/\hbar$  in the integrand. Together, when linearized with respect to  $T_m - T_e$  and  $\mu - \mu_s$ , these coupled spin and heat flows mimic the Onsager-reciprocal thermo-electric transport of electrons (Mahan, 2000).

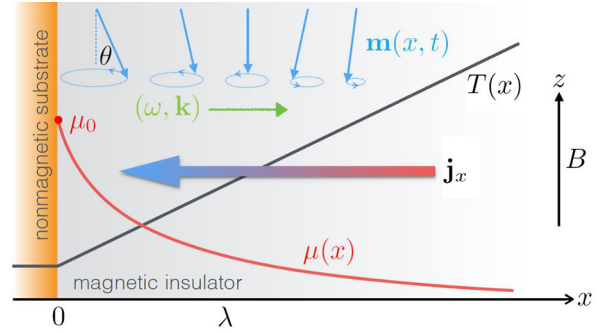


FIG. 45. A monodomain ferromagnet with uniform equilibrium spin density pointing in the  $-z$  direction (in the presence of a magnetic field  $B$  pointing up along  $z$ ). A positive thermal gradient  $\partial_x T > 0$  induces magnonic flux  $\mathbf{j}_x$  toward the interface, where an excess of thermal magnons accumulates over their spin-diffusion length  $\lambda$ . When the corresponding nonequilibrium interfacial chemical potential  $\mu_0$  reaches a critical value (exceeding the magnon gap), the magnetic order undergoes a Hopf bifurcation toward a steady precessional state, where Gilbert damping and radiative spin-wave losses are replenished by the thermal-magnon pumping  $\propto \mu_0$ . The coherent transverse magnetic dynamics decays away from the interface as  $m_x - im_y \propto e^{i(kx - \omega t)}$ , where  $\text{Im}k > 0$ . From Tserkovnyak *et al.*, 2016.

A likely dominant route to establish such a bias at the interface upon subjecting the bilayer to a normal thermal gradient is the magnonic spin Seebeck effect in the magnetic bulk, which leads to a magnon pileup at the interface (Flebus *et al.*, 2016). For a small thermal gradient, the latter results in the linear-response interfacial spin and heat flow, while for a large enough thermal bias a Bose-Einstein condensation of magnons can ensue near the interface (Tserkovnyak *et al.*, 2016), which is schematically depicted in Fig. 45. This condensation leads to a spontaneously coherent precession of the magnetic order parameter.

In simple antiferromagnets, the spin Seebeck effect in the bulk vanishes due to the sublattice symmetry (which is also true for the interfacial spin flow, if the interface is fully compensated and effectively respects this symmetry). For example, for the case of the easy-axis bipartite antiferromagnet, according to the axial symmetry, the magnon bands should be double degenerate, corresponding to spin projections  $\pm\hbar$  along the easy axis. These bands carry finite but opposite spin currents in response to a temperature gradient. However, when applying a magnetic field along the easy axis, the subband symmetry is lifted (Sec. I.C.3) and a spin Seebeck effect emerges, with the spin current polarized along the magnetic field. This was recently demonstrated experimentally (Seki *et al.*, 2015; S. M. Wu *et al.*, 2016) (see Fig. 46) and studied theoretically (Rezende, Rodríguez-Suárez, and Azevedo, 2016a).

A net spin current in a magnetically compensated antiferromagnet can be injected by coherent spin pumping from an adjacent ferromagnet or by spin Hall effect from an adjacent normal metal (see Secs. II.B and III.C.2). Both can be demonstrated in the same ferromagnet/antiferromagnet/metal trilayer, where the ferromagnet and the metal can serve interchangeably as either injector or detector of spin currents. A theoretical framework for antiferromagnet-mediated spin

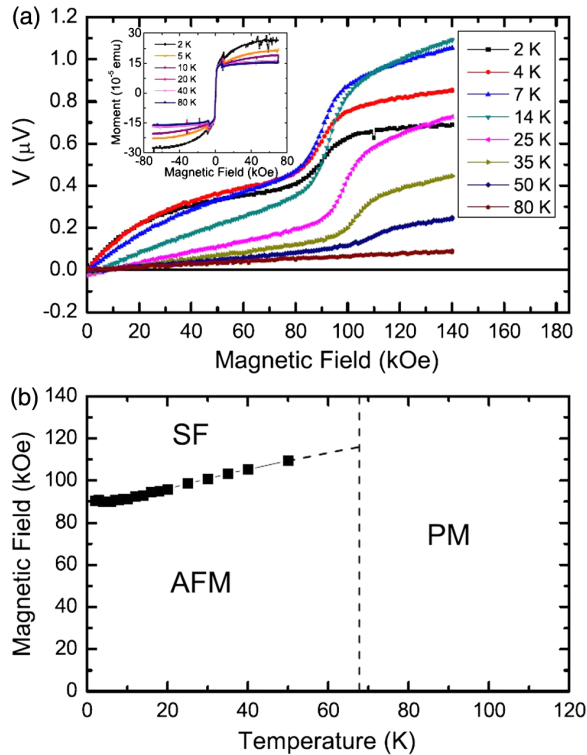


FIG. 46. The spin Seebeck voltage (top panel) measured as a function of the magnetic field along the easy axis for a  $\text{MgF}_2/\text{MnF}_2/\text{Pt}/\text{MgO}/\text{Ti}$  multilayer. The sharp upturn in the signal corresponds to the spin-flop transition. The bottom panel shows the phase diagram of  $\text{MnF}_2$  according to the existence and location of this upturn. AFM stands for the (collinear) antiferromagnet, SF the spin-flopped (canted) antiferromagnet, and PM the paramagnet (above the Néel temperature). From S. M. Wu *et al.*, 2016.

currents in such trilayers was established for the coherent coupled low-temperature dynamics (Takei *et al.*, 2015; Khymyn *et al.*, 2016), where the spin current in the antiferromagnet is carried by an evanescent spin-wave mode. At finite temperatures, thermal magnons open an additional channel for spin transport (Rezende, Rodríguez-Suárez, and Azevedo, 2016b). The precessing magnetization in the adjacent ferromagnet would pump differently the oppositely polarized magnons in the antiferromagnet. Spin conduction through magnetic insulators was first experimentally demonstrated in 2014, simultaneously by H. Wang *et al.* (2014) and Hahn *et al.* (2014) using NiO in YIG/NiO/Pt trilayers (see also Table V). H. Wang *et al.* (2014) observed efficient dynamic spin injection from YIG into NiO as a result of strong coupling. Tshitoyan *et al.* (2015) went on to demonstrate the direct relation between spin-angular momentum transfer efficiency and ferromagnetic/antiferromagnetic coupling. H. Wang *et al.* (2014) also confirmed robust spin propagation in NiO up to 100 nm thick (i.e., a characteristic decay length of around 10 nm, see Table V). This effect was mediated by its antiferromagnetic spin correlations. In contrast, Hahn *et al.* (2014) reported poor interface transparency, of the order of 10%, possibly due to nonoptimal interface quality. The propagation length they measured was also not consistent with a picture of mobile antiferromagnetic spin correlations. Unlike H. Wang *et al.* (2014) and Hahn *et al.* (2014), Lin *et al.* (2016) used the spin Seebeck effect to inject

magnons into NiO. Since spin Seebeck results in dc injection, they were able to confirm the dominant role of thermal magnons in the propagation process. Finally, H. Wang *et al.* (2015) demonstrated systematic long-distance spin transport in several antiferromagnetic insulators in YIG/antiferromagnet/Pt trilayers (see Table V). They found a strong correlation between spin propagation and antiferromagnetic ordering temperatures highlighting the critical role of magnetic correlations. They also found a correlation between spin propagation and extrinsic contributions to YIG damping, thus further highlighting the important role of the ferromagnetic/antiferromagnetic interface for spin transport in antiferromagnetic insulators. Spin conduction has also recently been demonstrated to be maximized, as a function of temperature, in the vicinity of the Néel temperatures of NiO and CoO (Qiu *et al.*, 2016) (spin pumping injection), (Lin *et al.*, 2016) (spin Seebeck injection), and NiFeOx (Frangou *et al.*, 2017) (spin pumping injection). Enhanced spin pumping efficiency due to magnetic fluctuations of antiferromagnetic spin absorbers was demonstrated at the same time in NiFe/Cu/IrMn trilayers where the spin current is purely electronic through Cu (Frangou *et al.*, 2016) (see also Sec. I.C.2). This enhanced efficiency is related to the fact that interfacial spin-mixing conductance depends on the transverse spin susceptibility of the spin absorber (Ohnuma *et al.*, 2014; Chen *et al.*, 2016), which is known to show a maximum around the antiferromagnetic-to-paramagnetic phase transition.

We note that thermal magnons in an antiferromagnet could similarly serve as spin conduits in other heterostructures and transport scenarios. One example related to the earlier discussion in this section could be an antiferromagnet-mediated spin Seebeck effect between a ferromagnet and a normal metal. Interestingly, the spin Nernst effect can generally be expected to be present in antiferromagnets as well, due to spin-orbit interactions, in analogy to spin Hall effect in metals [see, e.g., Hoffmann (2013) and Sinova *et al.* (2015)]. This effect is permitted even for the highest-symmetry classes of the most featureless materials. In fact, the spin Nernst effect is expected to be observed equally well in paramagnets and spin liquids. This effect does not rely on the presence of time-reversal symmetry breaking, unlike the thermal Hall effect (thermal analog of the Hall effect). Several recent papers (Cheng, Okamoto, and Xiao, 2016; Kim *et al.*, 2016; Zyuzin and Kovalev, 2016) demonstrated the spin Nernst effect in models of honeycomb lattice magnets with Dzyaloshinski-Moriya interactions.

With regard to magnetic textures, the interactions of thermally induced magnon spin currents with magnetic textures, particularly topological solitons, along with the accompanying thermal-gradient-induced entropic forces, have been explored in ferromagnetic insulators (Hinzke and Nowak, 2011; Kovalev, 2014; Schlickeiser *et al.*, 2014; Wang, Lian, and Zhang, 2014; Kim and Tserkovnyak, 2015a). The key problem of interest is thermophoresis, i.e., the net soliton drift induced by a thermal gradient. Depending on various details related to the interplay between entropic and thermomagnonic forces, magnetic solitons will move toward either hot or cold regions (Kim and Tserkovnyak, 2015a; Yan, Cao, and Sinova, 2015). The problem with coupling between thermal gradients and mobile order parameter textures is

attracting growing interest in antiferromagnets, as discussed in Sec. IV.C. Some of the elementary thermophoretic aspects can be understood thanks to close analogy with the ferromagnetic case.

## B. Superfluid spin transport

At low temperatures, thermal spin waves freeze out and cease to contribute to spin transport. The spin currents can still be transmitted by collective order parameter dynamics. To understand this, let us return to our basis starting with equations in Sec. II, which we rewrite as

$$\begin{aligned} \mathbf{m} &= \chi_{\perp} \mathbf{l} \times (s \partial_t \mathbf{l} + \mathbf{l} \times \mathbf{b}), \\ s(\partial_t \mathbf{m} + \alpha \mathbf{l} \times \partial_t \mathbf{l}) &= \partial_t (\mathbf{l} \times A \partial_t \mathbf{l}) - \mathbf{l} \times \partial_t \mathcal{F}_a + \mathbf{b} \times \mathbf{m} + \boldsymbol{\tau}_m. \end{aligned} \quad (38)$$

The second equation is readily interpreted as the continuity equation for the spin density  $\rho_s \equiv s\mathbf{m}$ :

$$\partial_t \rho_s + \partial_i \mathbf{j}_{s,i} = \boldsymbol{\tau}_\alpha + \boldsymbol{\tau}_a + \boldsymbol{\tau}_b + \boldsymbol{\tau}_m, \quad (39)$$

where  $\mathbf{j}_{s,i} \equiv -\mathbf{l} \times A \partial_i \mathbf{l}$  is the collective spin current,  $\boldsymbol{\tau}_\alpha \equiv -\alpha s \mathbf{l} \times \partial_t \mathbf{l}$  is the dampinglike torque describing the leakage of the spin-angular momentum into crystalline environment,  $\boldsymbol{\tau}_a \equiv -\mathbf{l} \times \partial_t \mathcal{F}_a$  is the reactive anisotropy torque,  $\boldsymbol{\tau}_b \equiv \mathbf{b} \times \mathbf{m}$  is the classic Larmor torque of the external field  $\mathbf{b}$  on the small magnetization  $\mathbf{m}$ , and  $\boldsymbol{\tau}_m$  is the spin-transfer torque associated with any other (itinerant) degrees of freedom, such as electrons (either in the bulk or at an interface).

In the generic case of an anisotropic antiferromagnet, such as the common easy-axis scenario, injecting a collective spin current at low (subgap) frequencies would decay over a healing length  $\sim \sqrt{A/K}$  governed by the anisotropy  $K$  (Takei and Tserkovnyak, 2015). This contrasts with the thermal spin current that decays in magnetic insulators over a temperature-dependent spin-diffusion length of magnons (Cornelissen *et al.*, 2015). At higher frequencies, the spin signals can be transmitted resonantly via the coherent spin-wave modes, which can propagate over much larger distances governed by the Gilbert damping (Takei and Tserkovnyak, 2015).

In the more interesting easy-plane case which could be realized when the  $z$ -axis anisotropy  $K < 0$  or in the absence of anisotropies (i.e., the pure Heisenberg limit) but with a magnetic field  $\mathbf{b} \parallel \mathbf{z}$ , we have an easy  $xy$ -plane magnet, mapping at low energies onto the  $XY$  model (Sonin, 1978, 2010; König, Bønsager, and MacDonald, 2001). In this limit, the spin density is approximately collinear with the  $z$  axis,  $\rho_s \approx \rho_s \mathbf{z}$ , while  $\mathbf{l}$  swings predominantly in the  $x$ - $y$  plane (which we can parametrize by the azimuthal angle  $\varphi$ ). The corresponding equations of motion for these low-energy degrees of freedom follow by projecting Eqs. (38) onto the  $z$  axis:

$$\partial_t \varphi = \rho_s / \chi_{\perp} s^2, \quad \partial_t \rho_s + \partial_i j_{s,i} = \tau_\alpha + \tau_m. \quad (40)$$

Here  $j_{s,i} = -A \partial_i \varphi$ ,  $\tau_\alpha = -\alpha s \partial_t \varphi$ , and  $\tau_m$  is the  $z$ -axis projection of the spin-transfer torque. We are still allowing  $\tau_m$  to be of a general form, either of bulk or interfacial nature, with the latter relevant for establishing the appropriate

boundary conditions for bulk dynamics. These coupled equations reflect a damped spin superfluid hydrodynamics (Takei and Tserkovnyak, 2014; Takei *et al.*, 2014), associated with the canonically conjugate (coordinate or momentum) pair of variables  $(\varphi, \rho_s)$ , with the Hamiltonian density

$$\mathcal{H} = \frac{\rho_s^2}{2\chi_{\perp} s^2} + \frac{A}{2} (\partial_i \varphi)^2, \quad (41)$$

and the Rayleigh function

$$\mathcal{R} = \frac{\alpha s}{2} (\partial_t \varphi)^2. \quad (42)$$

The destruction of the associated (topologically stable) superfluid spin currents by thermal and quantum phase slips has been studied by Kim, Takei, and Tserkovnyak (2016) and Kim and Tserkovnyak (2016), respectively. Quantum phase slips, which dominate at low temperatures, are particularly interesting in the case of easy-plane antiferromagnets and exhibit a topological character depending on whether the constituent spins are integer or half-odd-integer valued (profoundly affecting the superfluid-insulator quantum phase transition). While such superfluid spin flows were believed to be severely compromised by even a small parasitic anisotropy within the easy plane (Kohn and Sherrington, 1970; Sonin, 1978; König, Bønsager, and MacDonald, 2001), it gets effectively restored at finite temperatures by topological spin transport carried by Brownian diffusion of chiral domain walls (Kim, Takei, and Tserkovnyak, 2015). The relevant temperature scale for this is set by the total energy of an individual domain wall  $\mathcal{A}\sqrt{A\kappa}$ , where  $\kappa \ll |K|$  is the parasitic anisotropy and  $\mathcal{A}$  is the geometric cross section of the wire.

Injection and detection of such superfluid spin currents in easy-plane antiferromagnets was proposed by Takei *et al.* (2014) using the direct and inverse spin Hall effects at interfaces with heavy metals. This is enabled by a spin-mixing conductance  $g^{\uparrow\downarrow}$  associated with the Néel order, which is finite even in the case of a compensated magnetization at the interface (Jia *et al.*, 2011; Cheng *et al.*, 2014; Takei *et al.*, 2014), thus allowing for an electronically induced interfacial spin torque  $\tau_m$ . In the spirit of our previous discussion (see Sec. II, regarding the smallness of  $\mathbf{m}$ ), it is sufficient here to retain only the spin torques and pumping associated with the rigid dynamics of the Néel order  $\mathbf{l}$  alone. Figure 47 shows a proposed detection of a spin superflow via a long-ranged negative electron drag that it mediates. Refined detection schemes have been discussed by Takei and Tserkovnyak (2015). Similar setups could be used also for experimental detection of thermal and quantum phase slips, as proposed by Kim, Takei, and Tserkovnyak (2016) and Kim and Tserkovnyak (2016). Furthermore, at finite temperatures, we may expect the collective spin and heat flows to be carried in a superfluid spin state by the coupled two-fluid dynamics, in close analogy with the ferromagnetic case (Flebus *et al.*, 2016).

To conclude this section, we note that, in contrast to what is observed in ferromagnets, spin superfluidity in antiferromagnets is unaffected by detrimental dipolar interactions (Skarsvåg, Holmqvist, and Brataas, 2015). The wealth of

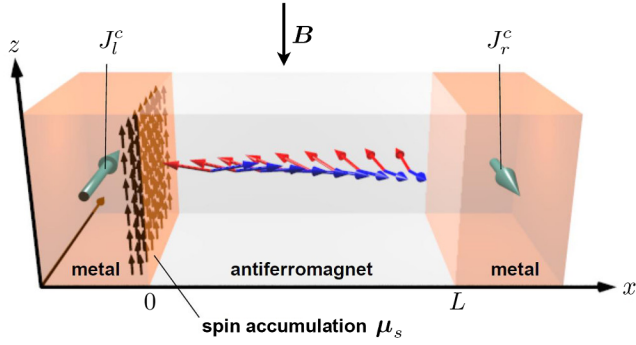


FIG. 47. Negative electron drag between two metals mediated by an antiferromagnetic spin superfluid. The left metal injects a spin current by producing the interfacial torque  $\tau_m = g^{\uparrow\downarrow} \mu_s / (4\pi)$ , which then propagates along the  $x$  axis according to Eq. (36).  $\mu_s$  is in the first place induced by the spin Hall effect associated with the electrical current  $J_l^c$  flowing in the  $y$  direction. The spin-current detection by the right metal proceeds in the Onsager-reciprocal fashion: the Néel dynamics pump spin current [associated with the torque  $\tau_m = -g^{\uparrow\downarrow} \hbar \partial_t \varphi / (4\pi)$ ], which finally produces a detectable voltage by the inverse spin Hall effect. From Takei *et al.*, 2014.

insulating antiferromagnetic materials, particularly of the easy-plane character, bodes well for the search for a useful spin-superfluid medium. Furthermore, using the magnetic-field-induced antiferromagnetic spin-flop transition offers a practical tool to mitigate parasitic easy-axis anisotropies (Qaiumzadeh *et al.*, 2017).

### C. Thermally induced domain-wall motion

The interplay between spin waves, antiferromagnetic domain walls, and temperature gradient has been investigated in various ways. Tveten, Qaiumzadeh, and Brataas (2014) and Kim, Tserkovnyak, and Tchernyshyov (2014) addressed the motion of a uniaxial antiferromagnetic wall driven by magnons. They identified three main mechanisms responsible for driving domain-wall motion: transfer of angular momentum ( $=2\hbar$ ), reflection against the wall, and redshift of the magnon frequency corresponding to a net transfer of momentum (Kim, Tserkovnyak, and Tchernyshyov, 2014). When circularly polarized, the transfer of angular momentum causes the wall to precess away from the magnon source, resulting in reflection and redshift at high and low magnon intensities, respectively. With linear polarized magnons, no spin transfer occurs (both circularly polarized magnon states are equally populated) and instead a viscous force associated with magnon damping drags the wall toward the magnon source (Tveten, Qaiumzadeh, and Brataas, 2014).

Using the collective coordinate approach presented in Sec. II, Kim, Tchernyshyov, and Tserkovnyak (2015) demonstrated that domain-wall and other stochastic solitonic dynamics under the influence of thermal random forces exhibit Brownian thermophoresis. This effect tends to induce a mean drift toward colder regions as illustrated in Fig. 48.

Indeed, averaging Eq. (30) over an ensemble of solitons undergoing stochastic Brownian motion leads to the Fokker-Planck equation in the form of a continuity relation:

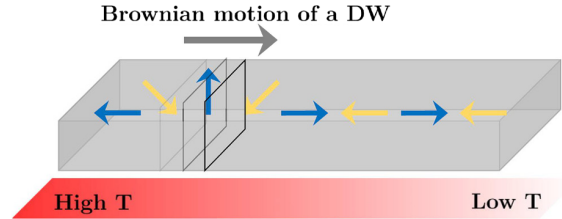


FIG. 48. Stochastic thermal forces associated with an inhomogeneous temperature profile push an antiferromagnetic domain wall to a colder region. From Kim, Tchernyshyov, and Tserkovnyak, 2015.

$$\partial_t \rho + \nabla \cdot \mathbf{j} = 0, \quad (43)$$

where  $\rho$  is the soliton density and  $\mathbf{j}$  their net flux. The latter is given by (Kim, Tchernyshyov, and Tserkovnyak, 2015)

$$\mathbf{j} = \mu \rho (\mathbf{F} - k_B \nabla T) - D \nabla \rho. \quad (44)$$

The average velocity of (a uniform ensemble of) skyrmions subjected to a constant force and thermal gradient is thus

$$\mathbf{v} = \mu (\mathbf{F} - k_B \nabla T), \quad (45)$$

which shows the tendency to drift toward the colder regions where the solitons are less agitated and their Brownian motion freezes. This thermophoretic torque competes with thermomagnonic torques ( $\sim \mathbf{F}$ ), whose entropic component pushes the localized magnetic textures toward hotter regions (Kim and Tserkovnyak, 2015a). In the special case of a one-dimensional domain-wall motion in an easy-axis antiferromagnet (Kim, Tchernyshyov, and Tserkovnyak, 2015), the mobility is given by  $\mu = \lambda_{dw}/2$ , where  $\lambda_{dw} \equiv \sqrt{A/K}$  is the domain-wall width. The dissipation of energy associated with a steady rigid domain-wall motion is  $P = \dot{R} \cdot F = \dot{R}^2 / \mu$ . Since for the ferromagnetic dynamics, according to the Landau-Lifshitz-Gilbert phenomenology, the Rayleigh function associated with the (directional) magnetic order parameter  $\mathbf{m}$  (constrained by  $|\mathbf{m}| \equiv 1$ ) coincides with that of the antiferromagnetic  $\mathbf{l}$  (with  $|\mathbf{l}| \equiv 1$ ), the expression for the mobility remains (with  $\alpha$  being the usual ferromagnetic Gilbert damping). When the physical cross section of the magnetic wire increases and the mobility  $\mu \propto A^{-1}$  decreases, eventually thermomagnonic torques (including spin transfer and entropic forces) start dominating, pushing domain walls generally toward the hotter side (Kim and Tserkovnyak, 2015b), in the presence of a thermal gradient  $\nabla T$ .

Stochastic motion of topological solitons is qualitatively different (and faster) in antiferromagnets compared to ferromagnets in two dimensions, due to the absence of the gyrotoprotic Magnus force in the former, as discussed in Sec. II.A.3 (Schütte *et al.*, 2014; Kim, Tchernyshyov, and Tserkovnyak, 2015; Barker and Tretiakov, 2016). Finally, Selzer *et al.* (2016) investigated the motion of antiferromagnetic domain walls in response to thermal gradients using an atomistic model. Similar to Shiino *et al.* (2016) and Gomonay, Jungwirth, and Sinova (2016), they obtained massless motion of the domain wall due to the absence of azimuthal tilting during the motion.

## V. CONCLUSION AND PERSPECTIVES

Up until recently limited to a passive role in spintronic devices, antiferromagnetic materials could represent the future of spintronic applications. The recent experimental achievements (spin pumping, spin-orbit torque, anisotropic magnetoresistance, anomalous Hall effect, spin Seebeck effect, etc.) bear the promises for future outstanding developments. The wide diversity under which antiferromagnetism appears in nature (from metals to insulators, not to mention the vast richness of magnetic textures) offers a fascinating playground for physicists, materials scientists, and engineers.

Nonetheless, significant challenges still need to be thoroughly addressed before antiferromagnets can become active elements of real spintronic devices. First and foremost, collecting systematic and reproducible data represent a major difficulty due to significant sample-to-sample variability and uncontrolled size effects. Since the magnetic texture of antiferromagnets is greatly sensitive to the layer thickness, temperature, and growth conditions, the impact of the magnetic order (compensated versus uncompensated interfaces, collinear versus noncollinear texture, etc.) on the spin transport properties remains to be accurately understood. To this end, the development of new characterization techniques, ranging from optical imaging to THz methods (Urs *et al.*, 2016), will be a seminal milestone in order to overcome the difficulties faced by generations of researchers working on antiferromagnetic materials.

A particularly thrilling aspect of antiferromagnetic materials is their wide variety in nature. The growth of novel materials with high spin polarization and low damping will also be an important step (Hu, 2012; Sahoo *et al.*, 2016). A recent striking and stimulating example of how two fields of condensed matter physics may envision a common future is the prediction that Dirac quasiparticles [with the example of Dirac quasiparticles in the CuMnAs semimetal (Tang *et al.*, 2016)] can be controlled by spin-orbit torque reorientation of the Néel vector in an antiferromagnet (Šmejkal *et al.*, 2017). In a more long-term vision, we can also imagine capitalizing on the broad knowledge acquired by decades of fundamental research conducted on strongly correlated antiferromagnets (Georges, de' Medici, and Mravlje, 2013; Behrmann and Lechermann, 2015) and high- $T_c$  superconductors (Scalapino, 2012), where the intermingling between spin transport and antiferromagnetic order requires deeper investigation. Emerging materials with strong spin-orbit coupling such as antiferromagnetic topological insulators (Mong, Essin, and Moore, 2010; Bansil, Lin, and Das, 2016) or Weyl semimetals (Wan *et al.*, 2011) could also be an inspiring research direction in the near future (Šmejkal, Jungwirth, and Sinova, 2017).

## ACKNOWLEDGMENTS

We acknowledge all the colleagues who contributed by publishing the results shown in this review. We thank all our colleagues from our respective laboratories and within the scientific community for stimulating discussions and for motivating our curiosity and interest in this topic and for useful comments on the manuscript, in particular: T. Jungwirth, J. Sinova, J. Wunderlich, O. Gomonay, X. Marti, A. Hoffmann,

S. Maekawa, A. Brataas, W. E. Bailey, M. Chshiev, H. Béa, A. Schuhl, G. Gaudin, M. Miron, O. Boulle, S. Auffret, O. Klein, D. Givord, A. Mougin, A. Bataille, L. Ranno, M. Viret, H. Saidaoui, C. Akosa, P. Merodio, L. Frangou, G. Forestier, O. Gladii, P. Wadley, F. Lechermann, J. Linder, R. Cheng, W. Lin, A. Sekine, and J. Heremans. We thank M. Gallagher-Gambarelli for a critical reading of the manuscript. V.B. acknowledges the financial support of the French National Agency for Research (Grant No. ANR-15-CE24-0015-01). A.M., V.B., and M.T. acknowledge the financial support of the King Abdullah University of Science and Technology (KAUST) through the Office of Sponsored Research (OSR) (Grant No. OSR-2015-CRG4-2626). M.T. acknowledges the financial support of C-SPIN, one of six centers of STARnet, a Semiconductor Research Corporation program, sponsored by MARCO and DARPA, and by the NSF (Grant No. DMR-1207577). T.M. and T.O. were supported by the Japan Society for the Promotion of Science KAKENHI (Grants No. 26870300 and No. 15H05702), and the Grant-in-Aid for Scientific Research on Innovative Area, "Nano Spin Conversion Science" (Grant No. 26103002). Y.T. acknowledges the financial support of the ARO (Contract No. 911NF-14-1-0016) and the NSF-funded MRSEC (Grant No. DMR-1420451).

## REFERENCES

- Abarra, E., K. Takano, F. Hellman, and A. Berkowitz, 1996, "Thermodynamic Measurements of Magnetic Ordering in Antiferromagnetic Superlattices," *Phys. Rev. Lett.* **77**, 3451.
- Acharyya, R., H. Y. T. Nguyen, W. P. Pratt, and J. Bass, 2010, "Spin-Flipping Associated With the Antiferromagnet IrMn," *IEEE Trans. Magn.* **46**, 1454.
- Acharyya, R., H. Y. T. Nguyen, W. P. Pratt, and J. Bass, 2011, "A Study of Spin-flipping in Sputtered IrMn Using Py-Based Exchange-Biased Spin-Valves," *J. Appl. Phys.* **109**, 07C503.
- Akmalidinov, K., C. Ducruet, C. Portemont, I. Joumard, I. L. Prejbeanu, B. Dieny, and V. Baltz, 2014, "Mixing Antiferromagnets to Tune NiFe-[IrMn/FeMn] Interfacial Spin-Glasses, Grains Thermal Stability and Related Exchange Bias Properties," *J. Appl. Phys.* **115**, 17B718.
- Akmalidinov, K., L. Frangou, C. Ducruet, C. Portemont, J. Pereira, I. Joumard, B. Dieny, J. Alvarez-Héroult, and V. Baltz, 2015, "Disordered Magnetic Phases Located over Ferromagnetic/antiferromagnetic Films Impact on Cell-to-Cell Variability of Exchange Bias in Thermally-Assisted MRAM Chips," *IEEE Magn. Lett.* **6**, 3000404.
- Allwood, D. A., G. Xiong, C. C. Faulkner, D. Atkinson, D. Petit, and R. P. Cowburn, 2005, "Magnetic Domain-Wall Logic," *Science* **309**, 1688.
- Ambrose, T., and C. L. Chien, 1996, "Finite-Size Effects and Uncompensated Magnetization in Thin Antiferromagnetic CoO Layers," *Phys. Rev. Lett.* **76**, 1743.
- Anderson, P. W., 1959, "New Approach to the Theory of Superexchange Interactions," *Phys. Rev.* **115**, 2.
- Ando, K., 2014, "Dynamical Generation of Spin Currents," *Semicond. Sci. Technol.* **29**, 043002.
- Ando, K., S. Takahashi, K. Harii, K. Sasage, J. Ieda, S. Maekawa, and E. Saitoh, 2008, "Electric Manipulation of Spin Relaxation Using the Spin Hall Effect," *Phys. Rev. Lett.* **101**, 036601.
- Auerbach, A., 1994, *Interacting Electrons and Quantum Magnetism* (Springer-Verlag, New York).

- Balents, L., 2010, “Spin Liquids in Frustrated Magnets,” *Nature (London)* **464**, 199.
- Baltz, V., G. Gaudin, P. Somani, and B. Dieny, 2010, “Influence of Edges on the Exchange Bias Properties of Ferromagnetic/antiferromagnetic Nanodots,” *Appl. Phys. Lett.* **96**, 262505.
- Baltz, V., B. Rodmacq, A. Zarefy, L. Lechevallier, and B. Dieny, 2010, “Bimodal Distribution of Blocking Temperature in Exchange-Biased Ferromagnetic/antiferromagnetic Bilayers,” *Phys. Rev. B* **81**, 052404.
- Baltz, V., J. Sort, S. Landis, B. Rodmacq, and B. Dieny, 2005, “Tailoring Size Effects on the Exchange Bias in Ferromagnetic-Antiferromagnetic < 100 Nm Nanostructures,” *Phys. Rev. Lett.* **94**, 117201.
- Baltz, V., J. Sort, B. Rodmacq, B. Dieny, and S. Landis, 2004, “Size Effects on Exchange Bias in Sub-100 Nm Ferromagnetic-antiferromagnetic Dots Deposited on Prepatterned Substrates,” *Appl. Phys. Lett.* **84**, 4923.
- Bansil, A., H. Lin, and T. Das, 2016, “Colloquium: Topological Band Theory,” *Rev. Mod. Phys.* **88**, 021004.
- Barker, J., and O. A. Tretiakov, 2016, “Static and Dynamical Properties of Antiferromagnetic Skyrmions in the Presence of Applied Current and Temperature,” *Phys. Rev. Lett.* **116**, 147203.
- Barthem, V. M. T. S., C. V. Colin, H. Mayaffre, M.-H. Julien, and D. Givord, 2013, “Revealing the Properties of Mn2Au for Antiferromagnetic Spintronics,” *Nat. Commun.* **4**, 2892.
- Bar'yakhtar, I. V., and B. A. Lvanov, 1983, “Dynamic Solitons in a Uniaxial Antiferromagnet,” *Zh. Eksp. Teor. Fiz.* **85**, 328 [*JETP* **58**, 190 (1983)].
- Bass, J., and W. P. Pratt, 2007, “Spin-Diffusion Lengths in Metals and Alloys, and Spin-Flipping at Metal/metal Interfaces: An Experimentalist’s Critical Review,” *J. Phys. Condens. Matter* **19**, 183201.
- Basset, J., A. Sharma, Z. Wei, J. Bass, and M. Tsoi, 2008, “Towards Antiferromagnetic Metal Spintronics,” in *Society of Photo-Optical Instrumentation Engineers (SPIE)*, edited by Manijeh Razeghi, Henri-Jean M. Drouhin, and Jean-Eric Wegrowe (SPIE—International Society for Optical Engineering, Bellingham, WA), Vol. 7036, p. 3605.
- Bauer, G. E. W., E. Saitoh, and B. J. van Wees, 2012, “Spin Caloritronics,” *Nat. Mater.* **11**, 391.
- Bauer, G. E. W., and Y. Tserkovnyak, 2011, “Spin-Magnon Transmutation,” *Physics* **4**, 40.
- Behrmann, M., and F. Lechermann, 2015, “Large-Amplitude Spin Oscillations Triggered by Nonequilibrium Strongly Correlated  $t_2g$  Electrons,” *Phys. Rev. B* **91**, 075110.
- Belov, K. P., and V. I. Sokolov, 1977, “Antiferromagnetic Garnets,” *Sov. Phys. Usp.* **20**, 149.
- Bender, S. A., R. A. Duine, A. Brataas, and Y. Tserkovnyak, 2014, “Dynamic Phase Diagram of Dc-Pumped Magnon Condensates,” *Phys. Rev. B* **90**, 094409.
- Bender, S. A., R. A. Duine, and Y. Tserkovnyak, 2012, “Electronic Pumping of Quasiequilibrium Bose-Einstein-Condensed Magnons,” *Phys. Rev. Lett.* **108**, 246601.
- Bender, S. A., and Y. Tserkovnyak, 2015, “Interfacial Spin and Heat Transfer between Metals and Magnetic Insulators,” *Phys. Rev. B* **91**, 140402.
- Berger, L., 1996, “Emission of Spin Waves by a Magnetic Multilayer Traversed by a Current,” *Phys. Rev. B* **54**, 9353.
- Berkowitz, A. E., and K. Takano, 1999, “Exchange Anisotropy— a Review,” *J. Magn. Magn. Mater.* **200**, 552.
- Bernevig, B. A., and O. Vafek, 2005, “Piezo-Magnetoelectric Effects in P-Doped Semiconductors,” *Phys. Rev. B* **72**, 033203.
- Binek, C., and B. Doudin, 2005, “Magnetoelectronics with Magnetoelectrics,” *J. Phys. Condens. Matter* **17**, L39.
- Bitter, F., 1938, “A Generalization of the Theory of Ferromagnetism,” *Phys. Rev.* **54**, 79.
- Bizette, H., C. F. Squire, and B. Tsai, 1938, “Le Point de Transition Lambda de La Susceptibilité Magnétique Du Protoxyde de Manganèse,” *C. Acad. Sci. Paris* **207**, 449 [<http://gallica.bnf.fr/ark:/12148/bpt6k31590/f449.image>].
- Blazey, K. W., and H. Rohrer, 1968, “Antiferromagnetism and the Magnetic Phase Diagram of GdAl<sub>103</sub>,” *Phys. Rev. B* **173**, 574.
- Boakye, F., and G. Adanu, 1996, “The Néel Temperature of Alpha-Mn Thin Films,” *Thin Solid Films* **279**, 29.
- Bode, M., E. Y. Vedmedenko, K. von Bergmann, A. Kubetzka, P. Ferriani, S. Heinze, and R. Wiesendanger, 2006, “Atomic Spin Structure of Antiferromagnetic Domain Walls,” *Nat. Mater.* **5**, 477.
- Bodnar S. Yu., L. Smejkal, I. Turek, T. Jungwirth, O. Gomonay, J. Sinova, A. A. Sapozhnik, H.-J. Elmers, M. Klau, and M. Jourdan, 2017, “Writing and Reading antiferromagnetic Mn<sub>2</sub>Au: Néel spin-orbit torques and large anisotropic magnetoresistance,” *arXiv: 1706.02482v1*.
- Boona, S. R., R. C. Myers, and J. P. Heremans, 2014, “Spin Caloritronics,” *Energy Environ. Sci.* **7**, 885.
- Bossini, D., A. M. Alashnikova, R. V. Pisarev, Th. Rasing, and A. V. Kimel, 2015, “Ultrafast Opto-Magnetism in KNiF<sub>3</sub>,” *Ultrafast Magn. I. Springer Proc. Physics* (Springer, New York), Vol. 159, p. 221.
- Brasse, M., L. Chioncel, J. Kuneš, A. Bauer, A. Regnat, C. G. F. Blum, S. Wurmehl, C. Pfleiderer, M. A. Wilde, and D. Grundler, 2013, “De Haas-van Alphen Effect and Fermi Surface Properties of Single-Crystal CrB<sub>2</sub>,” *Phys. Rev. B* **88**, 155138.
- Brataas, A., G. E. W. Bauer, and P. J. Kelly, 2006, “Non-Collinear Magnetoelectronics,” *Phys. Rep.* **427**, 157.
- Brataas, A., and K. M. D. Hals, 2014, “Spin-orbit Torques in Action,” *Nat. Nanotechnol.* **9**, 86.
- Brataas, A., A. D. Kent, and H. Ohno, 2012, “Current-Induced Torques in Magnetic Materials,” *Nat. Mater.* **11**, 372.
- Brataas, A., Y. Tserkovnyak, and G. E. W. Bauer, 2006, “Current-Induced Macrospin versus Spin-Wave Excitations in Spin Valves,” *Phys. Rev. B* **73**, 014408.
- Brataas, A., Y. Tserkovnyak, G. E. W. Bauer, and P. J. Kelly, 2012, “Spin Currents,” Book Title, edited by S. Maekawa, S. O. Val, E. Saitoh, and T. Kimura (Oxford University Press, Oxford), 87.
- Brink, A. V. D., G. Vermijs, A. Solognac, J. Koo, J. T. Kohlhepp, H. J. M. Swagten, and B. Koopmans, 2016, “Field-Free Magnetization Reversal by Spin-Hall Effect and Exchange Bias,” *Nat. Commun.* **7**, 10854.
- Brück, S., J. Sort, V. Baltz, S. Suriñach, J. S. Muñoz, B. Dieny, M. D. Baró, and J. Nogués, 2005, “Exploiting Length Scales of Exchange-Bias Systems to Fully Tailor Double-Shifted Hysteresis Loops,” *Adv. Mater.* **17**, 2978.
- Chen, H., Q. Niu, and A. H. MacDonald, 2014, “Anomalous Hall Effect Arising from Noncollinear Antiferromagnetism,” *Phys. Rev. Lett.* **112**, 017205.
- Chen, K., W. Lin, C. L. Chien, and S. Zhang, 2016, “Temperature Dependence of Angular Momentum Transport Across Interfaces,” *Phys. Rev. B* **94**, 054413.
- Chen, Y.-T., S. Takahashi, H. Nakayama, M. Althammer, S. Goennenwein, E. Saitoh, and G. E. W. Bauer, 2013, “Theory of Spin Hall Magnetoresistance,” *Phys. Rev. B* **87**, 144411.
- Cheng, R., M. W. Daniels, J.-G. Zhu, and D. Xiao, 2015, “Ultrafast Switching of Antiferromagnets via Spin-Transfer Torque,” *Phys. Rev. B* **91**, 064423.



- Cheng, R., and Q. Niu, 2014, “Dynamics of Antiferromagnets Driven by Spin Current,” *Phys. Rev. B* **89**, 081105.
- Cheng, R., S. Okamoto, and D. Xiao, 2016, “Spin Nernst Effect of Magnons in Collinear Antiferromagnets,” *Phys. Rev. Lett.* **117**, 217202.
- Cheng, R., D. Xiao, and A. Brataas, 2016, “Terahertz Antiferromagnetic Spin Hall Nano-Oscillator,” *Phys. Rev. Lett.* **116**, 207603.
- Cheng, R., J. Xiao, Q. Niu, and A. Brataas, 2014, “Spin Pumping and Spin-Transfer Torques in Antiferromagnets,” *Phys. Rev. Lett.* **113**, 057601.
- Cheng, R., J.-G. Zhu, and D. Xiao, 2016, “Dynamic Feedback in Ferromagnet/Spin-Hall Heterostructures,” *Phys. Rev. Lett.* **117**, 097202.
- Chernyshov, A., M. Overby, X. Liu, J. K. Furdyna, Y. Lyanda-Geller, and L. P. Rokhinson, 2009, “Evidence for Reversible Control of Magnetization in a Ferromagnetic Material by Means of Spin-orbit Magnetic Field,” *Nat. Phys.* **5**, 656.
- Chumak, A. V., Al. D. Karenowska, A. A. Serga, and B. Hillebrands, 2015, “Magnon Spintronics,” *Nat. Phys.* **11**, 453.
- Ciccarelli, C., *et al.*, 2016, “Room-Temperature Spin-Orbit Torque in NiMnSb,” *Nat. Phys.* **12**, 855.
- Clarkson, J., *et al.*, 2017, “Hidden Magnetic States Emergent Under Electric Field, In A Room Temperature Composite Magnetoelectric Multiferroic,” *Sci. Rep.* **7**, 15460.
- Coey, J. M. D., 2009, *Magnetism and Magnetic Materials* (Cambridge University Press, Cambridge, England).
- Coldea, R., S. M. Hayden, G. Aeppli, T. G. Perring, C. D. Frost, T. E. Mason, S.-W. Cheong, and Z. Fisk, 2001, “Spin Waves and Electronic Interactions in La<sub>2</sub>CuO<sub>4</sub>,” *Phys. Rev. Lett.* **86**, 5377.
- Cornelissen, L. J., J. Liu, R. A. Duine, J. Ben Youssef, and B. J. Van Wees, 2015, “Long Distance Transport of Magnon Spin Information in a Magnetic Insulator at Room Temperature,” *Nat. Phys.* **11**, 1022.
- Cubukcu, M., O. Boulle, M. Drouard, K. Garello, C. O. Avci, I. M. Miron, J. Langer, B. Ocker, P. Gambardella, and G. Gaudin, 2014, “Spin-Orbit Torque Magnetization Switching of a Three-Terminal Perpendicular Magnetic Tunnel Junction,” *Appl. Phys. Lett.* **104**, 042406.
- Dai, N., N. Thuan, L. Hong, N. Phuc, Y. Lee, S. Wolf, and D. Nam, 2008, “Impact of in-Plane Currents on Magnetoresistance Properties of an Exchange-Biased Spin Valve with an Insulating Antiferromagnetic Layer,” *Phys. Rev. B* **77**, 132406.
- Dai, P., 2015, “Antiferromagnetic Order and Spin Dynamics in Iron-Based Superconductors,” *Rev. Mod. Phys.* **87**, 855.
- Daniels, M. W., W. Guo, G. M. Stocks, D. Xiao, and J. Xiao, 2015, “Spin-Transfer Torque Induced Spin Waves in Antiferromagnetic Insulators,” *New J. Phys.* **17**, 103039.
- Dassonneville, B., R. Acharyya, H. Y. T. Nguyen, R. Loloee, W. P. Pratt, and J. Bass, 2010, “A Way to Measure Electron Spin-Flipping at Ferromagnetic/nonmagnetic Interfaces and Application to Co/Cu,” *Appl. Phys. Lett.* **96**, 022509.
- De Jong, J. A., A. V. Kimel, R. V. Pisarev, A. Kirilyuk, and Th. Rasing, 2011, “Laser-Induced Ultrafast Spin Dynamics in ErFeO<sub>3</sub>,” *Phys. Rev. B* **84**, 104421.
- De Ranieri, E., *et al.*, 2008, “Lithographically and Electrically Controlled Strain Effects on Anisotropic Magnetoresistance in (Ga, Mn)As,” *New J. Phys.* **10**, 065003.
- Dieny, B., V. S. Speriosu, and S. S. P. Parkin, 1991, “Giant Magnetoresistive in Soft Ferromagnetic Multilayers,” *Phys. Rev. B* **43**, 1297.
- Du, C., H. Wang, F. Yang, and P. C. Hammel, 2014a, “Systematic Variation of Spin-Orbit Coupling with D-Orbital Filling: Large Inverse Spin Hall Effect in 3d Transition Metals,” *Phys. Rev. B* **90**, 140407.
- Du, C., H. Wang, F. Yang, and P. C. Hammel, 2014b, “Enhancement of Pure Spin Currents in Spin Pumping Y<sub>3</sub>Fe<sub>5</sub>O<sub>12</sub>/Cu/Metal Trilayers through Spin Conductance Matching,” *Phys. Rev. Applied* **1**, 044004.
- Duine, R. A., 2011, “Spintronics: An Alternating Alternative,” *Nat. Mater.* **10**, 344.
- Duine, R. A., P. M. Haney, A. S. Nunez, and A. H. MacDonald, 2007, “Inelastic Scattering in Ferromagnetic and Antiferromagnetic Metal Spintronics,” *Phys. Rev. B* **75**, 014433.
- Dyakonov, M. I., 2010, “Spin Hall Effect,” in *Future Trends in Microelectronics*, edited by S. Luryi, J. Xu, and A. Zaslavsky (Wiley, New York), p. 251.
- Dzyaloshinskii, I., 1958, “Thermodynamic Theory of ‘Weak’ Ferromagnetism of Antiferromagnetics,” *J. Phys. Chem. Solids* **4**, 241.
- Emori, S., U. Bauer, S.-M. Ahn, E. Martinez, and G. S. D. Beach, 2013, “Current-Driven Dynamics of Chiral Ferromagnetic Domain Walls,” *Nat. Mater.* **12**, 611.
- Esmailzadeh, S., U. Hålenius, and M. Valldor, 2006, “Crystal Growth, Magnetic, and Optical Properties of the Ternary Nitride MnSiN<sub>2</sub>,” *Chem. Mater.* **18**, 2713.
- Fang, D., H. Kurebayashi, J. Wunderlich, K. Výborný, L. P. Zárbo, R. P. Campion, A. Casiraghi, B. L. Gallagher, T. Jungwirth, and a. J. Ferguson, 2011, “Spin-orbit-Driven Ferromagnetic Resonance,” *Nat. Nanotechnol.* **6**, 413.
- Fawcett, E., 1988, “Spin-Density-Wave Antiferromagnetism in Chromium,” *Rev. Mod. Phys.* **60**, 209.
- Fert, A., V. Cros, and J. Sampaio, 2013, “Skyrmions on the Track,” *Nat. Nanotechnol.* **8**, 152.
- Fert, A., and P. M. Levy, 1980, “Role of Anisotropic Exchange Interactions in Determining the Properties of Spin-Glasses,” *Phys. Rev. Lett.* **44**, 1538.
- Fert, A., N. Reyren, and V. Cros, 2017, “Magnetic Skyrmions: Advances in Physics and Potential Applications,” *Nat. Rev. Mater.* **2**, 17031.
- Fiebig, M., N. P. Duong, and T. Satoh, 2004, “Ultrafast Manipulation of Antiferromagnetism in NiO,” *Phys. Rev. Lett.* **93**, 117402.
- Fina, I., and X. Marti, 2017, “Electric Control of Antiferromagnets,” *IEEE Trans. Magn.* **53**, 2500107.
- Fina, I., *et al.*, 2014, “Anisotropic Magnetoresistance in an Antiferromagnetic Semiconductor,” *Nat. Commun.* **5**, 4671.
- Flebus, B., S. A. Bender, Y. Tserkovnyak, and A. Duine, 2016, “Two-Fluid Theory for Spin Superfluidity in Magnetic Insulators,” *Phys. Rev. Lett.* **116**, 117201.
- Frangou, L., G. Forestier, S. Auffret, S. Gambarelli, and V. Baltz, 2017, “Relaxation Mechanism in NiFe Thin Films Driven by Spin Angular Momentum Absorption throughout the Antiferromagnetic Phase Transition in Native Surface Oxides,” *Phys. Rev. B* **95**, 054416.
- Frangou, L., S. Oyarzun, S. Auffret, L. Vila, S. Gambarelli, and V. Baltz, 2016, “Enhanced Spin Pumping Efficiency in Antiferromagnetic IrMn Thin Films around the Magnetic Phase Transition,” *Phys. Rev. Lett.* **116**, 077203.
- Fukami, S., C. Zhang, S. DuttaGupta, A. Kurenkov, and H. Ohno, 2016, “Magnetization Switching by Spin-Orbit Torque in an Antiferromagnet/ferromagnet Bilayer System,” *Nat. Mater.* **15**, 535.
- Galceran, R., *et al.*, 2016, “Isothermal Anisotropic Magnetoresistance in Antiferromagnetic Metallic IrMn,” *Sci. Rep.* **6**, 35471.
- Gambardella, P., and I. M. Miron, 2011, “Current-Induced Spin-Orbit Torques,” *Philos. Trans. R. Soc. London* **369**, 3175.
- Garate, I., and A. H. MacDonald, 2009, “Influence of a Transport Current on Magnetic Anisotropy in Gyrotropic Ferromagnets,” *Phys. Rev. B* **80**, 134403.

- Garello, K., *et al.*, 2014, “Ultrafast magnetization switching by spin-orbit torques,” *Appl. Phys. Lett.* **105**, 212402.
- Georges, A., L. de’ Medici, and J. Mravlje, 2013, “Strong Correlations from Hund’s Coupling,” *Annu. Rev. Condens. Matter Phys.* **4**, 137.
- Ghosh, A., S. Auffret, U. Ebels, and W. E. Bailey, 2012, “Penetration Depth of Transverse Spin Current in Ultrathin Ferromagnets,” *Phys. Rev. Lett.* **109**, 127202.
- Giamarchi, T., 2003, *Quantum Physics in One Dimension* (Oxford University Press, Oxford).
- Giamarchi, T., Ch. Rüegg, and O. Tchernyshyov, 2008, “Bose-Einstein Condensation in Magnetic Insulators,” *Nat. Phys.* **4**, 198.
- Göbel, G., A. Mook, J. Henk, and I. Mertig, 2017, “Antiferromagnetic Skyrmion Crystals: Generation, Topological Hall and Topological Spin Hall Effect,” *Phys. Rev. B* **96**, 060406(R).
- Gomonay, H. V., R. V. Kunitsyn, and V. M. Loktev, 2012, “Symmetry and the Macroscopic Dynamics of Antiferromagnetic Materials in the Presence of Spin-Polarized Current,” *Phys. Rev. B* **85**, 134446.
- Gomonay, H. V., and V. M. Loktev, 2010, “Spin Transfer and Current-Induced Switching in Antiferromagnets,” *Phys. Rev. B* **81**, 144427.
- Gomonay, H. V., and V. M. Loktev, 2014, “Spintronics of Antiferromagnetic Systems,” *Low Temp. Phys.* **40**, 17.
- Gomonay, O., T. Jungwirth, and J. Sinova, 2016, “Staggering Antiferromagnetic Domain Wall Velocity in a Staggered Spin-Orbit Field,” *Phys. Rev. Lett.* **117**, 017202.
- Gomonay, O., M. Klaui, and J. Sinova, 2016, “Manipulating Antiferromagnets with Magnetic Fields: Ratchet Motion of Multiple Domain Walls Induced by Asymmetric Field Pulses,” *Appl. Phys. Lett.* **109**, 142404.
- Gould, C., C. Rüster, T. Jungwirth, E. Girgis, G. Schott, R. Giraud, K. Brunner, G. Schmidt, and L. Molenkamp, 2004, “Tunneling Anisotropic Magnetoresistance: A Spin-Valve-Like Tunnel Magnetoresistance Using a Single Magnetic Layer,” *Phys. Rev. Lett.* **93**, 117203.
- Gross, I., *et al.*, 2017, “Real-Space Imaging of Non-Collinear Antiferromagnetic Order with a Single Spin Magnetometer,” unpublished.
- Grzybowski, M. J., *et al.*, 2017, “Imaging Current-Induced Switching of Antiferromagnetic Domains in CuMnAs,” *Phys. Rev. Lett.* **118**, 057701.
- Hagiwara, M., K. Katsumata, H. Yamaguchi, M. Tokunaga, I. Yamada, M. Gross, and P. Goy, 1999, “A Complete Frequency-Field Diagram for the Antiferromagnetic Resonance in MnF<sub>2</sub>,” *Int. J. Infrared Millimeter Waves* **20**, 617.
- Hahn, C., G. De Loubens, V. V. Naletov, J. Ben Youssef, O. Klein, and M. Viret, 2014, “Conduction of Spin Currents through Insulating Oxides,” *Europhys. Lett.* **108**, 57005.
- Hajiri, T., M. Matsushita, Y. Z. Ni, and H. Asano, 2017, “Impact of Anisotropy on Antiferromagnet Rotation in Heusler-Type Ferromagnet / Antiferromagnet Epitaxial Bilayers,” *Phys. Rev. B* **95**, 134413.
- Haldane, F. D. M., 1983, “Nonlinear Field Theory of Large-Spin Heisenberg Antiferromagnets: Semiclassically Quantized Solitons of the One-Dimensional Easy-Axis Néel State,” *Phys. Rev. Lett.* **50**, 1153.
- Hals, K. M. D., Y. Tserkovnyak, and A. Brataas, 2011, “Phenomenology of Current-Induced Dynamics in Antiferromagnets,” *Phys. Rev. Lett.* **106**, 107206.
- Han, G. C., J. J. Qiu, Q. J. Yap, P. Luo, D. E. Laughlin, J. G. Zhu, T. Kanbe, and T. Shige, 2013, “Magnetic Stability of Ultrathin FeRh Films,” *J. Appl. Phys.* **113**, 17C107.
- Han, J., Y. Wang, F. Pan, and C. Song, 2016, “Spin-Hall-Effect-Assisted Electroresistance in Antiferromagnets via 105 A/cm<sup>2</sup> Dc Current,” *Sci. Rep.* **6**, 31966.
- Han, J. H., C. Song, F. Li, Y. Y. Wang, G. Y. Wang, Q. H. Yang, and F. Pan, 2014, “Antiferromagnet-Controlled Spin Current Transport in SrMnO<sub>3</sub>/Pt Hybrids,” *Phys. Rev. B* **90**, 144431.
- Han, T.-H., J. S. Helton, S. Chu, D. G. Nocera, J. A. Rodriguez-Rivera, C. Broholm, and Y. S. Lee, 2012, “Fractionalized Excitations in the Spin-Liquid State of a Kagome-Lattice Antiferromagnet,” *Nature (London)* **492**, 406.
- Haney, P. M., R. A. Duine, A. S. Núñez, and A. H. MacDonald, 2008, “Current-Induced Torques in Magnetic Metals: Beyond Spin-Transfer,” *J. Magn. Magn. Mater.* **320**, 1300.
- Haney, P. M., H. W. Lee, K. J. Lee, A. Manchon, and M. D. Stiles, 2013, “Current Induced Torques and Interfacial Spin-Orbit Coupling: Semiclassical Modeling,” *Phys. Rev. B* **87**, 174411.
- Haney, P. M., and A. H. MacDonald, 2008, “Current-Induced Torques Due to Compensated Antiferromagnets,” *Phys. Rev. Lett.* **100**, 196801.
- Haney, P. M., D. Waldron, R. A. Duine, A. S. Núñez, H. Guo, and A. H. MacDonald, 2007, “*Ab Initio* Giant Magnetoresistance and Current-Induced Torques in Cr/Au/Cr Multilayers,” *Phys. Rev. B* **75**, 174428.
- Hassdenteufel, A., B. Hebler, C. Schubert, A. Liebig, M. Teich, M. Helm, M. Aeschlimann, M. Albrecht, and R. Bratschitsch, 2013, “Thermally Assisted All-Optical Helicity Dependent Magnetic Switching in Amorphous Fe<sub>100-x</sub>Tbx Alloy Films,” *Adv. Mater.* **25**, 3122.
- He, X., Y. J. Wang, N. Wu, A. N. Caruso, E. Vescovo, K. D. Belashchenko, P. A. Dowben, and C. Binck, 2010, “Robust Isothermal Electric Control of Exchange Bias at Room Temperature,” *Nat. Mater.* **9**, 579.
- Hellman, F., *et al.*, 2017, “Interface-Induced Phenomena in Magnetism,” *Rev. Mod. Phys.* **89**, 025006.
- Higuchi, T., and M. Kuwata-Gonokami, 2016, “Control of Antiferromagnetic Domain Distribution via Polarization-Dependent Optical Annealing,” *Nat. Commun.* **7**, 10720.
- Hinze, D., and U. Nowak, 2011, “Domain Wall Motion by the Magnonic Spin Seebeck Effect,” *Phys. Rev. Lett.* **107**, 027205.
- Hirjibehedin, C. F., C. P. Lutz, and A. J. Heinrich, 2006, “Spin Coupling in Engineered Atomic Structures,” *Science* **312**, 1021.
- Hirobe, D., M. Sato, T. Kawamata, Y. Shiomi, K.-I. Uchida, R. Iguchi, Y. Koike, S. Maekawa, and E. Saitoh, 2016, “One-Dimensional Spinon Spin Currents,” *Nat. Phys.* **13**, 30.
- Hirschberger, M., S. K. Kushwaha, Z. Wang, Q. Gibson, S. Liang, C. A. Belvin, B. A. Bernevig, R. J. Cava, and N. P. Ong, 2016, “The Chiral Anomaly and Thermopower of Weyl Fermions in the Half-Heusler GdPtBi,” *Nat. Mater.* **15**, 1161.
- Hoffman, S., K. Sato, and Y. Tserkovnyak, 2013, “Landau-Lifshitz Theory of the Longitudinal Spin Seebeck Effect,” *Phys. Rev. B* **88**, 064408.
- Hoffmann, A., 2013, “Spin Hall Effects in Metals,” *IEEE Trans. Magn.* **49**, 5172.
- Hou, D., Z. Qiu, J. Barker, K. Sato, K. Yamamoto, and S. Velez, 2017, “Tunable Sign Change of Spin Hall Magnetoresistance in Pt/NiO/YIG Structures,” *Phys. Rev. Lett.*, to be published.
- Hu, X., 2012, “Half-Metallic Antiferromagnet as a Prospective Material for Spintronics,” *Adv. Mater.* **24**, 294.
- Hung, Y.-M., C. Hahn, H. Chang, M. Wu, H. Ohldag, and A. D. Kent, 2017, “Spin Transport in Antiferromagnetic NiO and Magnetoresistance in Y<sub>3</sub>Fe<sub>5</sub>O<sub>12</sub>/NiO/Pt Structures,” *AIP Adv.* **7**, 055903.
- Ivanov, B. A., 2014, “Spin Dynamics of Antiferromagnets under Action of Femtosecond Laser Pulses,” *Low Temp. Phys.* **40**, 91.
- Ivanov, B. A., and A. K. Kolezhuk, 1995, “Solitons in low-dimensional antiferromagnets,” *Fiz. Nizk. Temp.* **21**, 355 [*Low Temp. Phys.* **21**, 275 (1995)].

- Jaccarino, V., A. R. King, M. Motokawa, T. Sakakibara, and M. Date, 1983, "Temperature Dependence Of FeF<sub>2</sub> Spin Flop Field," *J. Magn. Magn. Mater.* **31–34**, 1117.
- Jacobs, I. S., 1961, "Spin-Flopping in MnF<sub>2</sub> by High Magnetic Fields," *J. Appl. Phys.* **32**, S61.
- Jacobs, I. S., and P. E. Lawrence, 1967, "Metamagnetic Phase Transition and Hysteresis in FeCl<sub>2</sub>," *Phys. Rev.* **164**, 866.
- Jia, X., K. Liu, K. Xia, and G. E. W. Bauer, 2011, "Spin Transfer Torque on Magnetic Insulators," *Europhys. Lett.* **96**, 17005.
- Johansen, Ö., and A. Brataas, 2017, "Spin Pumping and Inverse Spin Hall Voltages from Dynamical Antiferromagnets," *Phys. Rev. B* **95**, 220408(R).
- Johnston, D. C., 2012, "Magnetic Susceptibility of Collinear and Noncollinear Heisenberg Antiferromagnets," *Phys. Rev. Lett.* **109**, 077201.
- Ju, G., J. Hohlfeld, B. Bergman, R. J. M. Van Devedonk, O. N. Mryasov, J. Y. Kim, X. Wu, D. Weller, and B. Koopmans, 2004, "Ultrafast Generation of Ferromagnetic Order via a Laser-Induced Phase Transformation in FeRh Thin Films," *Phys. Rev. Lett.* **93**, 197403.
- Jungwirth, T., X. Marti, P. Wadley, and J. Wunderlich, 2016, "Antiferromagnetic Spintronics," *Nat. Nanotechnol.* **11**, 231.
- Kampfthath, T., A. Sell, G. Klatt, A. Pashkin, S. Mährlein, T. Dekorsy, M. Wolf, M. Fiebig, A. Leitenstorfer, and R. Huber, 2011, "Coherent Terahertz Control of Antiferromagnetic Spin Waves," *Nat. Photonics* **5**, 31.
- Kanazawa, N., Y. Onose, T. Arima, D. Okuyama, K. Ohoyama, S. Wakimoto, K. Kakurai, S. Ishiwata, and Y. Tokura, 2011, "Large Topological Hall Effect in a Short-Period Helimagnet MnGe," *Phys. Rev. Lett.* **106**, 156603.
- Kato, Y. K., R. C. Myers, A. C. Gossard, and D. D. Awschalom, 2004, "Observation of the Spin Hall Effect in Semiconductors," *Science* **306**, 1910.
- Kawaguchi, M., K. Shimamura, S. Fukami, F. Matsukura, H. Ohno, T. Moriyama, D. Chiba, and T. Ono, 2013, "Current-Induced Effective Fields Detected by Magnetotransport Measurements," *Appl. Phys. Express* **6**, 113002.
- Keffer, F., and C. Kittel, 1952, "Theory of Antiferromagnetic Resonance," *Phys. Rev.* **85**, 329.
- Khymyn, R., I. Lisenkov, V. S. Tiberkevich, A. N. Slavin, and B. A. Ivanov, 2016, "Transformation of Spin Current by Antiferromagnetic Insulators," *Phys. Rev. B* **93**, 224421.
- Kim, S. K., H. Ochoa, R. Zarzuela, and Y. Tserkovnyak, 2016, "Realization of the Haldane-Kane-Mele Model in a System of Localized Spins," *Phys. Rev. Lett.* **117**, 227201.
- Kim, S. K., S. Takei, and Y. Tserkovnyak, 2015, "Topological Spin Transport by Brownian Diffusion of Domain Walls," *Phys. Rev. B* **92**, 220409.
- Kim, S. K., S. Takei, and Y. Tserkovnyak, 2016, "Thermally-Activated Phase Slips in Superfluid Spin Transport in Magnetic Wires," *Phys. Rev. B* **93**, 020402(R).
- Kim, S. K., O. Tchernyshyov, and Y. Tserkovnyak, 2015, "Thermophoresis of an Antiferromagnetic Soliton," *Phys. Rev. B* **92**, 020402.
- Kim, S. K., and Y. Tserkovnyak, 2015, "Landau-Lifshitz Theory of Thermomagnonic Torque," *Phys. Rev. B* **92**, 020410.
- Kim, S. K., and Y. Tserkovnyak, 2016, "Topological Effects on Quantum Phase Slips in Superfluid Spin Transport," *Phys. Rev. Lett.* **116**, 127201.
- Kim, S. K., Y. Tserkovnyak, and O. Tchernyshyov, 2014, "Propulsion of a Domain Wall in an Antiferromagnet by Magnons," *Phys. Rev. B* **90**, 104406.
- Kimel, A. V., B. A. Ivanov, R. V. Pisarev, P. A. Usachev, A. Kirilyuk, and Th. Rasing, 2009, "Inertia-Driven Spin Switching in Antiferromagnets," *Nat. Phys.* **5**, 727.
- Kimel, A. V., A. Kirilyuk, A. Tsvetkov, R. V. Pisarev, and Th. Rasing, 2004, "Laser-Induced Ultrafast Spin Reorientation in the Antiferromagnet TmFeO<sub>3</sub>," *Nature (London)* **429**, 850.
- Kimel, A. V., A. Kirilyuk, P. A. Usachev, R. V. Pisarev, A. M. Balbashov, and Th. Rasing, 2005, "Ultrafast Non-Thermal Control of Magnetization by Instantaneous Photomagnetic Pulses," *Nature (London)* **435**, 655.
- Kimel, A. V., C. D. Stanciu, P. A. Usachev, R. V. Pisarev, V. N. Gridnev, A. Kirilyuk, and Th. Rasing, 2006, "Optical Excitation of Antiferromagnetic Resonance in TmFeO<sub>3</sub>," *Phys. Rev. B* **74**, 060403.
- Kirilyuk, A., A. V. Kimel, and Th. Rasing, 2010, "Ultrafast Optical Manipulation of Magnetic Order," *Rev. Mod. Phys.* **82**, 2731.
- Kittel, C., 1951, "Theory of Antiferromagnetic Resonance," *Phys. Rev.* **82**, 565.
- Kittel, C., 1976, *Introduction to Solid State Physics* (John Wiley & Sons, New York), 5th ed.
- Kobs, A., S. Hesse, W. Kreuzpaintner, G. Winkler, D. Lott, P. Weinberger, A. Schreyer, and H. P. Oepen, 2011, "Anisotropic Interface Magnetoresistance in Pt/Co/Pt Sandwiches," *Phys. Rev. Lett.* **106**, 217207.
- Kohn, A., A. Kovács, R. Fan, G. J. McIntyre, R. C. C. Ward, and J. P. Goff, 2013, "The Antiferromagnetic Structures of IrMn<sub>3</sub> and Their Influence on Exchange-Bias," *Sci. Rep.* **3**, 2412.
- Kohn, W., and D. Sherrington, 1970, "Two Kinds of Bosons and Bose Condensates," *Rev. Mod. Phys.* **42**, 1.
- König, J., M. C. Bønsager, and A. H. MacDonald, 2001, "Dissipationless Spin Transport in Thin Film Ferromagnets," *Phys. Rev. Lett.* **87**, 187202.
- Kosevich, A. M., B. A. Ivanov, and A. S. Kovalev, 1990, "Magnetic Solitons," *Phys. Rep.* **194**, 117.
- Kosub, T., M. Kopte, R. Hu, P. Appel, B. Shields, P. Maletinsky, O. G. Schmidt, and D. Makarov, 2017, "Purely Antiferromagnetic Magnetoelectric Random Access Memory," *Nat. Commun.* **8**, 13985.
- Kovalev, A. A., 2014, "Skyrmionic Spin Seebeck Effect via Dissipative Thermomagnonic Torques," *Phys. Rev. B* **89**, 241101.
- Kriegner, D., *et al.*, 2016, "Multiple-Stable Anisotropic Magnetoresistance Memory in Antiferromagnetic MnTe," *Nat. Commun.* **7**, 11623.
- Kübler, J., and C. Felser, 2014, "Non-Collinear Antiferromagnets and the Anomalous Hall Effect," *Europhys. Lett.* **108**, 67001.
- Kurebayashi, H., *et al.*, 2014, "An Antidamping Spin-orbit Torque Originating from the Berry Curvature," *Nat. Nanotechnol.* **9**, 211.
- Lake, B., D. A. Tennant, C. D. Frost, and S. E. Nagler, 2005, "Quantum Criticality and Universal Scaling of a Quantum Antiferromagnet," *Nat. Mater.* **4**, 329.
- Lambert, C.-H., *et al.*, 2014, "All-Optical Control of Ferromagnetic Thin Films and Nanostructures," *Science* **345**, 1337.
- Lau, Y.-C., D. Betto, K. Rode, J. M. D. Coey, and P. Stamenov, 2016, "Spin-Orbit Torque Switching without External Field with a Ferromagnetic Exchange-Biased Coupling Layer," *Nat. Nanotechnol.* **11**, 758.
- Leroy, M.-A., A. M. Bataille, F. Bertran, P. Le Fèvre, A. Taleb-Ibrahimi, and S. Andrieu, 2013, "Electronic Structure of the Cr(001) Surface and Cr/MgO Interface," *Phys. Rev. B* **88**, 205134.
- Leroy, M.-A., *et al.*, 2014, "Tunnel-Mediated Coupling between Antiferromagnetic Thin Films," *Phys. Rev. B* **90**, 035432.

- Leroy, M.-A., *et al.*, 2015, “Enhanced Magnetization at the Cr/MgO(001) Interface,” *Appl. Phys. Lett.* **107**, 251602.
- Lhoutellier, G., D. Ledue, R. Patte, F. Barbe, B. Dieny, and V. Baltz, 2015, “Bimodal Distribution of Blocking Temperature for Exchange-Bias Ferromagnetic/antiferromagnetic Bilayers: A Granular Monte Carlo Study with Less Stable Magnetic Regions Spread over the Interface,” *J. Phys. D* **48**, 115001.
- Li, H., *et al.*, 2015, “Intraband and Interband Spin-Orbit Torques in Noncentrosymmetric Ferromagnets,” *Phys. Rev. B* **91**, 134402.
- Lin, W., K. Chen, S. Zhang, and C. L. Chien, 2016, “Enhancement of Thermally Injected Spin Current through an Antiferromagnetic Insulator,” *Phys. Rev. Lett.* **116**, 186601.
- Lin, W., and C. L. Chien, 2017, “Electrical Detection of Spin Backflow from an Antiferromagnetic Insulator/Y3Fe5O12 Interface,” *Phys. Rev. Lett.* **118**, 067202.
- Linder, J., 2011, “Controllable Spin-Transfer Torque on an Antiferromagnet in a Dual Spin-Valve,” *Phys. Rev. B* **84**, 094404.
- Liu, L., T. Moriyama, D. C. Ralph, and R. A. Buhrman, 2011, “Spin-Torque Ferromagnetic Resonance Induced by the Spin Hall Effect,” *Phys. Rev. Lett.* **106**, 036601.
- Liu, L., C.-F. Pai, Y. Li, H. W. Tseng, D. C. Ralph, and R. A. Buhrman, 2012, “Spin-Torque Switching with the Giant Spin Hall Effect of Tantalum,” *Science* **336**, 555.
- Lombard, L., *et al.*, 2010, “IrMn and FeMn Blocking Temperature Dependence on Heating Pulse Width,” *J. Appl. Phys.* **107**, 09D728.
- Loth, S., S. Baumann, C. P. Lutz, D. M. Eigler, and A. J. Heinrich, 2012, “Bistability in Atomic-Scale Antiferromagnets,” *Science* **335**, 196.
- Máca, F., J. Mašek, O. Stelmakhovych, X. Martí, H. Reichlová, K. Uhlířová, P. Beran, P. Wadley, V. Novák, and T. Jungwirth, 2012, “Room-Temperature Antiferromagnetism in CuMnAs,” *J. Magn. Mater.* **324**, 1606.
- MacDonald, A. H., and M. Tsoi, 2011, “Antiferromagnetic Metal Spintronics,” *Philos. Trans. R. Soc. London* **369**, 3098.
- Mahan, G. D., 2000, *Many-Particle Physics* (Kluwer Academic, New York), 3rd ed..
- Manchon, A., 2014, “Spin-orbitronics: A New Moment for Berry,” *Nat. Phys.* **10**, 340.
- Manchon, A., 2017a, “Spin Diffusion and Torques in Disordered Antiferromagnets,” *J. Phys. Condens. Matter* **29**, 104002.
- Manchon, A., 2017b, “Spin Hall Magnetoresistance in Antiferromagnet/normal Metal Bilayers,” *Phys. Status Solidi RRL*, to be published.
- Manchon, A., H. C. Koo, J. Nitta, S. M. Frolov, and R. A. Duine, 2015, “New Perspectives for Rashba Spin-orbit Coupling,” *Nat. Mater.* **14**, 871.
- Manchon, A., and S. Zhang, 2008, “Theory of Nonequilibrium Intrinsic Spin Torque in a Single Nanomagnet,” *Phys. Rev. B* **78**, 212405.
- Mangin, S., *et al.*, 2014, “Engineered Materials for All-Optical Helicity-Dependent Magnetic Switching,” *Nat. Mater.* **13**, 286.
- Martí, X., *et al.*, 2012, “Electrical Measurement of Antiferromagnetic Moments in Exchange-Coupled IrMn/NiFe Stacks,” *Phys. Rev. Lett.* **108**, 017201.
- Martí, X., *et al.*, 2014, “Room-Temperature Antiferromagnetic Memory Resistor,” *Nat. Mater.* **13**, 367.
- Martin, L. W., S. P. Crane, Y.-H. Chu, M. B. Holcomb, M. Gajek, M. Huijben, C.-H. Yang, N. Balke, and R. Ramesh, 2008, “Multiferroics and Magnetoelectrics: Thin Films and Nanostructures,” *J. Phys. Condens. Matter* **20**, 434220.
- Matos-Abiague, A., and J. Fabian, 2009, “Anisotropic Tunneling Magnetoresistance and Tunneling Anisotropic Magnetoresistance: Spin-Orbit Coupling in Magnetic Tunnel Junctions,” *Phys. Rev. B* **79**, 155303.
- Mauri, D., H. C. Siegmann, P. S. Bagus, and E. Kay, 1987, “Simple Model for Thin Ferromagnetic Films Exchange Coupled to an Antiferromagnetic Substrate,” *J. Appl. Phys.* **62**, 3047.
- Mcguire, T. R., and R. I. Potter, 1975, “Anisotropic Magnetoresistance in Ferromagnetic 3D Alloys,” *IEEE Trans. Magn.* **11**, 1018.
- Meiklejohn, W. H., 1962, “Exchange Anisotropy—a Review,” *J. Appl. Phys.* **33**, 1328.
- Meiklejohn, W. H., and C. P. Bean, 1956, “New Magnetic Anisotropy,” *Phys. Rev.* **102**, 1413–1414.
- Meinert, M., D. Graulich, and T. Matalla-Wagner, 2017, “Key Role of Thermal Activation in the Electrical Switching of Antiferromagnetic Mn<sub>2</sub> Au,” *arXiv:1706.06983*.
- Mendes, J. B. S., R. O. Cunha, O. Alves Santos, P. R. T. Ribeiro, F. L. A. Machado, R. L. Rodríguez-Suárez, A. Azevedo, and S. M. Rezende, 2014, “Large Inverse Spin Hall Effect in the Antiferromagnetic Metal Ir<sub>20</sub> Mn<sub>80</sub>,” *Phys. Rev. B* **89**, 140406.
- Merchant, P., B. Normand, K. W. Krämer, M. Boehm, D. F. McMorrow, and Ch. Rüegg, 2014, “Quantum and Classical Criticality in a Dimerized Quantum Antiferromagnet,” *Nat. Phys.* **10**, 373.
- Merodio, P., A. Ghosh, C. Lemonias, E. Gautier, U. Ebels, M. Chshiev, H. Béa, V. Baltz, and W. E. Bailey, 2014, “Penetration Depth and Absorption Mechanisms of Spin Currents in Ir<sub>20</sub>Mn<sub>80</sub> and Fe<sub>50</sub>Mn<sub>50</sub> Polycrystalline Films by Ferromagnetic Resonance and Spin Pumping,” *Appl. Phys. Lett.* **104**, 032406.
- Merodio, P., A. Kalitsov, H. Béa, V. Baltz, and M. Chshiev, 2014a, “Spin-Dependent Transport in Antiferromagnetic Tunnel Junctions,” *Appl. Phys. Lett.* **105**, 122403.
- Merodio, P., A. Kalitsov, H. Béa, V. Baltz, and M. Chshiev, 2014b, “Spin-Modulated Torque Waves in Ferrimagnetic Tunnel Junctions,” *Phys. Rev. B* **90**, 224422.
- Miao, B. F., S. Y. Huang, D. Qu, and C. L. Chien, 2013, “Inverse Spin Hall Effect in a Ferromagnetic Metal,” *Phys. Rev. Lett.* **111**, 066602.
- Miron, I. M., K. Garello, G. Gaudin, P.-J. Zermatten, M. V. Costache, S. Auffret, S. Bandiera, B. Rodmacq, A. Schuhl, and Pietro Gambardella, 2011, “Perpendicular Switching of a Single Ferromagnetic Layer Induced by in-Plane Current Injection,” *Nature (London)* **476**, 189.
- Miron, I. M., G. Gaudin, S. Auffret, B. Rodmacq, A. Schuhl, S. Pizzini, J. Vogel, and P. Gambardella, 2010, “Current-Driven Spin Torque Induced by the Rashba Effect in a Ferromagnetic Metal Layer,” *Nat. Mater.* **9**, 230.
- Molina-Ruiz, M., A. F. Lopeandía, F. Pi, D. Givord, O. Bourgeois, and J. Rodríguez-Viejo, 2011, “Evidence of Finite-Size Effect on the Néel Temperature in Ultrathin Layers of CoO Nanograins,” *Phys. Rev. B* **83**, 140407.
- Mong, R. S. K., A. M. Essin, and J. E. Moore, 2010, “Antiferromagnetic Topological Insulators,” *Phys. Rev. B* **81**, 245209.
- Moriya, T., 1960, “Anisotropic Superexchange and Weak Ferromagnetism,” *Phys. Rev.* **120**, 91.
- Moriyama, T., N. Matsuzaki, K. J. Kim, I. Suzuki, T. Taniyama, and T. Ono, 2015, “Sequential Write-Read Operations in FeRh Antiferromagnetic Memory,” *Appl. Phys. Lett.* **107**, 122403.
- Moriyama, T., S. Takei, M. Nagata, Y. Yoshimura, N. Matsuzaki, T. Terashima, Y. Tserkovnyak, and T. Ono, 2015, “Anti-Damping Spin Transfer Torque through Epitaxial Nickel Oxide,” *Appl. Phys. Lett.* **106**, 162406.
- Mourigal, M., M. Enderle, A. Klöpperpieper, J.-S. Caux, A. Stunault, and H. M. Rønnow, 2013, “Fractional Spinon Excitations in the Quantum Heisenberg Antiferromagnetic Chain,” *Nat. Phys.* **9**, 435.
- Mukai, Y., H. Hirori, T. Yamamoto, H. Kageyama, and K. Tanaka, 2014, “Antiferromagnetic Resonance Excitation by Terahertz

- Magnetic Field Resonantly Enhanced with Split Ring Resonator,” *Appl. Phys. Lett.* **105**, 022410.
- Murakami, S., N. Nagaosa, and S.-C. Zhang, 2003, “Dissipationless Quantum Spin Current at Room Temperature,” *Science* **301**, 1348.
- Nagamiya, T., 1951, “Theory of Antiferromagnetism and Antiferromagnetic Resonance Absorption, II,” *Prog. Theor. Phys.* **6**, 342.
- Nagaosa, N., J. Sinova, S. Onoda, A. H. MacDonald, and N. P. Ong, 2010, “Anomalous Hall Effect,” *Rev. Mod. Phys.* **82**, 1539.
- Nagaosa, N., and Y. Tokura, 2013, “Topological Properties and Dynamics of Magnetic Skyrmions,” *Nat. Nanotechnol.* **8**, 899.
- Nakatsuji, S., N. Kiyohara, and T. Higo, 2015, “Large Anomalous Hall Effect in a Non-Collinear Antiferromagnet at Room Temperature,” *Nature (London)* **527**, 212.
- Nakayama, H., *et al.*, 2013, “Spin Hall Magnetoresistance Induced by a Nonequilibrium Proximity Effect,” *Phys. Rev. Lett.* **110**, 206601.
- Nayak, A. K., *et al.*, 2016, “Large Anomalous Hall Effect Driven by a Nonvanishing Berry Curvature in the Noncollinear Antiferromagnet Mn<sub>3</sub>Ge,” *Sci. Adv.* **2**, e1501870.
- Néel, L., 1932, “Influence Des Fluctuations Du Champ Moléculaire Sur Les Propriétés Magnétiques Des Corps,” *Ann. Phys. (N.Y.)* **10**, 5.
- Néel, L., 1967, “Étude théorique du couplage ferro-antiferromagnétique dans les couches minces,” *Ann. Phys. (N.Y.)* **14**, 61.
- Néel, L., 1971, “Magnetism and Local Molecular Field,” *Science* **174**, 985.
- Neubauer, A., C. Pfleiderer, B. Binz, A. Rosch, R. Ritz, P. G. Niklowitz, and P. Böni, 2009, “Topological Hall Effect in the A Phase of MnSi,” *Phys. Rev. Lett.* **102**, 186602.
- Nguyen, M.-H., C.-F. Pai, K. X. Nguyen, D. A. Muller, D. C. Ralph, and R. A. Buhrman, 2015, “Enhancement of the Anti-Damping Spin Torque Efficacy of Platinum by Interface Modification,” *Appl. Phys. Lett.* **106**, 222402.
- Nikuni, T., M. Oshikawa, A. Oosawa, and H. Tanaka, 2000, “Bose-Einstein Condensation of Dilute Magnons in TiCuCl<sub>3</sub>,” *Phys. Rev. Lett.* **84**, 5868.
- Nishitani, J., T. Nagashima, and M. Hangyo, 2013, “Coherent Control of Terahertz Radiation from Antiferromagnetic Magnons in MnO Excited by Optical Laser Pulses,” *Appl. Phys. Lett.* **103**, 081907.
- Nogués, J., and I. K. Schuller, 1999, “Exchange Bias,” *J. Magn. Magn. Mater.* **192**, 203.
- Núñez, A. S., R. A. Duine, P. M. Haney, and A. H. MacDonald, 2006, “Theory of Spin Torques and Giant Magnetoresistance in Antiferromagnetic Metals,” *Phys. Rev. B* **73**, 214426.
- Núñez, A. S., and A. H. MacDonald, 2006, “Theory of Spin Transfer Phenomena in Magnetic Metals and Semiconductors,” *Solid State Commun.* **139**, 31.
- Oh, Y.-W., *et al.*, 2016, “Field-Free Switching of Perpendicular Magnetization through Spin-orbit Torque in Antiferromagnet/ferromagnet/oxide Structures,” *Nat. Nanotechnol.* **11**, 878.
- Ohnuma, Y., H. Adachi, E. Saitoh, and S. Maekawa, 2014, “Enhanced Dc Spin Pumping into a Fluctuating Ferromagnet near TC,” *Phys. Rev. B* **89**, 174417.
- Olejnik, K., *et al.*, 2017a, “Antiferromagnetic CuMnAs Multi-Level Memory Cell with Microelectronic Compatibility,” *Nat. Commun.* **8**, 15434.
- Olejnik, K., *et al.*, 2017b, “THz electrical writing speed in an antiferromagnetic memory,” *arXiv:1711.08444v1*.
- Ou, Y., S. Shi, D. C. Ralph, and R. A. Buhrman, 2016, “Strong Spin Hall Effect in the Antiferromagnet PtMn,” *Phys. Rev. B* **93**, 220405(R).
- Palacio, F., A. Paduan-Filho, and R. L. Carlin, 1980, “Phase Diagram of Antiferromagnetic K<sub>2</sub>[FeCl<sub>5</sub>(H<sub>2</sub>O)],” *Phys. Rev. B* **21**, 296.
- Park, B. G., J. Wunderlich, D. A. Williams, S. J. Joo, K. Y. Jung, K. H. Shin, K. Olejník, A. B. Shick, and T. Jungwirth, 2008, “Tunneling Anisotropic Magnetoresistance in Multilayer-(Co/Pt)/AlOx/Pt Structures,” *Phys. Rev. Lett.* **100**, 087204.
- Park, B. G., *et al.*, 2011, “A Spin-Valve-like Magnetoresistance of an Antiferromagnet-Based Tunnel Junction,” *Nat. Mater.* **10**, 347.
- Park, W., D. Baxter, S. Steenwyk, I. Moraru, W. Pratt, and J. Bass, 2000, “Measurement of Resistance and Spin-Memory Loss (spin Relaxation) at Interfaces Using Sputtered Current Perpendicular-to-Plane Exchange-Biased Spin Valves,” *Phys. Rev. B* **62**, 1178.
- Parkin, S. S. P., 1991, “Systematic Variation of the Strength and Oscillation Period of Indirect Magnetic Exchange Coupling through the 3d, 4d, and 5d Transition Metals,” *Phys. Rev. Lett.* **67**, 3598.
- Parkin, S. S. P., M. Hayashi, and L. Thomas, 2008, “Magnetic Domain-Wall Recetrack Memory,” *Science* **320**, 190.
- Pati, S. P., M. Al-Mahdawi, S. Ye, Y. Shiokawa, T. Nozaki, and M. Sahaishi, 2016, “Finite-Size Scaling Effect on Néel Temperature of Antiferromagnetic Cr<sub>2</sub>O<sub>3</sub>(0001) Films in Exchange-Coupled Heterostructures,” *Phys. Rev. B* **94**, 224417.
- Petti, D., *et al.*, 2013, “Storing Magnetic Information in IrMn/MgO/Ta Tunnel Junctions via Field-Cooling,” *Appl. Phys. Lett.* **102**, 192404.
- Pi, U. H., K. W. Kim, J. Y. Bae, S. C. Lee, Y. J. Cho, K. S. Kim, and S. Seo, 2010, “Tilting of the Spin Orientation Induced by Rashba Effect in Ferromagnetic Metal Layer,” *Appl. Phys. Lett.* **97**, 162507.
- Popova, D., A. Bringer, and S. Blügel, 2011, “Theory of the Inverse Faraday Effect in View of Ultrafast Magnetization Experiments,” *Phys. Rev. B* **84**, 214421.
- Prakash, A., J. Brangham, F. Yang, and J. P. Heremans, 2016, “Spin Seebeck Effect through Antiferromagnetic NiO,” *Phys. Rev. B* **94**, 014427.
- Prakhya, K., A. Popescu, and P. M. Haney, 2014, “Current-Induced Torques between Ferromagnets and Compensated Antiferromagnets: Symmetry and Phase Coherence Effects,” *Phys. Rev. B* **89**, 054421.
- Qaiumzadeh, A., H. Skarsvåg, C. Holmqvist, and A. Brataas, 2017, “Spin Superfluidity in Biaxial Antiferromagnetic Insulators,” *Phys. Rev. Lett.* **118**, 137201.
- Qiu, Z., *et al.*, 2016, “Spin-Current Probe for Phase Transition in an Insulator,” *Nat. Commun.* **7**, 12670.
- Qu, D., S. Y. Huang, and C. L. Chien, 2015, “Inverse Spin Hall Effect in Cr: Independence of Antiferromagnetic Ordering,” *Phys. Rev. B* **92**, 020418.
- Raičević, I., D. Popović, C. Panagopoulos, L. Benfatto, M. B. Silva Neto, E. S. Choi, and T. Sasagawa, 2011, “Skyrmions in a Doped Antiferromagnet,” *Phys. Rev. Lett.* **106**, 227206.
- Ralph, D. C., and M. D. Stiles, 2008, “Spin Transfer Torques,” *J. Magn. Magn. Mater.* **320**, 1190.
- Reichlová, H., *et al.*, 2015, “Current Induced Torques in Structures with Ultra-Thin IrMn Antiferromagnet,” *Phys. Rev. B* **92**, 165424.
- Reichlová, H., *et al.*, 2016, “Temperature and Thickness Dependence of Tunneling Anisotropic Magnetoresistance in Exchange-Biased Py/IrMn/MgO/Ta Stacks,” *Mater. Res. Express* **3**, 076406.
- Rezende, S. M., R. L. Rodríguez-Suárez, and A. Azevedo, 2016a, “Theory of the Spin Seebeck Effect in Antiferromagnets,” *Phys. Rev. B* **93**, 014425.
- Rezende, S. M., R. L. Rodríguez-Suárez, and A. Azevedo, 2016b, “Diffusive Magnonic Spin Transport in Antiferromagnetic Insulators,” *Phys. Rev. B* **93**, 054412.
- Rojas-Sánchez, J.-C., N. Reyren, P. Laczkowski, W. Savero, J.-P. Attané, C. Deranlot, M. Jamet, J.-M. George, L. Vila, and H. Jaffrès, 2014, “Spin Pumping and Inverse Spin Hall Effect in Platinum: The Essential Role of Spin-Memory Loss at Metallic Interfaces,” *Phys. Rev. Lett.* **112**, 106602.

- Roshchin, I. V., O. Petravic, R. Morales, Z.-P. Li, X. Batlle, and I. K. Schuller, 2005, “Lateral Length Scales in Exchange Bias,” *Europhys. Lett.* **71**, 297.
- Ross, M. P., 2013, Ph.D. thesis, Tech. Univ. Munchen.
- Ross, P., M. Schreier, J. Lotze, H. Huebl, R. Gross, and S. T. B. Goennenwein, 2015, “Antiferromagnetic Resonance Detected by DC Voltages in MnF<sub>2</sub>/Pt Bilayers,” *J. Appl. Phys.* **118**, 233907.
- Roy, P. E., R. M. Otxoa, and J. Wunderlich, 2016, “Robust Picosecond Writing of a Layered Antiferromagnet by Staggered Spin-Orbit Fields,” *Phys. Rev. B* **94**, 014439.
- Sachdev, S., 1999, *Quantum Phase Transitions* (Cambridge University Press, Cambridge).
- Safeer, C. K., E. Jué, A. Lopez, L. Buda-Prejbeanu, S. Auffret, S. Pizzini, O. Boulle, I. M. Miron, and G. Gaudin, 2015, “Spin-Orbit Torque Magnetization Switching Controlled by Geometry,” *Nat. Nanotechnol.* **11**, 143.
- Saglam, H., W. Zhang, M. B. Jungfleisch, J. Sklenar, J. E. Pearson, J. B. Ketterson, and A. Hoffmann, 2016, “Spin Transport through the Metallic Antiferromagnet FeMn,” *Phys. Rev. B* **94**, 140412(R).
- Sahoo, R., *et al.*, 2016, “Compensated Ferrimagnetic Tetragonal Heusler Thin Films for Antiferromagnetic Spintronics,” *Adv. Mater.* **28**, 8499.
- Saidaoui, H. B. M., A. Manchon, and X. Waintal, 2014, “Spin Transfer Torque in Antiferromagnetic Spin Valves: From Clean to Disordered Regimes,” *Phys. Rev. B* **89**, 174430.
- Saidaoui, H. B. M., X. Waintal, and A. Manchon, 2017, “Robust spin transfer torque in antiferromagnetic tunnel junctions,” *Phys. Rev. B* **95**, 134424.
- Saidl, V., *et al.*, 2016, “Investigation of Magneto-Structural Phase Transition in FeRh by Reflectivity and Transmittance Measurements in Visible and near-Infrared Spectral Region,” *New J. Phys.* **18**, 083017.
- Saidl, V., *et al.*, 2017, “Optical Determination of the Néel Vector in a CuMnAs Thin-Film Antiferromagnet,” *Nat. Photonics* **11**, 91.
- Saitoh, E., M. Ueda, H. Miyajima, and G. Tatara, 2006, “Conversion of Spin Current into Charge Current at Room Temperature: Inverse Spin-Hall Effect,” *Appl. Phys. Lett.* **88**, 182509.
- Salazar-Alvarez, G., *et al.*, 2009, “Direct Evidence of Imprinted Vortex States in the Antiferromagnet of Exchange Biased Microdisks,” *Appl. Phys. Lett.* **95**, 012510.
- Sando, D., A. Barthélémy, and M. Bibes, 2014, “BiFeO<sub>3</sub> Epitaxial Thin Films and Devices: Past, Present and Future,” *J. Phys. Condens. Matter* **26**, 473201.
- Satoh, T., S.-J. Cho, R. Iida, T. Shimura, K. Kuroda, H. Ueda, Y. Ueda, B. A. Ivanov, F. Nori, and M. Fiebig, 2010, “Spin Oscillations in Antiferromagnetic NiO Triggered by Circularly Polarized Light,” *Phys. Rev. Lett.* **105**, 077402.
- Satoh, T., B. B. van Aken, N. P. Duong, T. Lottermoser, and M. Fiebig, 2007, “Ultrafast Spin and Lattice Dynamics in Antiferromagnetic Cr<sub>2</sub>O<sub>3</sub>,” *Phys. Rev. B* **75**, 155406.
- Scalapino, D. J., 2012, “A Common Thread: The Pairing Interaction for Unconventional Superconductors,” *Rev. Mod. Phys.* **84**, 1383.
- Schlickeiser, F., U. Ritzmann, D. Hinzke, and U. Nowak, 2014, “Role of Entropy in Domain Wall Motion in Thermal Gradients,” *Phys. Rev. Lett.* **113**, 097201.
- Scholl, A., M. Liberati, E. Arenholz, H. Ohldag, and J. Stöhr, 2004, “Creation of an Antiferromagnetic Exchange Spring,” *Phys. Rev. Lett.* **92**, 247201.
- Schütte, C., J. Iwasaki, A. Rosch, and N. Nagaosa, 2014, “Inertia, Diffusion, and Dynamics of a Driven Skyrmion,” *Phys. Rev. B* **90**, 174434.
- Seemann, K. M., *et al.*, 2010, “Spin-Orbit Strength Driven Crossover between Intrinsic and Extrinsic Mechanisms of the Anomalous Hall Effect in the Epitaxial L10-Ordered Ferromagnets FePd and FePt,” *Phys. Rev. Lett.* **104**, 076402.
- Seifert, T., *et al.*, 2016, “Efficient Metallic Spintronic Emitters of Ultrabroadband Terahertz Radiation,” *Nat. Photonics* **10**, 483.
- Seifert, T., and T. Kampfrath, 2017, “Terahertz Spectroscopy of Femtosecond Spins Currents in Magnetic Heterostructures,” oral presentation, and private communication at the DPG Meeting, Dresden.
- Seki, S., T. Ideue, M. Kubota, Y. Kozuka, R. Takagi, M. Nakamura, Y. Kaneko, M. Kawasaki, and Y. Tokura, 2015, “Thermal Generation of Spin Current in an Antiferromagnet,” *Phys. Rev. Lett.* **115**, 266601.
- Sekine, A., and T. Chiba, 2016, “Electric-Field-Induced Spin Resonance in Antiferromagnetic Insulators: Inverse Process of the Dynamical Chiral Magnetic Effect,” *Phys. Rev. B* **93**, 220403.
- Sekine, A., and K. Nomura, 2016, “Chiral Magnetic Effect and Anomalous Hall Effect in Antiferromagnetic Insulators with Spin-Orbit Coupling,” *Phys. Rev. Lett.* **116**, 096401.
- Selzer, S., U. Atxitia, U. Ritzmann, D. Hinzke, and U. Nowak, 2016, “Inertia-Free Thermally Driven Domain-Wall Motion in Antiferromagnets,” *Phys. Rev. Lett.* **117**, 107201.
- Shang, T., *et al.*, 2016, “Effect of NiO Inserted Layer on Spin-Hall Magnetoresistance in Pt/NiO/YIG Heterostructures,” *Appl. Phys. Lett.* **109**, 032410.
- Shick, A. B., S. Khmelevskiy, O. N. Mryasov, J. Wunderlich, and T. Jungwirth, 2010, “Spin-Orbit Coupling Induced Anisotropy Effects in Bimetallic Antiferromagnets: A Route towards Antiferromagnetic Spintronics,” *Phys. Rev. B* **81**, 212409.
- Shick, A. B., F. Máca, J. Mašek, and T. Jungwirth, 2006, “Prospect for Room Temperature Tunneling Anisotropic Magnetoresistance Effect: Density of States Anisotropies in CoPt Systems,” *Phys. Rev. B* **73**, 024418.
- Shiino, T., S. H. Oh, P. M. Haney, S. W. Lee, G. Go, B. G. Park, and K. J. Lee, 2016, “Antiferromagnetic Domain Wall Motion Driven by Spin-Orbit Torques,” *Phys. Rev. Lett.* **117**, 087203.
- Shindou, R., and N. Nagaosa, 2001, “Orbital Ferromagnetism and Anomalous Hall Effect in Antiferromagnets on the Distorted Fcc Lattice,” *Phys. Rev. Lett.* **87**, 116801.
- Sinova, J., S. O. Valenzuela, J. Wunderlich, C. H. Bach, and T. Jungwirth, 2015, “Spin Hall Effect,” *Rev. Mod. Phys.* **87**, 1213.
- Sinova, J., and I. Žutić, 2012, “New Moves of the Spintronics Tango,” *Nat. Mater.* **11**, 368.
- Skarsvåg, H., C. Holmqvist, and A. Brataas, 2015, “Spin Superfluidity and Long-Range Transport in Thin-Film Ferromagnets,” *Phys. Rev. Lett.* **115**, 237201.
- Sklenar, J., W. Zhang, M. B. Jungfleisch, W. Jiang, H. Saglam, J. E. Pearson, J. B. Ketterson, and A. Hoffmann, 2016, “Spin Hall Effects in Metallic Antiferromagnets—Perspectives for Future Spin-Orbitronics,” *AIP Adv.* **6**, 055603.
- Skumryev, V., S. Stoyanov, Y. Zhang, G. Hadjipanayis, D. Givord, and J. Nogues, 2003, “Beating the Superparamagnetic Limit with Exchange Bias,” *Nature (London)* **423**, 850.
- Slaughter, J. M., N. D. Rizzo, and F. B. Mancoff, 2010, “Toggle and Spin-Torque MRAM: Status and Outlook,” *J. Magn. Soc. Jpn.* **5**, 171.
- Slonczewski, J. C., 1996, “Current-Driven Excitation of Magnetic Multilayers,” *J. Magn. Magn. Mater.* **159**, L1.
- Šmejkal, L., T. Jungwirth, and J. Sinova, 2017, “Route towards Dirac and Weyl Antiferromagnetic Spintronics,” *Phys. Status Solidi RRL* **11**, 1700044.
- Šmejkal, L., J. Železný, J. Sinova, and T. Jungwirth, 2017, “Electric Control of Dirac Quasiparticles by Spin-Orbit Torque in an Antiferromagnet,” *Phys. Rev. Lett.* **118**, 106402.

- Soeya, S., T. Imagawa, K. Mitsuoka, and S. Narishige, 1994, "Distribution of Blocking Temperature in Bilayered Ni<sub>81</sub>Fe<sub>19</sub>/NiO Films," *J. Appl. Phys.* **76**, 5356.
- Soh, W. T., Y. Yeow, X. Zhong, and C. K. Ong, 2015, "Inverse Spin Hall Effect of Antiferromagnetic MnIr in Exchange Biased NiFe/MnIr Films," *J. Phys. D* **48**, 345002.
- Soh, Y.-A., and R. K. Kummamuru, 2011, "Spintronics in Antiferromagnets," *Phil. Trans. R. Soc. A* **369**, 3646.
- Sonin, E. B., 1978, "Analog of Superfluid Currents for Spins and Electron-Hole Pairs," *JETP* **47**, 1091 [<http://www.jetp.ac.ru/cgi-bin/e/index/e/47/6/p1091?a=list>].
- Sonin, E. B., 2010, "Spin Currents and Spin Superfluidity," *Adv. Phys.* **59**, 181.
- Stanciu, C. D., F. Hansteen, A. V. Kimel, A. Kirilyuk, A. Tsukamoto, A. Itoh, and Th Rasing, 2007, "All-Optical Magnetic Recording with Circularly Polarized Light," *Phys. Rev. Lett.* **99**, 047601.
- Stiles, M. D., and A. Zangwill, 2002, "Anatomy of Spin-Transfer Torque," *Phys. Rev. B* **66**, 014407.
- Stoner, E. C., and E. P. Wohlfarth, 1948, "A Mechanism of Magnetic Hysteresis in Heterogeneous Alloys," *Phil. Trans. R. Soc. A* **240**, 599.
- Sürgers, C., G. Fischer, P. Winkel, and H. V. Löhneysen, 2014, "Large Topological Hall Effect in the Non-Collinear Phase of an Antiferromagnet," *Nat. Commun.* **5**, 3400.
- Sürgers, C., W. Kittler, T. Wolf, and H. V. Löhneysen, 2016, "Anomalous Hall Effect in the Noncollinear Antiferromagnet Mn<sub>5</sub>Si<sub>3</sub>," *AIP Adv.* **6**, 055604.
- Suzuki, T., R. Chisnell, A. Devarakonda, Y.-T. Liu, W. Feng, D. Xiao, J. W. Lynn, and J. G. Checkelsky, 2016, "Large Anomalous Hall Effect in a Half-Heusler Antiferromagnet," *Nat. Phys.* **12**, 1119.
- Suzuki, T., S. Fukami, N. Ishiwata, M. Yamanouchi, S. Ikeda, N. Kasai, and H. Ohno, 2011, "Current-Induced Effective Field in Perpendicularly Magnetized Ta/CoFeB/MgO Wire," *Appl. Phys. Lett.* **98**, 142505.
- Svanidze, E., *et al.*, 2015, "An Itinerant Antiferromagnetic Metal without Magnetic Constituents," *Nat. Commun.* **6**, 7701.
- Swaving, A. C., and R. A. Duine, 2011, "Current-Induced Torques in Continuous Antiferromagnetic Textures," *Phys. Rev. B* **83**, 054428.
- Takahashi, M., 1977, "Half-Filled Hubbard Model at Low Temperature," *J. Phys. C* **10**, 1289.
- Takano, K., R. H. Kodama, A. E. Berkowitz, W. Cao, and G. Thomas, 1997, "Interfacial Uncompensated Antiferromagnetic Spins: Role in Unidirectional Anisotropy in Polycrystalline Ni<sub>81</sub>Fe<sub>19</sub>/CoO Bilayers," *Phys. Rev. Lett.* **79**, 1130.
- Takei, S., B. I. Halperin, A. Yacoby, and Y. Tserkovnyak, 2014, "Superfluid Spin Transport through Antiferromagnetic Insulators," *Phys. Rev. B* **90**, 094408.
- Takei, S., T. Moriyama, T. Ono, and Y. Tserkovnyak, 2015, "Antiferromagnet-Mediated Spin Transfer between a Metal and a Ferromagnet," *Phys. Rev. B* **92**, 020409.
- Takei, S., and Y. Tserkovnyak, 2014, "Superfluid Spin Transport through Easy-Plane Ferromagnetic Insulators," *Phys. Rev. Lett.* **112**, 227201.
- Takei, S., and Y. Tserkovnyak, 2015, "Nonlocal Magnetoresistance Mediated by Spin Superfluidity," *Phys. Rev. Lett.* **115**, 156604.
- Tanaka, T., H. Kontani, M. Naito, T. Naito, D. S. Hirashima, K. Yamada, and J. Inoue, 2008, "Intrinsic Spin Hall Effect and Orbital Hall Effect in 4d and 5d Transition Metals," *Phys. Rev. B* **77**, 165117.
- Tang, P., Q. Zhou, G. Xu, and S.-C. Zhang, 2016, "Dirac Fermions in Antiferromagnetic Semimetal," *Nat. Phys.* **12**, 1100.
- Tang, X.-L., H. W. Zhang, H. Su, Y. L. Jing, and Z. Y. Zhong, 2010, "Spin-Transfer Effect and Independence of Coercivity and Exchange Bias in a Layered Ferromagnet/antiferromagnet System," *Phys. Rev. B* **81**, 052401.
- Tang, X.-L., H.-W. Zhang, H. Su, Z. Y. Zhong, and Y.-L. Jing, 2007, "Changing and Reversing the Exchange Bias in a Current-in-Plane Spin Valve by Means of an Electric Current," *Appl. Phys. Lett.* **91**, 122504.
- Tang, Y., D. Smith, B. Zink, F. Hellman, and A. Berkowitz, 2003, "Finite Size Effects on the Moment and Ordering Temperature in Antiferromagnetic CoO Layers," *Phys. Rev. B* **67**, 054408.
- Thomson, W., 1856, "On the Electro-Dynamic Qualities of Metals: Effects of Magnetization on the Electric Conductivity of Nickel and Iron," *Proc. R. Soc. London* **8**, 546.
- Tokaç, M., S. A. Bunyayev, G. N. Kakazei, D. S. Schmool, D. Atkinson, and A. T. Hindmarch, 2015, "Interfacial Structure Dependent Spin Mixing Conductance in Cobalt Thin Films," *Phys. Rev. Lett.* **115**, 056601.
- Tretiakov, O. A., D. Clarke, G. W. Chern, Ya. B. Bazaliy, and O. Tchernyshyov, 2008, "Dynamics of Domain Walls in Magnetic Nanostrips," *Phys. Rev. Lett.* **100**, 127204.
- Tserkovnyak, Y., S. A. Bender, R. A. Duine, and B. Flebus, 2016, "Bose-Einstein Condensation of Magnons Pumped by the Bulk Spin Seebeck Effect," *Phys. Rev. B* **93**, 100402.
- Tserkovnyak, Y., A. Brataas, and G. E. W. Bauer, 2002, "Enhanced Gilbert Damping in Thin Ferromagnetic Films," *Phys. Rev. Lett.* **88**, 117601.
- Tserkovnyak, Y., A. Brataas, G. E. W. Bauer, and B. I. Halperin, 2005, "Nonlocal Magnetization Dynamics in Ferromagnetic Heterostructures," *Rev. Mod. Phys.* **77**, 1375.
- Tshitoyan, V., C. Ciccarelli, A. P. Mihai, M. Ali, A. C. Irvine, T. A. Moore, T. Jungwirth, and A. J. Ferguson, 2015, "Electrical Manipulation of Ferromagnetic NiFe by Antiferromagnetic IrMn," *Phys. Rev. B* **92**, 214406.
- Tsymbal, E. Y., O. N. Mryasov, and P. R. LeClair, 2003, "Spin-Dependent Tunnelling in Magnetic Tunnel Junctions," *J. Phys. Condens. Matter* **15**, R109.
- Tung, L. D., K. H. J. Buschow, J. J. M. Franse, and N. P. Thuy, 1996, "Magnetic Coupling between Rare Earth Moments in Some Antiferromagnetic Gd Compounds," *J. Magn. Magn. Mater.* **154**, 96.
- Tveten, E. G., T. Müller, J. Linder, and A. Brataas, 2016, "Intrinsic Magnetization of Antiferromagnetic Textures," *Phys. Rev. B* **93**, 104408.
- Tveten, E. G., A. Qaiumzadeh, and A. Brataas, 2014, "Antiferromagnetic Domain Wall Motion Induced by Spin Waves," *Phys. Rev. Lett.* **112**, 147204.
- Tveten, E. G., A. Qaiumzadeh, O. A. Tretiakov, and A. Brataas, 2013, "Staggered Dynamics in Antiferromagnets by Collective Coordinates," *Phys. Rev. Lett.* **110**, 127208.
- Uchida, K., *et al.*, 2010a, "Spin Seebeck Insulator," *Nat. Mater.* **9**, 894.
- Uchida, K.-i., H. Adachi, T. Ota, H. Nakayama, S. Maekawa, and E. Saitoh, 2010b, "Observation of Longitudinal Spin-Seebeck Effect in Magnetic Insulators," *Appl. Phys. Lett.* **97**, 172505.
- Umetsu, R. Y., K. Fukamichi, and A. Sakuma, 2006, "Electrical and Magnetic Properties, and Electronic Structures of Pseudo-Gap-Type Antiferromagnetic L10-Type MnPt Alloys," *Mater. Trans.* **47**, 2.
- Umetsu, R. Y., C. Mitsumata, A. Sakuma, and K. Fukamichi, 2003, "Magnetic and Electrical Properties, and Mechanism of Exchange Bias-Field of Gamma-Phase and L10-Type Antiferromagnetic Mn Alloys," *Trans. Magn. Soc. Jpn.* **3**, 59.
- Urazhdin, S., and N. Anthony, 2007, "Effect of Polarized Current on the Magnetic State of an Antiferromagnet," *Phys. Rev. Lett.* **99**, 046602.
- Urs, N. O., B. Mozooni, P. Mazalski, M. Kustov, P. Hayes, S. Deldar, E. Quandt, and J. McCord, 2016, "Advanced Magneto-Optical

- Microscopy: Imaging from Picoseconds to Centimeters—Imaging Spin Waves and Temperature Distributions,” *AIP Adv.* **6**, 055605.
- Valenzuela, S. O., and M. Tinkham, 2006, “Direct Electronic Measurement of the Spin Hall Effect,” *Nature (London)* **442**, 176.
- Valet, T., and A. Fert, 1993, “Theory of the Perpendicular Magnetoresistance in Magnetic Multilayers,” *Phys. Rev. B* **48**, 7099.
- Vallejo-Fernandez, G., and J. N. Chapman, 2010, “Thermal Stability of Exchange Bias Nanostructures,” *J. Appl. Phys.* **107**, 09D704.
- Vallejo-Fernandez, G., L. E. Fernández-Outón, and K. O’Grady, 2008, “Antiferromagnetic Grain Volume Effects in Metallic Polycrystalline Exchange Bias Systems,” *J. Phys. D* **41**, 112001.
- Van der Ziel, J. P., P. S. Pershan, and I. D. Malmstrom, 1965, “Optically-Induced Magnetization Resulting from the Inverse Faraday Effect,” *Phys. Rev. Lett.* **15**, 190.
- Van Vleck, J. H., 1941, “On the Theory of Antiferromagnetism,” *J. Chem. Phys.* **9**, 85.
- Wadley, P., *et al.*, 2013, “Tetragonal Phase of Epitaxial Room-Temperature Antiferromagnet CuMnAs,” *Nat. Commun.* **4**, 2322.
- Wadley, P., *et al.*, 2015, “Antiferromagnetic Structure in Tetragonal CuMnAs Thin Films,” *Sci. Rep.* **5**, 17079.
- Wadley, P., *et al.*, 2016, “Electrical Switching of an Antiferromagnet,” *Science* **351**, 587.
- Wan, X., A. M. Turner, A. Vishwanath, and S. Y. Savrasov, 2011, “Topological Semimetal and Fermi-Arc Surface States in the Electronic Structure of Pyrochlore Iridates,” *Phys. Rev. B* **83**, 205101.
- Wang, C., H. Seinige, G. Cao, J. S. Zhou, J. B. Goodenough, and M. Tsoi, 2015, “Electrically Tunable Transport in the Antiferromagnetic Mott Insulator Sr<sub>2</sub>IrO<sub>4</sub>,” *Phys. Rev. B* **92**, 115136.
- Wang, C., H. Seinige, G. Cao, J.-S. Zhou, J. B. Goodenough, and M. Tsoi, 2014, “Anisotropic Magnetoresistance in Antiferromagnetic Sr<sub>2</sub>IrO<sub>4</sub>,” *Phys. Rev. X* **4**, 041034.
- Wang, H., C. Du, P. C. Hammel, and F. Yang, 2014, “Antiferromagnetic Spin Transport from Y<sub>3</sub>Fe<sub>5</sub>O<sub>12</sub> into NiO,” *Phys. Rev. Lett.* **113**, 097202.
- Wang, H., C. Du, P. C. Hammel, and F. Yang, 2015, “Spin Transport in Antiferromagnetic Insulators Mediated by Magnetic Correlations,” *Phys. Rev. B* **91**, 220410.
- Wang, H. L., C. H. Du, Y. Pu, R. Adur, P. C. Hammel, and F. Y. Yang, 2014, “Scaling of Spin Hall Angle in 3d, 4d, and 5d Metals from Y<sub>3</sub>Fe<sub>5</sub>O<sub>12</sub>/metal Spin Pumping,” *Phys. Rev. Lett.* **112**, 197201.
- Wang, J., B. Lian, and S. C. Zhang, 2014, “Universal Scaling of the Quantum Anomalous Hall Plateau Transition,” *Phys. Rev. B* **89**, 085106.
- Wang, K., J. G. M. Sanderink, T. Bolhuis, W. G. van der Wiel, and M. P. de Jong, 2015, “Tunnelling Anisotropic Magnetoresistance due to Antiferromagnetic CoO Tunnel Barriers,” *Sci. Rep.* **5**, 15498.
- Wang, L., S. G. Wang, Syed Rizwan, Q. H. Qin, and X. F. Han, 2009, “Magnetoresistance Effect in Antiferromagnet/nonmagnet/antiferromagnet Multilayers,” *Appl. Phys. Lett.* **95**, 152512.
- Wang, X., C. O. Paulyac, and A. Manchon, 2014, “Spin-Orbit-Coupled Transport and Spin Torque in a Ferromagnetic Heterostructure,” *Phys. Rev. B* **89**, 054405.
- Wang, Y. Y., C. Song, B. Cui, G. Y. Wang, F. Zeng, and F. Pan, 2012, “Room-Temperature Perpendicular Exchange Coupling and Tunneling Anisotropic Magnetoresistance in an Antiferromagnet-Based Tunnel Junction,” *Phys. Rev. Lett.* **109**, 137201.
- Wang, Y. Y., C. Song, G. Wang, J. Miao, F. Zeng, and F. Pan, 2014a, “Anti-Ferromagnet Controlled Tunneling Magnetoresistance,” *Adv. Funct. Mater.* **24**, 6806.
- Wang, Y. Y., C. Song, G. Y. Wang, F. Zeng, and F. Pan, 2014b, “Evidence for Asymmetric Rotation of Spins in Antiferromagnetic Exchange-Spring,” *New J. Phys.* **16**, 123032.
- Weber, N. B., H. Ohldag, H. Gomonaj, and F. U. Hillebrecht, 2003, “Magnetostrictive Domain Walls in Antiferromagnetic NiO,” *Phys. Rev. Lett.* **91**, 237205.
- Wei, Z., J. Basset, A. Sharma, J. Bass, and M. Tsoi, 2009, “Spin-Transfer Interactions in Exchange-Biased Spin Valves,” *J. Appl. Phys.* **105**, 07D108.
- Wei, Z., A. Sharma, J. Bass, and M. Tsoi, 2009, “Point-Contact Search for Antiferromagnetic Giant Magnetoresistance,” *J. Appl. Phys.* **105**, 07D113.
- Wei, Z., A. Sharma, A. Nunez, P. M. Haney, R. A. Duine, J. Bass, A. H. MacDonald, and M. Tsoi, 2007, “Changing Exchange Bias in Spin Valves with an Electric Current,” *Phys. Rev. Lett.* **98**, 116603.
- Wienholdt, S., D. Hinzke, and U. Nowak, 2012, “THz Switching of Antiferromagnets and Ferrimagnets,” *Phys. Rev. Lett.* **108**, 247207.
- Wong, C. H., and Y. Tserkovnyak, 2010, “Dissipative Dynamics of Magnetic Solitons in Metals,” *Phys. Rev. B* **81**, 060404.
- Wu, D., *et al.*, 2016, “Spin-Orbit Torques in Perpendicularly Magnetized Ir<sub>22</sub>Mn<sub>78</sub>/Co<sub>20</sub>Fe<sub>60</sub>B<sub>20</sub>/MgO Multilayer,” *Appl. Phys. Lett.* **109**, 222401.
- Wu, H. C., Z. M. Liao, R. G. S. Sofin, G. Feng, X. M. Ma, A. B. Shick, O. N. Mryasov, and I. V. Shvets, 2012, “Mn<sub>2</sub>Au: Body-Centered-Tetragonal Bimetallic Antiferromagnets Grown by Molecular Beam Epitaxy,” *Adv. Mater.* **24**, 6374.
- Wu, H.-C., *et al.*, 2016, “Anomalous Anisotropic Magnetoresistance of Antiferromagnetic Epitaxial Bimetallic Films: Mn<sub>2</sub>Au and Mn<sub>2</sub>Au/Fe Bilayers,” *Adv. Funct. Mater.* **26**, 5884.
- Wu, J., *et al.*, 2011, “Direct Observation of Imprinted Antiferromagnetic Vortex States in CoO/Fe/Ag(001) Discs,” *Nat. Phys.* **7**, 303.
- Wu, S. M., W. Zhang, A. KC, P. Borisov, J. E. Pearson, J. S. Jiang, D. Lederman, A. Hoffmann, and A. Bhattacharya, 2016, “Antiferromagnetic Spin Seebeck Effect,” *Phys. Rev. Lett.* **116**, 097204.
- Wunderlich, J., B. Kaestner, J. Sinova, and T. Jungwirth, 2005, “Experimental Observation of the Spin-Hall Effect in a Two-Dimensional Spin-Orbit Coupled Semiconductor System,” *Phys. Rev. Lett.* **94**, 047204.
- Xiao, J., and G. E. W. Bauer, 2012, “Spin-Wave Excitation in Magnetic Insulators by Spin-Transfer Torque,” *Phys. Rev. Lett.* **108**, 217204.
- Xiao, J., G. E. W. Bauer, K. C. Uchida, E. Saitoh, and S. Maekawa, 2010, “Theory of Magnon-Driven Spin Seebeck Effect,” *Phys. Rev. B* **81**, 214418.
- Xu, Y., S. Wang, and K. Xia, 2008, “Spin-Transfer Torques in Antiferromagnetic Metals from First Principles,” *Phys. Rev. Lett.* **100**, 226602.
- Yamane, Y., J. Ieda, and J. Sinova, 2016, “Electric Voltage Generation by Antiferromagnetic Dynamics,” *Phys. Rev. B* **94**, 054409.
- Yamaoka, T., M. Mekata, and H. Takaki, 1971, “Neutron Diffraction Study of Antiferro-Magnetism in Face-Centered Cubic Mn-Ir Alloys,” *J. Phys. Soc. Jpn.* **31**, 301.
- Yan, P., Y. Cao, and J. Sinova, 2015, “Thermodynamic Magnon Recoil for Domain Wall Motion,” *Phys. Rev. B* **92**, 100408.
- Yang, H., Y. Sun, Y. Zhang, W.-J. Shi, S. S. P. Parkin, and B. Yan, 2017, “Topological Weyl Semimetals in the Chiral Antiferromagnetic Materials Mn<sub>3</sub>Ge and Mn<sub>3</sub>Sn,” *New J. Phys.* **19**, 015008.
- Yang, Y., Y. Xu, X. Zhang, Y. Wang, S. Zhang, R.-W. Li, M. S. Mirshekarloo, K. Yao, and Y. Wu, 2016, “Fieldlike Spin-Orbit Torque in Ultrathin Polycrystalline FeMn Films,” *Phys. Rev. B* **93**, 094402.
- Yu, G., *et al.*, 2014, “Switching of Perpendicular Magnetization by Spin-Orbit Torques in the Absence of External Magnetic Fields,” *Nat. Nanotechnol.* **9**, 548.



- Železný, J., H. Gao, A. Manchon, F. Freimuth, Y. Mokrousov, J. Zemen, J. Mašek, J. Sinova, and T. Jungwirth, 2017, “Spin-Orbit Torques in Locally and Globally Non-Centrosymmetric Crystals: Antiferromagnets and Ferromagnets,” *Phys. Rev. B* **95**, 014403.
- Železný, J., H. Gao, K. Výborný, J. Zemen, J. Mašek, A. Manchon, J. Wunderlich, J. Sinova, and T. Jungwirth, 2014, “Relativistic Néel-Order Fields Induced by Electrical Current in Antiferromagnets,” *Phys. Rev. Lett.* **113**, 157201.
- Železný, J., Y. Zhang, C. Felser, and B. Yan, 2017, “Spin-Polarized Current in Non-Collinear Antiferromagnets Mn<sub>3</sub>X (X = Ga, Ge, Sn, Rh, Ir, Pt),” *Phys. Rev. Lett.* **119**, 187204.
- Zhang, R., and R. F. Willis, 2001, “Thickness-Dependent Curie Temperatures of Ultrathin Magnetic Films: Effect of the Range of Spin-Spin Interactions,” *Phys. Rev. Lett.* **86**, 2665.
- Zhang, S. S. L., G. Vignale, and S. Zhang, 2015, “Anisotropic Magnetoresistance Driven by Surface Spin-Orbit Scattering,” *Phys. Rev. B* **92**, 024412.
- Zhang, W., W. Han, S.-H. Yang, Y. Sun, Y. Zhang, B. Yan, and S. S. P. Parkin, 2016, “Giant Facet-Dependent Spin-Orbit Torque and Spin Hall Conductivity in the Triangular Antiferromagnet IrMn<sub>3</sub>,” *Sci. Adv.* **2**, e1600759.
- Zhang, W., M. B. Jungfleisch, F. Freimuth, W. Jiang, J. Sklenar, J. E. Pearson, J. B. Ketterson, Y. Mokrousov, and A. Hoffmann, 2015, “All-Electrical Manipulation of Magnetization Dynamics in a Ferromagnet by Antiferromagnets with Anisotropic Spin Hall Effects,” *Phys. Rev. B* **92**, 144405.
- Zhang, W., M. B. Jungfleisch, W. Jiang, J. E. Pearson, A. Hoffmann, F. Freimuth, and Y. Mokrousov, 2014, “Spin Hall Effects in Metallic Antiferromagnets,” *Phys. Rev. Lett.* **113**, 196602.
- Zhang, X., Q. Liu, J.-W. Luo, A. J. Freeman, and A. Zunger, 2014, “Hidden Spin Polarization in Inversion-Symmetric Bulk Crystals,” *Nat. Phys.* **10**, 387.
- Zhang, X., Y. Zhou, and M. Ezawa, 2016, “Antiferromagnetic Skyrmion: Stability, Creation and Manipulation,” *Sci. Rep.* **6**, 24795.
- Zhang, X., and L. K. Zou, 2014, “Planar Hall Effect in Y<sub>3</sub>Fe<sub>5</sub>O<sub>12</sub>/IrMn Films,” *Appl. Phys. Lett.* **105**, 262401.
- Zhou, R., Z. Jin, G. Li, G. Ma, Z. Cheng, and X. Wang, 2012, “Terahertz Magnetic Field Induced Coherent Spin Precession in YFeO<sub>3</sub>,” *Appl. Phys. Lett.* **100**, 061102.
- Zhou, X., L. Ma, Z. Shi, W. J. Fan, J. G. Zheng, R. F. L. Evans, and S. M. Zhou, 2015, “Magnetotransport in Metal/insulating-Ferromagnet Heterostructures: Spin Hall Magnetoresistance or Magnetic Proximity Effect,” *Phys. Rev. B* **92**, 060402(R).
- Zyuzin, V. A., and A. A. Kovalev, 2016, “Magnon Spin Nernst Effect in Antiferromagnets,” *Phys. Rev. Lett.* **117**, 217203.